University of California
Santa Barbara

Structure-property relationships of lipid-based surfactant monolayers

A dissertation submitted in partial satisfaction
of the requirements for the degree

Doctor of Philosophy
in
Chemical Engineering

by

Julia Michelle Fisher

Committee in charge:

Professor Todd M. Squires, Chair
Professor M. Scott Shell
Professor Matthew Helgeson
Professor Zvonimir Dogic

December 2023

The Dissertation of Julia Michelle Fisher is approved.

Professor M. Scott Shell

Professor Matthew Helgeson

Professor Zvonimir Dogic

Professor Todd M. Squires, Committee Chair

September 2023

Structure-property relationships of lipid-based surfactant monolayers

by

Julia Michelle Fisher

For my loved ones

Acknowledgements

Many people who know me are aware that my graduate school experience did not go as I had expected. It was, perhaps, a more tortuous path than most, taking much longer than I could have ever anticipated. Looking back, there were many people whose support carried me through this time in my life and I will do my best to sing their praises here.

First, I must thank my advisor Todd Squires. I will never forget your compassion and your faith in me. I am continuously inspired by your creativity and zest for research. Most of all, I admire how you treat others. I have always felt treated with respect. You have been patient with me when I struggled and you are generous with your time. You have created a work environment where I felt supported and could thrive.

I also wish to thank my committee members: Matt Helgeson, Scott Shell, and Zvonimir Dogic. Thank you all for being so generous with your guidance and support throughout my time here.

Many thanks to my collaborators Joe Zasadzinski, Cain Valtierrez-Gaytan, Craig Hawker, and Junfeng Chen. Some of the most fun I had doing research was when I had to opportunity to learn about and collaborate on other projects.

There are also many members of the Squires group to whom I am indebted. Ian, Hari, and Joe, thank you for letting me bombard you with research questions long after your time in the group. Alexandra, thank you for your support and advice as I navigated the grad school experience.

I have the luxury of saying that I have several friends who have supported me through this stage in my career: Rachel, Meg, Ashlee, Shona, Christy, Candice, and Chithra. I could not have made it through this experience without their kindness and love.

I certainly could not have made this journey without my family, whose unwavering support has been a cornerstone of my life. Mom, Dad, Will, and Ethan, I love you all

very much.

There are some beloved members of my family whom were here at the start of this journey, but are no longer with us. Grandma, Grandpa, and Uncle Tom, I still carry you all in my heart. I miss you dearly.

Lastly, I must thank Sean. You have been with me on this journey from almost day one, witnessing the good, the bad, and the ugly. Throughout this process, you have been my rock. I love you.

There are certainly more people who aren't listed here that deserve thanks. To the many talented and kind people I've had the privilege of meeting while working in Santa Barbara, thank you.

Curriculum Vitæ

Julia Michelle Fisher

Education

2023	Ph.D. in Chemical Engineering, University of California, Santa Barbara
2015	B.S.E in Chemical Engineering, Arizona State University

Research Experience

2016-2023	Graduate Student Researcher, University of California, Santa Barbara
2014-2015	Undergraduate Student Researcher, Arizona State University
2013-2014	Product Research & Development Intern, Henkel Consumer Goods, Inc., Scottsdale, AZ

Publications

J. M. Fisher, T. M. Squires. "Phospholipase-catalyzed degradation drives domain morphology and rheology transitions in model lung surfactant monolayers," *in preparation.*

A. V. Bayles, **J. M. Fisher**, C. S. Valentine, A. Nowbahar, M. E. Helgeson, T. M. Squires. "Hydrogen bonding strength determines water diffusivity in polymer ionogels," *Journal of Physical Chemistry B*, **125** (20), 5408-5419, 2021. DOI: 10.1021/acs.jpcb.1c01460

S. Seshadri, S. J. Bailey, L. Zhao, **J. Fisher**, M. Sroda, M. Chiu, F. Stricker, M. T. Valentine, J. Read de Alaniz, M. E. Helgeson. "Influence of polarity change and photophysical effects on photosurfactant-driven wetting," *Langmuir*, **37** (33), 9939-9951, 2021. DOI: 10.1021/acs.langmuir.1c00769

M. N. Idso, N. R. Baxter, S. Narayanan, E. Chang, **J. Fisher**, B. F. Chmelka, S. Han. "Proteorhodopsin function is primarily mediated by oligomerization in different micellar surfactant solution," *Journal of Physical Chemistry B*, **123** (19), 4180-4192, 2019. DOI: 10.1021/acs.jpcb.9b00922

J. P. Jahnke, M. N. Idso, S. Hussain, M. J. N. Junk, **J. M. Fisher**, D. D. Phan, S. Han, B. F. Chmelka. "Functionally active membrane proteins incorporated in mesostructured silica films," *Journal of the American Chemical Society*, **140** (11), 3892-3906, 2018. DOI: 10.1021/jacs.7b06863

Oral and poster presentations

J. M. Fisher, T. M. Squires. "Phospholipase-catalyzed degradation drives domain morphology and rheology transitions in lung surfactant monolayers," 97th ACS Colloid and Surface Science Symposium, June 4-7, 2023, Raleigh, NC. Oral presentation

J. M. Fisher, T. M. Squires. "Inactivation of Lung Surfactant by Phospholipase-Catalyzed Degradation," 2022 AIChE Annual Meeting, November 13-18, 2022, Phoenix, AZ. Oral presentation.

J. M. Fisher, T. M. Squires. "Understanding interfacial composition and structure of lipid-based surfactant monolayers relevant for treatment of lung disease," 15th Annual Amgen-Clorox Graduate Student Symposium, September 15, 2022, Santa Barbara, CA. Oral Presentation.

J. M. Fisher, T. M. Squires. "Inactivation of Lung Surfactant by Phospholipase-Catalyzed Degradation," ACS Fall 2022 Meeting, August 21–25, Chicago, IL. Oral presentation.

J. M. Fisher, T. M. Squires. "Inactivation of Lung Surfactant by Phospholipase-Catalyzed Degradation," 2021 AIChE Annual Meeting, November 7-11, Boston, MA. Oral presentation.

J. M. Fisher, T. M. Squires. "Inactivation of Lung Surfactant by Phospholipase-Catalyzed Degradation," 95th ACS Colloid and Surface Science Symposium, June 14-16, 2021, virtual conference. Poster presentation.

J. M. Fisher, T. M. Squires. "Inactivation of Lung Surfactant by Phospholipase-Catalyzed Degradation," Center for NanoScience Workshop: Evolving Nanosciences, September 23-27, 2019, Venice, Italy. Poster presentation.

J. M. Fisher, T. M. Squires. "Inactivation of Lung Surfactant by Phospholipase-Catalyzed Degradation," 12th Annual Amgen-Clorox Graduate Student Symposium, October 4, 2019, Santa Barbara, CA. Poster presentation.

M. N. Idso, **J. Fisher**, D. Lalli, L. Andreas, N. Baxter, M. Junk, G. Pintacuda, S. Han, B. F. Chmelka. "Structural analysis of the membrane protein proteorhodopsin incorporated in nanostructured silica-surfactant composites by solid-state NMR," 58th Experimental Nuclear Magnetic Resonance Conference, March 26-31, 2017, Pacific Grove, CA. Poster Presentation.

J. Fisher, M. N. Idso, N. P. Zussblatt, D. Lalli, L. Anders, L. Herwig, N. Baxter, F. Arnold, G. Pintacuda, S. Han, B. F. Chmelka. "Incorporation of photo-responsive membrane proteins in nanostructured silica for light-activated ion transport," 10th Annual Amgen-Clorox Graduate Student Symposium, October 6, 2017, Santa Barbara, CA. Poster presentation.

Academic Service

2022-2023	Executive Chair, Beyond Academia Conference, University of California, Santa Barbara
2019-2021	Mentor, Graduate Scholars Program, University of California, Santa Barbara

2018-2019	President, Chemical Engineering Graduate Student Association, University of California, Santa Barbara
2017-2018	Founding member and Social & Professional Development Chair, Chemical Engineering Graduate Student Association, University of California, Santa Barbara
2012-2014	Peer Mentor, Ira A. Fulton Schools of Engineering, Arizona State University

Teaching experience

Spring 2019	Teaching Assistant, CHE 120C - Transport Processes, Prof. S. Dey, Department of Chemical Engineering, University of California, Santa Barbara
Fall 2017	Teaching Assistant, CHE 152A - Process Dynamics and Control, Prof. D. Seborg, Department of Chemical Engineering, University of California, Santa Barbara
Fall 2016	Teaching Assistant, CHE 152A - Process Dynamics and Control, Prof. B. F. Chmelka, Department of Chemical Engineering, University of California, Santa Barbara
Fall 2014	Undergraduate Teaching Assistant, CHE 334 - Introduction to Transport Phenomena II: Heat and Mass Transfer, Prof. B. Mu, Department of Chemical Engineering, Arizona State University

Abstract

Structure-property relationships of lipid-based surfactant monolayers

by

Julia Michelle Fisher

Surfactants adsorb onto complex fluid-fluid interfaces, altering the interfacial energy and giving unique interfacial properties. When designing a formula containing surfactants or addressing challenges with naturally occurring surfactants, it is important to understand the interfacial properties of each surfactant system. This work investigates structure-property relationships of three surfactant systems: (1) model lung surfactant (DPPC) degraded by PLA_2; (2) lipid/fatty alcohol mixtures inspired by surfactant therapies (SRT); (3) lipid-PEG copolymers. The investigations of (1) and (2) are motivated by the need for effective ARDS therapeutics. Lung surfactant (LS) becomes 'inactivated' in ARDS and SRTs are ineffective in treating ARDS, however, the mechanisms hindering LS function and SRT efficacy are not well understood. We hypothesize that the interfacial rheology, which is not easily studied clinically, is critical to the function and efficacy of LS and SRT, respectively.

The investigation of (1) studies the evolving morphology and rheology DPPC monolayers being degraded by PLA_2. While degrading, domain morphology passes through qualitatively distinct transitions: compactification, aggregation, network percolation, coarsening, solidification, network erosion, and PLA_2-rich domain nucleation. The relative activity of the PLA_2 sample impacts the order and the duration of morphology transitions. Irrespective of PLA_2 activity, all measured linear viscoelastic surface shear moduli showed the same exponential dependence on condensed phase area fraction ($\log \mid G_s^* \mid \propto \phi$) throughout monolayer degradation. Monolayer rheology is viscous-dominant until the

domain solidification transition, at which point the relative surface elasticity begins to increase. As degradation proceeds further, the relative elasticity starts to decrease once network connections start to be severed.

The investigation of (2) studies the relationship between phase behavior, morphology, and surface rheology of DPPC, hexadecanol (HD), and dihydrocholesterol (DChol) mixtures, which are all used in SRT formulas. The morphology and rheology of DPPC:HD mixtures, with and without DChol, track with the condensation of DPPC. As DPPC condenses and domain area fraction increases, $| G_s^* |$ and relative elasticity grows. When monolayers approach fully condensed, $| G_s^* |$ continues to grow, but less strongly, and relative elasticity decreases. DChol-containing monolayers exhibit similar trends in surface rheology as DChol-free monolayers, but are comparatively easier to shear, especially as surface pressure increases.

System (3) is a library of discrete DMG-PEG4-n copolymers, motivated by lipid nanoparticles applications. Using Π-A isotherms of copolymer monolayers, we examine the dilute, semi-dilute, and desorption properties of each copolymer as a function of PEG headgroup size n. For the range of n examined, interactions between the PEG headgroups, as opposed to the aliphatic chains, contribute to much of the observed surface behavior. At dilute concentrations, DMG-PEG copolymers with larger headgroups occupy more interfacial area. At semi-dilute concentrations, where the PEG headgroups contact and interpenetrate, each DMG-PEG conjugate exhibits traits of a 2D polymer in a good solvent. At sufficiently high concentrations the energy of each monolayer reaches the respective desorption energy, which grows with the size of the PEG headgroup. Overall, the structure of PEG headgroups in lipid-PEG conjugates play a critical role in the resulting interfacial properties.

Contents

Curriculum Vitae **vii**

Abstract **x**

1 Introduction **1**
1.1 Lung surfactant and pulmonary disease 2
1.2 Lung surfactant inactivation and phospholipase-catalyzed degradation in ARDS 5
1.3 Structure-property relationships of surfactant monolayers inspired by surfactant replacement therapies 8
1.4 Interfacial properties of discrete lipid-PEG conjugates 10

2 Experimental details of monolayer preparation and surface rheology **12**
2.1 Monolayer preparation and visualization 12
2.2 Small amplitude oscillatory shear using microbutton microrheometry . . 14

3 Phospholipase-catalyzed degradation drives domain morphology and rheology transitions in model lung surfactant monolayers **18**
3.1 Introduction 18
3.2 Experimental 21
3.3 Results 22
3.4 Discussion and conclusions 37
3.5 Note on the content pertaining to this chapter 42

4 Monolayer morphology and rheology of DPPC, HD, and DChol mixtures evolve with DPPC phase behavior **43**
4.1 Introduction 43
4.2 Experimental methods 45
4.3 Phase behavior and morphology of 5:1 DPPC:HD with and without Dchol 46
4.4 Surface shear rheology of 5:1 DPPC:HD with and without DChol 52
4.5 Discussion and future directions 54

5 Interfacial properties of discrete lipid-PEG copolymer library as a function of PEG headgroup size **59**
5.1 Introduction . . . 59
5.2 Experimental methods . . . 62
5.3 Results and discussion . . . 63
5.4 Conclusions . . . 72

6 Conclusions and future directions **74**
6.1 Outlook on investigation of PLA_2-catalyzed degradation of model LS monolayers . . . 74
6.2 Outlook on investigation of DPPC:HD + DChol monolayers . . . 78
6.3 Outlook on investigation of DMG-PEG4-n monolayer library . . . 79

A Additional experimental protocols **81**
A.1 Cleaning protocols . . . 81
A.2 Stock solutions and handling procedures for DPPC sample preparation . . . 85
A.3 Preparing Wilhelmy plates . . . 86
A.4 Magnet holder design and handling . . . 87
A.5 Microbutton handling and setup . . . 90

B Supplementary materials for Chapter 3 **92**
B.1 Supplementary figures . . . 92
B.2 Surface behavior of PA and LPC . . . 97

C Supplementary materials for Chapter 4 **99**

D Supplementary materials for Chapter 5 **102**

Bibliography **104**

Chapter 1

Introduction

Complex fluid-fluid interfaces are ubiquitous in many industries, including biomedical, food, personal care, and petroleum. Surface-active species (surfactants) adsorb to fluid-fluid interfaces, altering the interfacial energy and giving the interface unique properties. Surfactants can be naturally occurring, exhibiting undesirable properties in some cases, while performing critical functions in others. For example, asphaltenes in crude oil adsorb to water droplets, stabilizing an emulsion which hinders refinement [1]. Alternatively, human lung surfactant (LS) is comprised primarily of phospholipids, proteins, and cholesterol, and is is responsible for moderating surface tension at the air-water interface inside the alveoli—LS is necessary for respiration and can become inactivated by pulmonary diseases such as acute respiratory distress syndrome [2, 3, 4]. Surfactants, natural or synthetic, can also be incorporated into product formulations, often to stabilize an interface. For example, pegylated lipids, phospholipids, and cholesterol were some of the surfactants incorporated in the lipid nanoparticle designs for COVID-19 mRNA vaccines, serving to stabilize either the particle or mRNA [5, 6].

When designing a formula containing surfactants (e.g. lipid nanoparticles) or addressing challenges with naturally occurring surfactant systems (e.g. inactivated lung

surfactant), it is important to understand the properties of each surfactant system on the interface. For example, both healthy and inactive lung surfactant form microstructures at the interface which influence their respective mechanical properties. To understand the role of mechanical properties in lung surfactant inactivation, it is imperative to measure the surface rheology of the microstructures on the interface. Chapter 3 details work done to measure the evolving morphology and surface rheology of model lung surfactant as it is degraded by phospholipase, an enzyme hypothesized to play a role in lung surfactant inactivation. The work of Chapter 4 is also motivated, in part, by lung surfactant activation, specifically the need for effective therapeutics to treat LS inactivation in ARDS. Chapter 4 details measurements of the morphology and surface rheology of surfactant mixtures inspired by surfactant replacement therapies used to treat lung surfactant deficiencies. Lastly, Chapter 5 is inspired by the surfactant systems in lipid nanoparticle designs, especially the use of pegylated lipids. The PEG moieties are located on the particle surface, preventing particle aggregation and extending the lifetime of particles in the body. The work of Chapter 5 interrogates how different PEG moieties behaves on an interface. Chapter 5 details surface pressure versus surface concentration measurements over a library of pegylated lipids which spans a range of PEG moiety sizes. The remainder of this chapter provides the background information and more detailed descriptions of each project.

1.1 Lung surfactant and pulmonary disease

The lung is a key organ in respiratory systems, where the intake of oxygen for metabolic processes and the output of carbon dioxide, a metabolic waste product, takes place. The alveoli are small sacs (75-300 μm in diameter) in grape-like bunches in the lung, serving as the barrier between air and the bloodstream. Alveoli make up a signif-

icant amount of the internal surface area of the lung, estimated to be $\backsim$ 1 m^2/kg body weight [2, 7]. As depicted in Figure 1.1a, the epithelial tissue of each alveolus is lined by a thin aqueous film called the alveolar hypophase, which is approximately 0.1-0.5 μm thick [2]. The air-hypophase interface contributes significant surface tension forces that must be overcome to breathe [2].

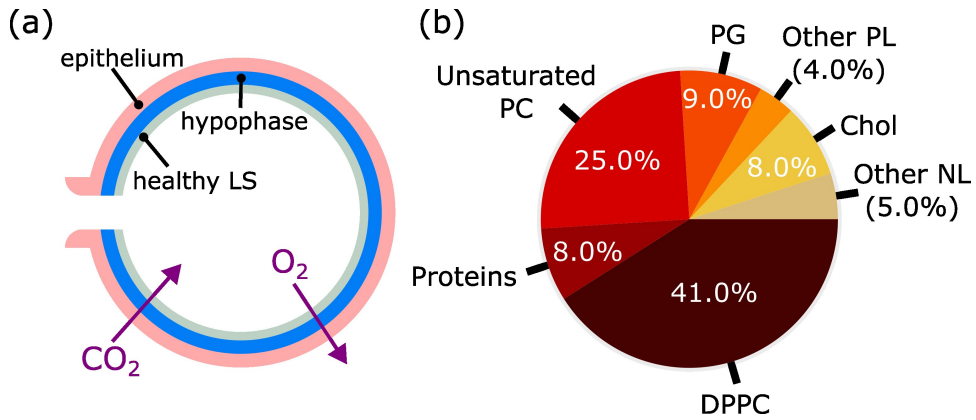

Figure 1.1: (a) Schematic diagram of gas exchange in a healthy alveolus. The epithelial tissue is lined by an aqueous hypophase and LS resides at the air-hypophase interface. The components are not drawn to scale. (b) Chart displaying the composition of human lung surfactant. LS consists of mostly phospholipids (PL), especially those with phosphocholine (PC) and phosphoglycerol (PG) headgroups [8]. The remaining fraction is comprised of proteins, cholesterol, and neutral lipids (NL) [8].

Lining the air-hypophase interface is a lung surfactant (LS) monolayer responsible for regulating surface tension in the lung. As shown by the chart in Figure 1.1b, LS is comprised almost entirely of phospholipids, with nearly half being the single phospholipid 1,2-dipalmitoyl-*sn*-glycero-3-phosphocholine (DPPC) [8]. In addition to phospholipids, LS also contains small amounts of proteins, cholesterol, and other neutral lipids [8]. LS moderates the surface tension in the lung, therefore lowering the energetic cost of breathing [2, 3]. LS is also essential for stabilizing alveoli, as evidenced by the collapse and uneven inflation observed in diseases where LS is deficient or inactivated [2, 3, 4, 9]. LS inactivation, marked by a decrease in LS surface activity, means the ability of LS to lower the surface tension to normal levels is somehow inhibited. LS inactivation and

LS deficiency are associated with pulmonary diseases such as acute respiratory distress syndrome (ARDS) and neonatal respiratory distress syndrome (NRDS) [2, 3, 4, 9].

NRDS is a pulmonary disease that can occur in premature infants, primarily affecting infants under 32 weeks of gestation [2]. Approximately 60,000 premature infants are at risk of NRDS in the US annually [2]. The underlying cause of NRDS is an insufficient amount of functional type II pneumocytes, the cells responsible for LS production [2]. As a result, NRDS patients are unable to produce enough LS for healthy respiration. In addition to alveolar collapse and uneven inflation, NRDS patients exhibit other symptoms including increased work of breathing (decreased lung compliance), reduced oxygen levels in the blood (hypoxemia), and excess fluid in the lungs (pulmonary edema) [2]. If untreated, these symptoms lead to further lung injury which most likely proves fatal. NRDS is currently treated by a combination of surfactant replacement therapy (SRT) and intensive care (e.g. mechanical ventilation). Prior to the implementation of these treatments, NRDS was the major cause of infant mortality in the US and other developed nations [2]. SRT is the delivery of exogeneous, LS-like surfactants to the lung, administered either prophylactically or once NRDS is established [2]. SRT performs the function of LS, reducing the work necessary to breathe, until the lungs are mature enough to produce sufficient LS. Since the introduction of SRT, the outcome of premature infants has greatly improved [2, 9].

ARDS, being the most severe form of acute lung injury, has a 40% mortality rate, affecting patients ranging from full-term infants to adults [2, 3, 4]. ARDS has become an especially pressing issue in recent years as the reported incidence of ARDS in non-survivors of COVID-19 is 90%.[10]. In the US, approximately 190,000 adults are diagnosed with ARDS annually [3, 4]. ARDS is identified by the rapid onset of respiratory failure, occurring approximately 12-24 hours after lung injury [2, 11, 12, 13, 14]. The causes of acute lung injury and ARDS-related respiratory failure span a breadth of pulmonary and

non-pulmonary events including chest/lung trauma, infection, toxic gas inhalation, aspiration, and shock. Like NRDS, ARDS patients exhibit decreased lung volume, decreased lung compliance, hypoxemia, and edema [2]. During the progression of ARDS, LS is said to be inactivated, however, the mechanism of inactivation is not well understood. Since ARDS and NRDS have a connection to lung surfactant and exhibit similar symptoms the medical community turned to SRT to develop therapies for ARDS. Unfortunately, clinical studies of surfactant replacement therapy for ARDS patients demonstrated only modest improvement at most and even conflicting results in some cases [15, 16, 17, 18, 19]. One possible explanation for the limited success of SRT in treating ARDS is that ARDS includes a mechanism that inactivates both endogenous and exogenous surfactants, rendering the current formulations for surfactant replacement therapy ineffective. Much of this body of work is motivated by the need to understand the mechanisms behind LS inactivation in ARDS as well as SRT efficacy in NRDS and ARDS, which are discussed in more detail in the following two sections.

1.2 Lung surfactant inactivation and phospholipase-catalyzed degradation in ARDS

Some aspects of the ARDS pathophysiology suggest pathways to LS inactivation. Surfactant-related events in the pathophysiology are summarized in Figure 1.2 [2]. Following the initial lung injury is a complex cascade of events that may negatively impact LS function. First, the alveolar tissue may suffer damage and inflammation. The injured alveolar tissue has increased permeability, introducing serum proteins, cellular lipids and other surface active material into the hypophase. Serum proteins and lipids could adsorb to the interface and interact with LS, altering LS function and perhaps compromising

LS surface activity. Tissue injury and inflammation can directly affect LS metabolism by damaging or altering the function of the cells responsible for LS production (type II pneumocytes), leading to LS deficiency. The inflammatory response also prompts the release of lytic enzymes, such as phospholipase, into the hypophase. The lytic enzymes could also adsorb to the interface and chemically degrade the LS monolayer. To summarize, there are several surface-active components released into the hypophase after the initial injury, each of which could adsorb to the interface and inactivate LS through various mechanisms.

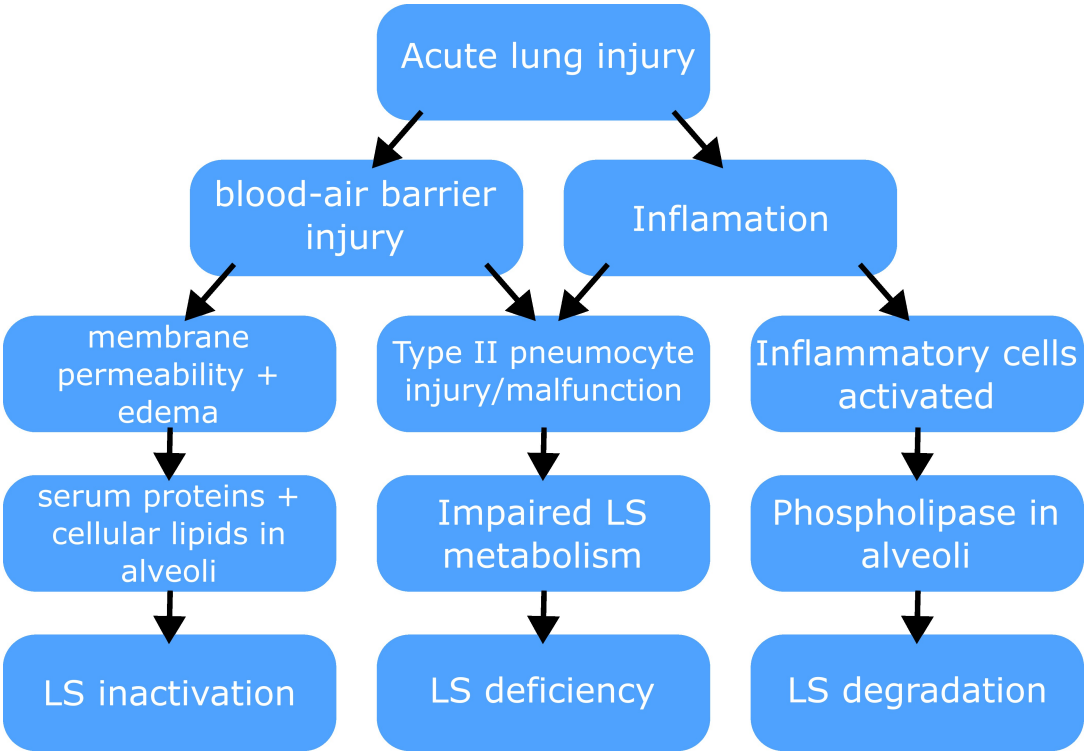

Figure 1.2: Schematic diagram of ARDS pathophysiology related to LS inactivation, deficiency, and degradation [2]. After an initial injury (e.g. pnuemonia, severe impact trauma, complications from contracting COVID-19, etc.), the alveolocapillary membrane (blood-air barrier) may suffer damage and inflammatjion. What follows is a cascade of events, which could eventually inactivate LS by comprimising surface activity or chemically degrading the LS monolayer. Not shown are events triggered by the inflammatory response unrelated to LS.

What is known about LS inactivation in ARDS clinically comes from compositional

studies of bronchoalveolar lavage, a sterile fluid flushed through a segment of the lung to extract LS for clinical diagnostics. The lavage of ARDS patients show decreased concentrations of LS phospholipids, as well as increased concentrations of serum proteins, phospholipase (PLA_2), fatty acids, and lyso-lipids [20, 21, 22]. PLA_2 is a lytic enzyme released in response to inflammation[23], which hydrolyzes phospholipids such as DPPC into fatty acids and lyso-lipids. The compositional changes in the lavage are consistent with PLA_2 being released after the initial lung injury, adsorbing to the interface, and degrading the LS monolayer. Under such conditions, LS may be less effective (i.e. inactivated) by one of two mechanisms: the deficiency in phospholipid may itself be sufficient, or, additionally, its degradation products (fatty acids and lyso-lipids) may actively interfere with LS function. An objective of the present work is to address this question. Here, we investigate the interactions between fatty acids and lyso-lipids with model LS (DPPC) by observing their effect on monolayer structure and mechanics.

There is support in the literature for the idea that palmitic acid (PA) and LPC, the fatty acid and lyso-lipid products for PLA_2-degraded DPPC, may interfere in the structure and mechanics of LS monolayers. For example, sub-micromolar concentrations of lysolipids have been shown to decrease surface tension reduction in multiple LS models.[24, 25, 26] Lysolipids exhibit line activity, altering the morphology of DPPC to less compacted shapes.[27] Likewise, PA co-crystallizes with DPPC[28], to form stiff, elastic domains, leading to nearly thousand-fold increases in surface viscosity.[29]

It is plausible that the PA produced during PLA_2-catalyzed degradation of DPPC co-crystallizes with remaining DPPC in the LS monolayer, forming stiff heterogeneities at the interface. These stiff domains would resist the deformation necessary for lung function[30], contributing to increased work of breathing and provoking further inflammation. In principle, enhanced inflammation may trigger the further release of PLA_2, contributing to a positive feedback loop that exacerbates ARDS and contributes to its

progression.

The work in Chapter 3 is motivated by the idea that PLA_2-catalyzed degradation of LS introduces components that actively interfere with the structure and morphology of LS monolayers, and therefore its function. Specifically, we track the morphology and rheology of model LS monolayers as they are degraded by PLA_2. Homogeneous, condensed phase DPPC monolayers develop an increasingly heterogeneous morphology, with increasingly heterogeneous stiffness, as PLA_2 degradation proceeds. Moreover, DPPC-PA co-crystals grow into a network, whose relative elasticity increases with time. These heterogeneous, elastic networks may impact alveolar mechanics in unexpected ways, meriting further investigation.

1.3 Structure-property relationships of surfactant monolayers inspired by surfactant replacement therapies

The outcomes in NRDS treatment have greatly improved since the implementation of SRTs. SRTs are exogeneous surfactant mixtures composed of lipids and proteins typically extracted from bovine or porcine lungs [2]. There are multiple SRTs in use today (e.g. Infasurf, Curosurf, and Survanta) and each is prepared using a different method. For example, Infasurf is processed from lavaged calf LS while Curosurf is processed from porcine lung tissue [2]. SRTs have also been manufactured synthetically, which has the advantage of more control over the composition than animal-derived methods. As a result of the different SRT preparation methods, the compositions and interfacial properties of each SRT are different. Formulas are primarily composed of phospholipids, such as DPPC, and often have small fractions of LS apoproteins, palmitic acid or hexadecanol,

and cholesterol [2]. Except for palmitic acid and hexadecanol, SRTs are composed of many of the same components as healthy LS, with the intent of emulating healthy LS function.

Clinical comparisons between SRTs for the treatment of NRDS have shown that each formula improves aspects of lung performance (e.g. gas exchange) to differing degrees. Additionally, clinically tested synthetic SRTs were found to be less efficacious than animal-derived SRTs in treating NRDS [2]. For ARDS, clinical studies of SRT demonstrated only modest improvement at most and even conflicting results in some cases [15, 16, 17, 18, 19]. However, the biophysical mechanisms behind the different SRT performances in both NRDS and ARDS are not well-understood.

We hypothesize that the morphology and corresponding rheology of SRTs, which are difficult to observe clinically, play a role in the efficacy of SRTs. An objective of the present work is to address this hypothesis by characterizing surface behavior across the SRT composition space. Chapter 4 tracks the phase behavior, morphology, and surface rheology of mixtures of DPPC, hexadecanol (HD), and dihydrocholesterol (DChol). The morphology and rheology of DPPC:HD mixtures, with and without DChol, are connected to the phase behavior of DPPC, becoming increasingly liquid-like and more difficult to shear once DPPC is condensed. The addition of DChol shifts the morphology from compact, circle-like domains to high aspect ratio stripes, as previously reported [31]. DChol-containing monolayers are comparatively easier to shear, especially as surface pressure increases. These results provide some initial insight into the relationship between SRT composition and surface mechanics. Going forward, this approach could be expanded to more mixtures of DPPC, HD and DChol as well as other SRT components, such as PA, LS apoproteins, and synthetic additives. Additionally, expanding this investigation to include DPPC-PA mixtures could provide more insight into the role of DPPC-PA co-crystals in LS inactivation.

1.4 Interfacial properties of discrete lipid-PEG conjugates

Lipid nanoparticles (LNP) are expanding as a potential delivery platform for a variety of therapeutics and are also utilized in other applications including cosmetics, food, and agriculture [5]. More recently, LNPs have become well-known as the delivery platform used for the COVID-19 mRNA vaccines [5, 6]. Notably, LNPs share many of the same components as LS and SRTs, including phospholipids, such as DPPC, and neutral lipids, like cholesterol [5]. Phospholipids in LNP formulas are desired for their biocompatibility and membrane formation [5, 6]. Cholesterol is used to modulate the fluidity of bilayers and is also highly biocompatible [5]. LNP designs often employ lipid-PEG conjugates, where a lipid has an attached, hydrophilic PEG chain headgroup. One of the most widely used lipid-PEG conjugates in LNPs is DMG-PEG2000, consisting of the lipid DMG (1,2-dimyristoyl-glycerol) coupled with a linear PEG chain of the average molecular weight 2000 g/mol [5, 6].

In LNP structures, lipid-PEG conjugates segregate to the outermost layer of the particle, with the polymer moieties forming a corona around the exterior of the particle [5, 6]. In LNPs, lipid-PEG conjugates exhibit several functions, such as dictating particle size and preventing particle aggregation [6]. The PEG moiety has low nonspecific binding and sterically blocks access to the LNP surface, extending the blood circulation lifetime of LNPs [5, 6, 32]. However, one drawback of commercial lipid-PEGs, such as DMG-PEG2000, is the polydispersity of the PEG chains [32]. Polydispersity results in batch differences, which would lead to variance in LNP properties and efficacy. More generally, polydispersity presents a challenge when trying to determine the structure-function relationships of lipid-PEG conjugates in any application. Addressing the issue of polydispersity, Chen et al. recently developed a synthesis strategy to produce discrete

libraries of lipid-PEG conjugates [32]. Using this strategy, lipid-PEG conjugates with monodisperse PEG headgroups are isolated and physical properties can be characterized as a function of headgroup structure.

Chapter 5 examines a library of DMG-PEG conjugates in the form of monolayers on an air-water interface. In this format, the PEG moieties in the monolayer are exposed to the aqueous subphase, modeling the aqueous environment around an LNP surface [33, 34, 35]. Here, we probe interfacial properties as a function of PEG headgroup size, using Π-A isotherms. When reduced to PEG surface concentration, the library of isotherms collapse onto a single curve, with some departure at higher Π. This result indicates that interactions between the PEG headgroups, as opposed to the aliphatic chains, contribute to much of the observed surface behavior. At dilute concentrations, DMG-PEG conjugates with larger headgroups occupy more interfacial area. At semi-dilute concentrations, where the PEG headgroups contact and interpenetrate, each DMG-PEG conjugate exhibits traits of a 2D polymer in a good solvent. At sufficiently high concentrations the energy of each monolayer reaches the respective desorption energy, which grows with the size of the PEG headgroup. Clearly, the structure of PEG headgroups in lipid-PEG conjugates play a critical role in the resulting interfacial properties, which would influence the structure and function of LNPs. As LNP applications continue to grow and more lipid-PEG conjugates are developed, Π-A isotherms could be a useful tool for characterizing new lipid-PEG conjugate designs.

Chapter 2

Experimental details of monolayer preparation and surface rheology

2.1 Monolayer preparation and visualization

Sample and subphase details are reported in their respective chapters. Each sample is stored in a pre-cleaned glass vial with a teflon-lined cap. The cleaning procedures for storage vials are described in Appendix A. Samples are prepared and deposited using cleaned gas-tight syringes (Hamilton) dedicated to specific steps in the sample handling process. The cleaning and handling procedures for syringes are described in Appendix A. Monolayers are prepared by adding the sample solution dropwise to the air-subphase interface in a cleaned custom Langmuir trough (Figure 2.1).

Prior to monolayer deposition, the trough, cone, and magnet holder are cleaned following a procedure adapted from Williams et al. [37]. The standard cleaning procedure is described in Appendix A. A slightly different procedure was adapted for the work in Chapter 4 to maintain consistent experimental protocols with collaborators. The alternate cleaning procedure is also described in Appendix A. For the work detailed in

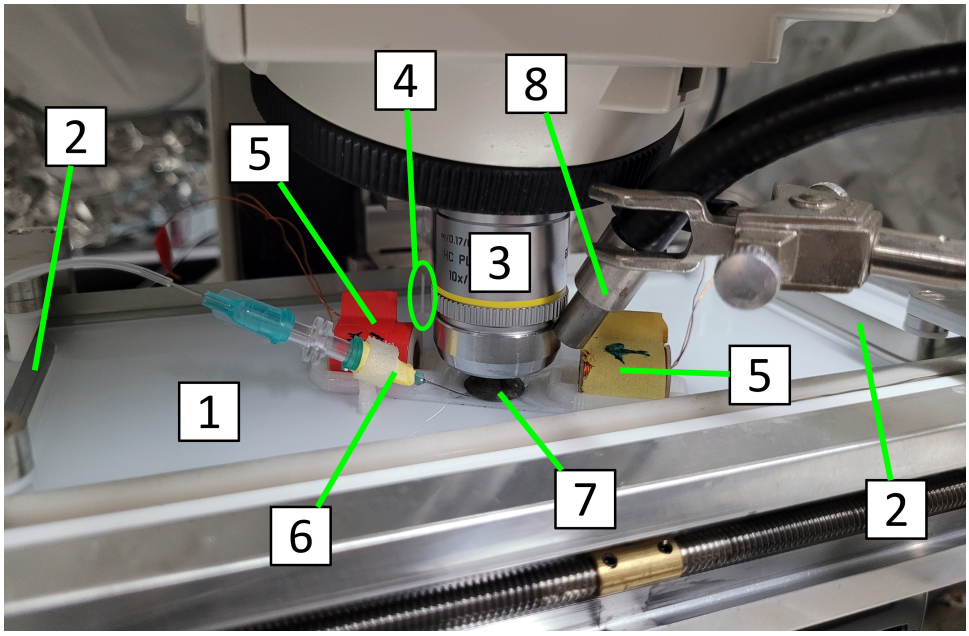

Figure 2.1: Experimental setup for studying surfactant monolayers. (1) Teflon Langmuir trough. (2) Motor-driven movable ribbon barrier. (3) Objective for brightfield/fluorescence microscope. (4) Wilhelmy plate. (5) Electromagnetic coils in custom 3D printed Nylon holder. (6) PLA_2 injection mechanism, which is described further in Chapter 3. Injection needle is connected to a syringe pump (not shown) which controls the injection of PLA_2 solution. (7) Stainless steel cone insert to suppress convective drift [36]. Two thin slits along the top edge allow surfactants to pass in and out of the cone. (8) Brightfield illumination source.

Chapter 5, no cone or magnet holders were used. Once cleaned, the trough is filled with the appropriate subphase. After deposition, the monolayer is undisturbed for either 30 minutes (Ch. 3 and 5) or 60 minutes (Ch. 4), allowing chloroform to evaporate and the monolayer to equilibrate. Monolayer morphology is visualized using a laser scanning confocal microscope (Leica DM2500). Surface pressure is measured using a filter paper Wilhelmy plate tensiometer (Riegler and Kirstein, Germany). The procedure for preparing a filter paper plate is described in Appendix A. Monolayer compression rates are reported in respective chapters. Compression is paused periodically when taking rheology measurements of DPPC monolayers. If there are no rheology measurements (Ch. 5), the monolayer is continuously compressed.

2.2 Small amplitude oscillatory shear using microbutton microrheometry

In this investigation, we utilize the microbutton microrheometry technique, described elsewhere [38]. For each experiment, a ferromagnetic microbutton probe of 50 μm radius, like the one in Figure 2.2a, is deposited on a clean interface. The probe is positioned between two oppositely aligned electromagnets connected in series, as shown schematically in Figure 2.2c. Electromagnetic coils are held in place by a custom 3D printed holder. Magnet holder design and handling practices are described in more detail in Appendix A. Each microbutton is visualized in brightfield with a CCD camera (CV-A10CL, JAI). Brightfield illumination is achieved by directing a halogen lamp light source through a fiber optic cable (Thorlabs) to shine down on the trough, as depicted in Figure 2.1. The reflection of light off the Teflon trough provides the contrast necessary to optically track the probe.

To conduct small amplitude oscillatory shear (SAOS) measurements, a sinusoidal current is applied to the electromagnets resulting in a sinusoidal magnetic field in the center of the trough. The frequency of oscillation is fixed at 1 Hz for all experiments, chosen for its relevance to the frequency of breathing. The resulting torque on the ferromagnetic microbutton,

$$\Gamma_0 e^{i\omega t} = mB_0 e^{i\omega t}, \tag{2.1}$$

drives an angular displacement,

$$\theta(t) = \theta_0 e^{i(\omega t - \delta)}. \tag{2.2}$$

which is monitored by optically tracking the orientation of the probe "buttonholes". The

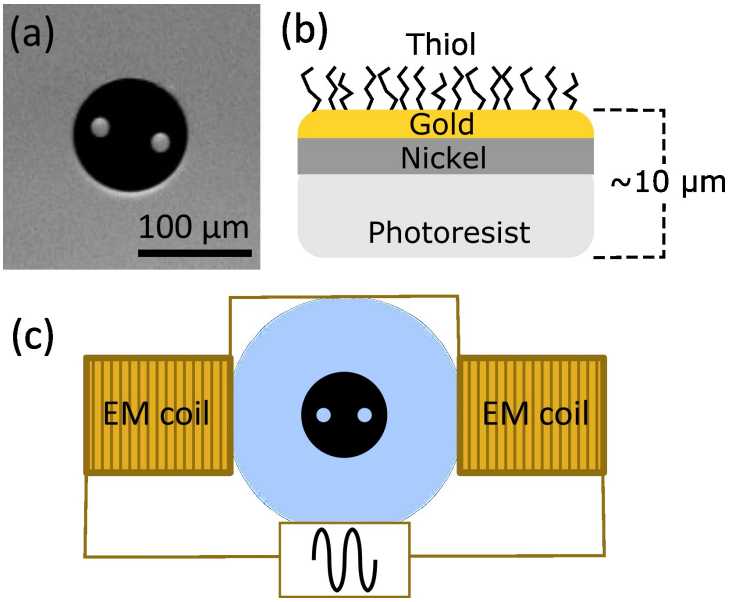

Figure 2.2: (a) Top view brightfield image of ferromagnetic microbutton probe. (b) Schematic diagram of the fabricated layers of the microbutton probe. The nickel layer provides the ferromagnetic properties of the microbutton and the thiol layer enables the amphiphilicity of the probe as described elsewhere.[39] (c) Schematic diagram of the microbutton probe placed on an air-water interface in the center of two electromagnets connected in series, used to apply an external torque on the probe.

magnetic field amplitudes were maintained such that the amplitude of angular displacement was $\lesssim 0.05$ radians. The rotational resistance ξ_R^* is calculated from the magnitudes of applied magnetic field and angular displacement,

$$\xi_R^*(\omega) = \frac{mB_0 e^{i\delta}}{i\omega\theta_0}. \tag{2.3}$$

Rotational resistance is dependent on both the subphase and interfacial drag on the probe. The Boussinesq number,

$$Bo = \frac{\eta_s}{\eta a}, \tag{2.4}$$

compares the relative magnitudes of drag contribution from the interface and the subphase, where η_s is the interfacial viscosity, η is the subphase fluid viscosity, and a is the

probe radius. For $Bo \gg 1$, interfacial drag dominates, and the rotational resistance is related to the surface viscosity by

$$\xi_R = 4\pi\eta_s a^2. \tag{2.5}$$

η_s^* is determined experimentally by combining eqn. 2.3 and 2.5 to yield,

$$\eta_s^*(\omega) = \frac{mB_0 e^{i\delta}}{i\omega\theta_0 4\pi a^2}. \tag{2.6}$$

An alternative way to express surface rheology is in terms of an interfacial shear modulus,

$$G_s^*(\omega) = i\omega\eta_s^*. \tag{2.7}$$

Therefore

$$G_s^*(\omega) = \frac{mB_0 e^{i\delta}}{\theta_0 4\pi a^2}. \tag{2.8}$$

$G_s^*(\omega)$ can be represented by its in-phase and out-of-phase components G_s' and G_s'',

$$G_s^*(\omega) = G_s'(\omega) + G_s''(\omega) = \frac{mB_0}{\theta_0 4\pi a^2}(\cos\delta + i\sin\delta). \tag{2.9}$$

G_s' and G_s'' are also referred to as the elastic and viscous shear moduli, respectively. The magnitude of the phase angle δ captures which modulus is greater, describing whether a viscoelastic material behaves more like an elastic solid or a viscous liquid. A δ greater than $\pi/4$ radians denotes a viscous-dominant response ($G_s'' > G_s'$) while δ less than $\pi/4$ radians denotes a elastic-dominant response ($G_s' > G_s''$).

Prior to spreading surfactant, the magnetic moment m of each probe is measured. At the air-buffer interface $Bo \gg 1$, meaning drag on the probe is subphase-dominated.

In the low Bo regime, rotational resistance is

$$\xi_R = \frac{16}{3}\eta a^3. \tag{2.10}$$

Combining Equations 2.3 and 2.10 and rearranging, m is expressed as

$$m = \frac{16\eta a^3 \omega \theta_0}{3B_0 \sin\delta}. \tag{2.11}$$

An oscillatory magnetic field of known amplitude and frequency is applied, and the angular displacement is tracked. The magnetic moment is accepted as the average over a minimum of 30 oscillations. Additional details on handling microbuttons and associated equipment are included in Appendix A.

Chapter 3

Phospholipase-catalyzed degradation drives domain morphology and rheology transitions in model lung surfactant monolayers

3.1 Introduction

Acute respiratory distress syndrome (ARDS) is the most severe form of acute lung injury. It is identified by the rapid onset of respiratory failure, occurring approximately 12-24 hours after lung injury with a 40% mortality rate, and affecting approximately 190,000 US adults annually [3, 4]. ARDS has become an especially pressing issue in recent years as the reported incidence of ARDS in non-survivors of COVID-19 is 90% [10]. Part of what makes ARDS so lethal is that no effective pharmacological therapeutics have been developed to treat it. One element understood to be involved in ARDS pathology is lung surfactant (LS), which is an adsorbed layer of phospholipids and proteins in the

alveoli.

In human lungs, the alveoli serve as the barrier between air and the bloodstream, making up the majority of the total internal lung surface area [2, 7]. The tissue of each alveolus is lined with a thin liquid film called the alveolar hypophase. The air-hypophase interface contributes surface tension forces that must be overcome to breathe. LS lines the air-hypophase interface and is responsible for moderating the surface tension and therefore lowering the energetic cost of breathing [2, 3]. During the progression of ARDS, LS is said to be 'inactivated', meaning that it increasingly loses its ability to reduce surface tension [2, 3]. LS is known to be essential for stabilizing alveoli; in diseases where LS is deficient or inactivated, uneven inflation of the lung — and even collapse of sections — are observed [2, 3]. Understanding how LS is inactivated represents a promising candidate to understanding ARDS, and therefore developing an effective treatment.

The mechanism for LS inactivation, however, is not well understood. What is known about LS inactivation in ARDS comes from compositional studies of bronchoalveolar lavage, a sterile fluid flushed through a segment of the lung to extract LS for clinical diagnostics. Healthy LS is more than 90% lipids by mass with most of that fraction being phospholipids [8]. Almost half of the lipid composition is just the phospholipid dipalmitoyl phosphatidylcholine (DPPC). The lavage of ARDS patients show decreased concentrations of LS phospholipids, as well as increased concentrations of serum proteins, phospholipase (PLA_2), fatty acids, and lyso-lipids [20, 21, 22]. PLA_2 is an enzyme released in response to inflammation [23], which hydrolyzes phospholipids such as DPPC into fatty acids and lyso-lipids, as shown in Figure 3.1. The compositional changes in the lavage are consistent with PLA_2 being released after the initial lung injury, adsorbing to the interface, and degrading the LS monolayer. Under such conditions, LS may be less effective (i.e. 'inactivated') by one of two mechanisms: the deficiency in phospholipid may itself be sufficient, or, additionally, its degradation products (fatty acids and lyso-

lipids) may actively interfere with LS function. The present work aims to address this question. Here, we investigate the interactions between fatty acids and lyso-lipids with model LS (DPPC) by observing their effect on monolayer structure and mechanics.

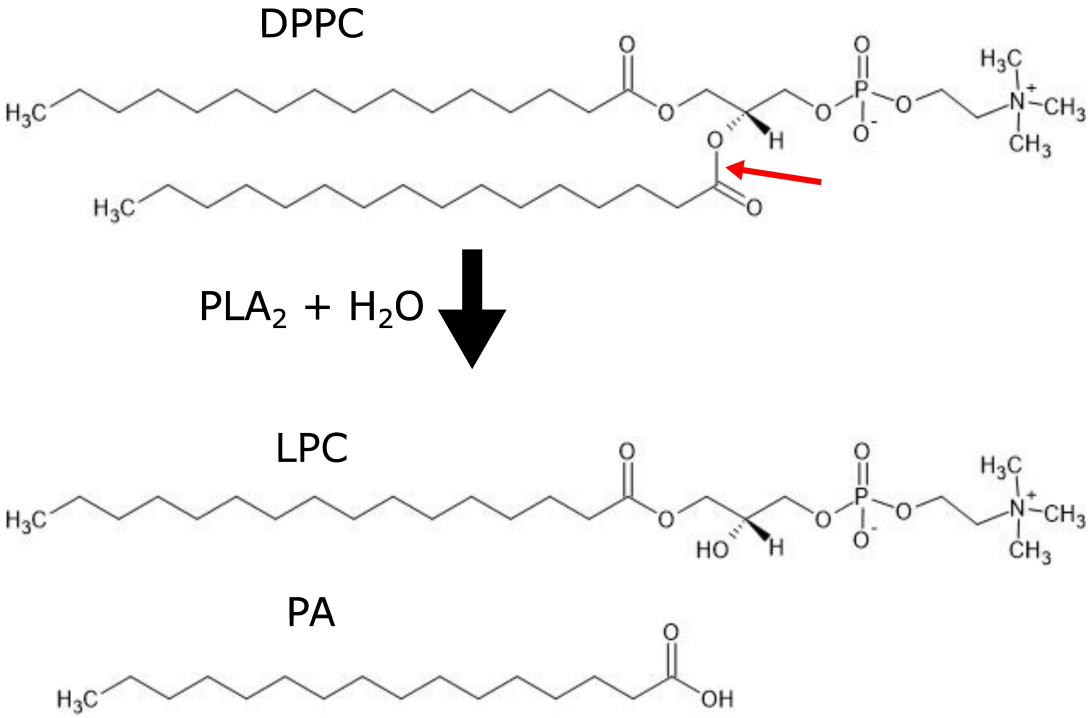

Figure 3.1: PLA_2-catalyzed degradation of DPPC produces the the corresponding lyso-lipid and fatty acid, LPC and PA, respectively. PLA_2 hydrolyzes the DPPC at the sn-2 bond, indicated by the red arrow.

There is support in the literature for the idea that palmitic acid (PA) and LPC, the fatty acid and lyso-lipid products for PLA_2-degraded DPPC, may interfere in the structure and mechanics of LS monolayers. For example, sub-micromolar concentrations of lysolipids have been shown to decrease surface tension reduction in multiple LS models [24, 25, 26]. Lysolipids exhibit line activity, altering the morphology of DPPC to less compacted shapes [27]. Likewise, PA co-crystallizes with DPPC [28], to form stiff, elastic domains, leading to nearly thousand-fold increases in surface viscosity [29].

It is plausible that the PA produced during PLA_2-catalyzed degradation of DPPC co-crystallizes with remaining DPPC in the LS monolayer, forming stiff heterogeneities at

the interface. These stiff domains would resist the deformation necessary for lung function [30], contributing to increased work of breathing and provoking further inflammation. In principle, enhanced inflammation may trigger the further release of PLA_2, contributing to a positive feedback loop that exacerbates ARDS and contributes to its progression.

The present work is motivated by the idea that PLA_2-catalyzed degradation of LS introduces components that actively interfere with the structure and morphology of LS monolayers, and therefore its function. Specifically, we track the morphology and rheology of model LS monolayers as they are degraded by PLA_2. Homogeneous, condensed phase DPPC monolayers develop an increasingly heterogeneous morphology, with increasingly heterogeneous stiffness, as PLA_2 degradation proceeds. Moreover, DPPC-PA co-crystals grow into a network, whose relative elasticity increases with time. These heterogeneous, elastic networks may impact alveolar mechanics in unexpected ways, meriting further investigation.

3.2 Experimental

3.2.1 Monolayer preparation and visualization

DPPC samples are prepared by diluting DPPC (Avanti Polar Lipids Ltd) with HPLC grade chloroform (Sigma-Aldrich). Fluorescence contrast is achieved by doping the DPPC solution with 0.5 wt% Texas Red labelled DHPE (Texas Red 1,2-dihexadecanoyl-*sn*-glycero-3-phosphoethanolamine, Life Technologies). Additional details on sample preparation and handling are included in Appendix A. The aqueous subphase is a Ca^{2+}-containing Tris-buffer: 10 mM Tris pH 8.9 (Fisher Scientific), 150 mM NaCl (Sigma-Aldrich, BioXtra grade), 5 mM $CaCl_2$ (Sigma-Aldrich, ACS grade). Ca^{2+}-ions are necessary for PLA_2 activity [40]. DPPC monolayers are prepared by spreading the DPPC

solution on the air-subphase interface in a a custom Langmuir trough (Figure 2.1).

Prior to monolayer deposition, the trough is cleaned as described in Appendix A and filled with a buffered subphase. After deposition, the monolayer is undisturbed for 30 minutes, allowing chloroform to evaporate and the monolayer to equilibrate. Morphology and surface pressure are measured as described in Chapter 2.

3.2.2 PLA_2-catalyzed degradation of model LS

PLA_2 (Sigma-Aldrich) is obtained as a lyophilized powder and dissolved in the same buffer used to make subphase (0.02 mg/mL). In an experiment, a microbutton probe and DPPC have already been deposited as previously discussed. The DPPC monolayer is then compressed to an initial surface pressure, Π_i. The compression rate is 0.02 cm^2/s, although compression is paused periodically to record morphology and surface shear rheology. PLA_2-containing solution (0.05 mL) is injected into the subphase via a syringe pump connected to the injection mechanism in Figure 3.2. As PLA_2 adsorbs to the interface, the monolayer is held at a fixed area and the morphology and rheology measurements are recorded at controlled intervals. Surface rheology measurements are conducted using the microbutton microrheometry technique as described in Chapter 2.

3.3 Results

3.3.1 Model LS morphology and rheology

The phase behavior and rheology of DPPC monolayers are well established for water and phosphate buffered saline subphases [41, 37, 42, 43]. Because PLA_2 function requires Ca^{2+}, this investigation uses Ca^{2+}-containing Tris-buffer. A standard method for studying the phase behavior is surface pressure (Π) – area isotherms, which track the surface

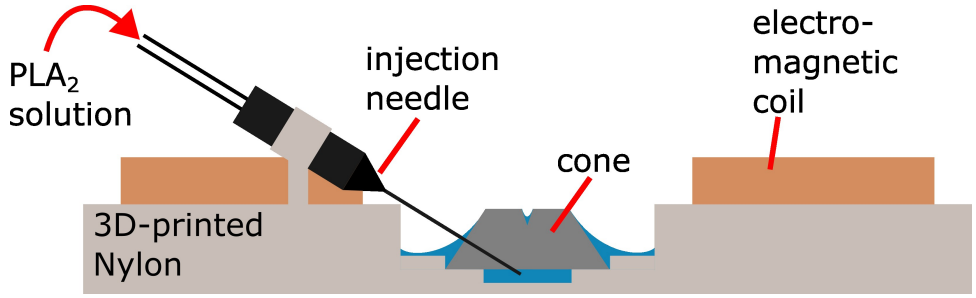

Figure 3.2: Schematic of PLA_2-injection mechanism. The entire setup is placed within the Langmuir through as shown in Figure 2.1 and cleaned as previously described in Chapter 2. Injection needle is connected to a syringe pump (not shown) which controls the injection of PLA_2 solution. Stainless steel cone insert to suppress convective drift [36]. Two thin slits along the top edge allow surfactants to pass in and out of the cone. Cone is lifted off of Langmuir trough to allow PLA_2 to enter from below the cone as well as through the slits.

pressure as a monolayer of DPPC is compressed or dilated in 2D, analogous to 3D P-V isotherms. Surface pressure is related to surface tension by

$$\Pi = \sigma^0 - \sigma, \tag{3.1}$$

where σ^0 is the surface tension of the clean interface and σ is the surface tension of the surfactant-laden interface. The surface pressure of a species on an interface is defined in thermodynamic quantities as the energy required for isothermal compression in 2D,

$$\Pi = -\frac{\delta F_S}{\delta A}\Big|_{T,N}. \tag{3.2}$$

As surface pressure rises the surface tension and the interfacial energy are lowered and less work is required to expand the interface. High surface pressures or low surface tensions, reaching nearly 0 mN/m upon exhalation, are desirable for normal lung function [2].

Figure 3.3a is a representative Π-A isotherm of DPPC on a Ca^{2+}-containing Tris-buffered subphase, capturing the phase behavior of the monolayer. For low surface concentrations (A > 80 Å^2/molecule), DPPC is in the liquid expanded (LE) phase. As the

monolayer is compressed, decreasing the area per molecule, surface pressure increases until a plateau begins. The plateau indicates phase coexistence between a liquid expanded and liquid condensed (LC) phase. The surface pressure at which the plateau initiates increases with temperature, but the onset is approximately 7 mN/m at 22 °C. While compressing along the LC-LE coexistence plateau, electrostatically repulsive, condensed domains of DPPC nucleate and grow (Figure 3.3a, inset). With further compression the monolayer transitions to a fully LC state.

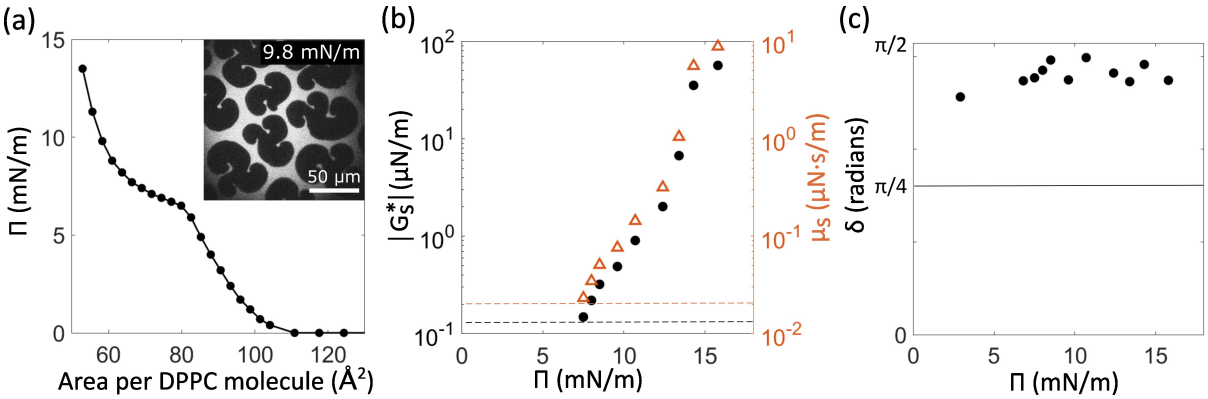

Figure 3.3: Interfacial behavior of DPPC monolayers on buffered subphase. (a) Surface pressure –area (Π –A) isotherm (T = 22 °C). Inset shows fluorescence micrograph of chiral LC domains (black) in coexistence with LE phase (bright). (b) Interfacial viscoelastic shear modulus | G_s^* | (filled circles) and surface shear viscosity μ_s (unfilled triangles) versus Π (ω = 1 Hz). Each symbol is the average of at least 10 measurements. Dashed lines denote sensitivity limit of microbutton michrorheometry in the chosen experimental configuration. (c) Phase angle δ versus Π.

The LE and LC phases are distinguished using fluorescence microscopy. In the LE phase the fluorescently tagged DHPE mixes with DPPC, appearing uniformly bright in fluorescence micrographs. LC domains exclude the fluorescently labelled DHPE and thus appear black, providing contrast with the bright expanded phase as shown in Figure 3.3a, inset. LC-DPPC domains can exhibit multi-lobed shapes, like in the Figure 3.3a inset, or a more compact bean-like shape. Each domain shape is chiral, arising from the chirality of DPPC and the tilt of its hydrophobic tails [44]. LC domains are polydisperse, with

both size and shape distribution depending on factors such as compression rate, aging, and temperature.

Figures 3.3b and 3.3c show the surface shear rheology of another DPPC monolayer under nominally the same conditions as the isotherm in Figure 3.3a. The magnitude of the linear, viscoelastic surface shear modulus $\mid G_s^* \mid$, increases approximately three orders of magnitude across the range of surface pressures in the isotherm. Below coexistence, $\Pi < 7$ mN/m, the measurement is subphase-dominated, and the recorded surface moduli cannot be distinguished from a clean interface without surfactant. At LC-LE coexistence the modulus rises exponentially with surface pressure as LC domains nucleate and grow. Figure 3.3c shows that for all surface pressures, the shear modulus at 1 Hz is viscous-dominated, meaning the interface behaves more like a viscous liquid than an elastic solid under shear deformation at the given frequency.

3.3.2 Degrading monolayer morphology follows discrete transitions

Monolayer morphology evolves significantly as PLA_2 degrades DPPC into PA and LPC. Figure 3.4 contains a series of micrographs representative of the morphology throughout the degradation process. Overall, the surface pressure and area fraction of the condensed phase decay with time. While degrading, the morphology passes through qualitatively distinct transitions: compactification, aggregation and percolation, coarsening, solidification, network erosion, and domain nucleation. Each monolayer starts with compressed, discrete LC-DPPC domains, displaying the characteristic chiral, bean-like shapes [45, 44] in Figure 3.4a. Degradation begins with PLA_2 targeting the perimeter of the LC-DPPC domains [46]. The first degradation induced change in morphology, compactification, is visible in Figure 3.4b; domains have become more isotropic and compact than

their chiral shapes in Figure 3.4a. Next, Figure 3.4c shows domains beginning to aggregate and even coalesce, or coarsen, forming the nascent network established in Figure 3.4d. With further degradation the condensed phase undergoes solidification, holding more rough, extended shapes, as shown in Figure 3.4e. Additionally in Figure 3.4e, heterogeneous pockets of trapped expanded phase have developed across the network. Lastly, as shown in Figure 3.4f, the solidified network erodes away with continued degradation, while a new condensed phase nucleates and grows. The remainder of this section is a deeper dive into how each transition occurs.

In the first transition (Figure 3.4a-3.4b), LC domains evolve away from the initial chiral shape. The group of domains circled in Figure 3.4a transition to more isotropic, compact shapes in Figure 3.4b. This transition denotes the start of PLA_2-catalyzed degradation at the phase boundaries and indicates that the domains are no longer completely LC-DPPC. Notably, some domains merge in Figure 3.4b, and by Figure 3.4c domains have aggregated and begun to coalesce. Aggregation also indicates a change in domain composition because LC-DPPC domains electrostatically repel each other [47]. As degradation continues, more domains aggregate to form increasingly larger structures, ultimately forming a percolated 2D colloidal gel-like network, like in Figure 3.4d (larger FOV image of network provided in Figure B.1).

As domains merge and aggregate into a percolated network, they also undergo a coarsening transition. Figure 3.5 follows examples of domains coarsening, including Ostwald ripening and coalescence. In Figure 3.5, the two domains outlined in the dashed line shrink and eventually disappear. We interpret the shrinkage as the result of Ostwald ripening, where DPPC molecules in small domains with higher internal surface pressure dissolve into the LE phase, then redeposit on larger domains. At the same time, the domains outlined in the solid line fuse rather than shrink, coalescing into a larger domain. Because these domains must flow and relax in order to coalesce, the condensed phase

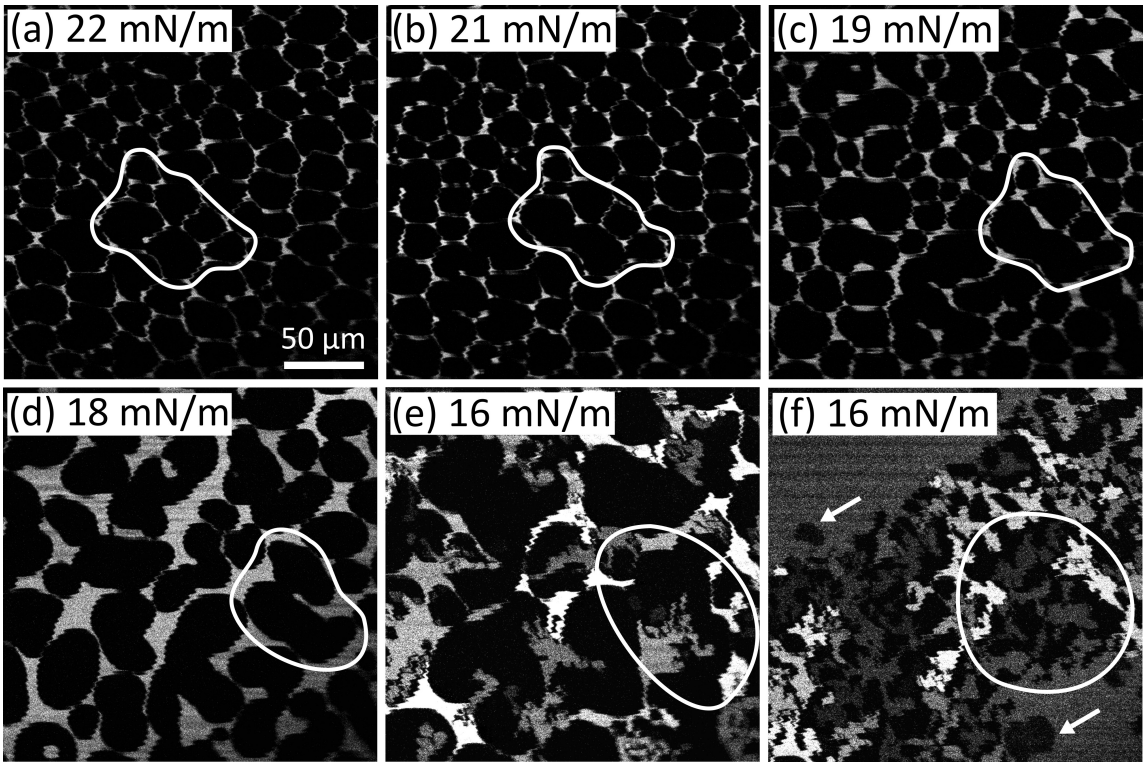

Figure 3.4: (a) LC-DPPC monolayer prior to injecting PLA_2. (b-f) Fluorescence micrograph series showing morphology transitions of the monolayer undergoing PLA_2-catalyzed degradation. White outline follows a group of domains throughout degradation. Small oscillations along the domain boundaries are the result of vibration near the microscope. (b-d) Domains undergo compactification, coarsening, and begin percolating into a network. Outlined domains coalesce, flow, and relax into larger compact domains. (e) Post-solidification: domains maintain extended phase boundaries. Network separates pockets of disordered phase, as evidenced by differing local fluorescence intensities. (f) PLA_2-catalyzed degradation erodes network. White arrows indicate new domains that nucleate and grow at later stages of degradation.

must remain liquid-like at this stage. Since the domains are liquid-like, domains growing through either coarsening mechanism will relax into compact shapes, as expected to minimize the line tension energy.

The rate of the shape transition to compact domains is consistent with line tension acting against the internal viscosity. The internal LC domain viscosity η_s^{LC} can be estimated from the time series in Figure 3.5d-3.5f, which follows the pinch-off and relaxation of two domains denoted by an arrow. The LC flow velocity v is approximately $\Delta x/\Delta t$,

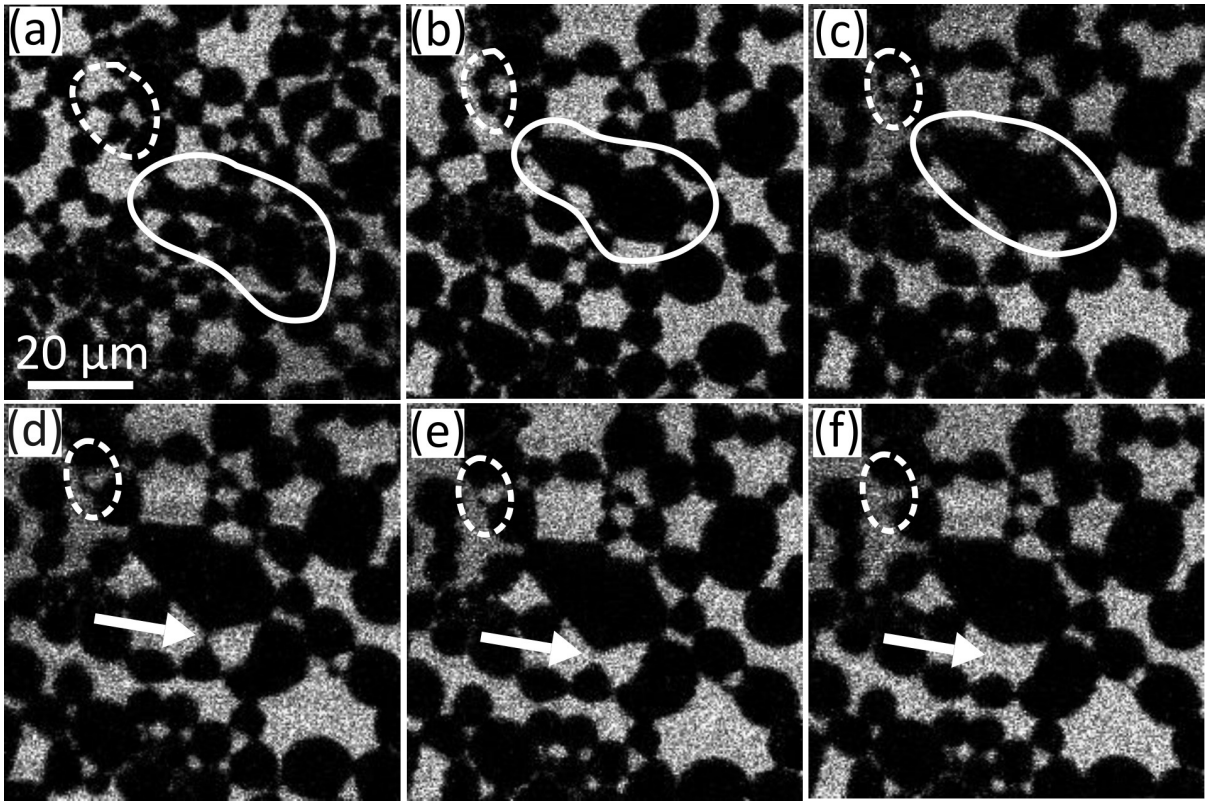

Figure 3.5: Fluorescence micrograph series of a single monolayer showing examples of coarsening processes during PLA_2-catalyzed degradation. Dashed outline follows two domains shrinking (a-d) and disappearing (e-f) via Ostwald ripening. Solid outline follows cluster of domains coalescing (a-c). Arrows follow a network connection (a) that pinches off and corresponding domains flow and relax in compact shapes (b-c).

where Δx is the change in position of the domain vertex between frames and Δt is the time between frames, and the line tension is $\backsim$ 1 pN [48, 49]. Using a 2D version of a classic argument for capillary relaxation of viscous drops ($\eta_s^{LC} \backsim \lambda/v$) [50], η_s^{LC} is estimated to be $\backsim 10^3 \mu$N·s/m. This viscosity is at least 10 times larger than pure DPPC at this surface pressure, as would be expected given the increasing palmitic acid content of the domains [29]. Since domain composition changes throughout the degradation process—with PA:DPPC ratio increasing with degradation—the domain viscosity is expected to grow. In fact, the next morphological transition is demarcated by domains no longer visibly flowing and relaxing into compact shapes.

After sufficient degradation, the liquid-like domains transition to solid-like domains. Instead of flowing and relaxing into compact shapes, what remains of the condensed network sustains much more extended phase boundaries. This is visible in Figure 3.4e, where the domains have rougher, less uniform structures than the preceding network in Figure 3.4d. Even though the same driving force to minimize line energy is present, the LC phase does not flow and relax into compact shapes. We interpret this as the internal phase of the LC network being more solid-like and unable to flow in response to stresses.

Throughout the solidification transition, a connected network of solid-like domains is clearly sustained, as demonstrated by its ability to confine the disordered phase. In Figure 3.4e, different regions of disordered phase have differing fluorescence intensities. Differing intensities indicate that unique local compositions have developed, which can only occur when different LE regions remain isolated from each other by the network, and are compressed or expanded differently in response to heterogeneous network stresses. The trapped pockets of LE phase with different compositions would also exert different surface pressures on its surrounding network. The ability of the network to sustain differences in surface pressure suggests that the network has some elasticity at this stage. As degradation continues, progressively eroding the LC phase, the solid-like network maintains the local disordered regions until network linkages are sufficiently degraded that they break apart.

Following breakage events, formerly distinct disordered environments mix, creating new local disordered regions. Examples of such events are captured in real-time in Figure B.2, which show diffusive mixing of fluorescence intensity between two distinct LE phases once their dividing LC boundary is severed. At this point in the degradation process, the pockets of disordered phase in the network keep growing as the fraction of condensed phase decays. The impact of continuous erosion of the network is visible in Figure 3.4f, where much of the condensed phase present in Figure 3.4e has been degraded. The result

is a sparse, heterogenous network with large pockets of disordered phase (larger FOV images provided in Appendix B, Fig. B.3).

While the solid-like network degrades and breaks apart, a new type of domain nucleates (Fig. 3.4f, white arrows). The new domains are the only condensed feature growing at this stage, which is demonstrated in Figure 3.6. At this resolution, it is difficult to discern how these domains nucleate from a micrograph alone, but the new domains are first seen close to the condensed phase. Maloney and Grainger also identified these domains, and indicated that they contain a mixture of DPPC and PA bound with PLA_2 in the subphase [51, 52]. Since the PLA_2-catalyzed degradation occurs at the LC-DPPC phase boundary, it is possible that these domains nucleate either near or on the phase boundary and then break off before they are large enough to see.

3.3.3 Enzymatic activity of PLA_2 influences order and duration of morphology transitions

The morphological transitions during degradation are influenced by the shelf-life of PLA_2 in the buffer solution. The short-term storage method of reconstituting a protein in buffer and refrigerating at 4 °C typically yields a shelf-life on the order of weeks. The degradation experiments discussed in this investigation span the lifetime of PLA_2 stored via this method. As a result, the decreasing stability of the stored PLA_2 over time directly affects the morphology transition processes across experiments. The remainder of this section discusses the morphology differences in more detail by comparing an experiment with relatively fresh PLA_2 ($\backsim$4 days old) to an experiment with relatively old PLA_2 ($\backsim$9 days old).

Figure 3.7 compares monolayer degradation processes with 4-day old PLA_2 versus 9-day old PLA_2 (insets), from the initial state (Fig. 3.7a) until the morphology consists

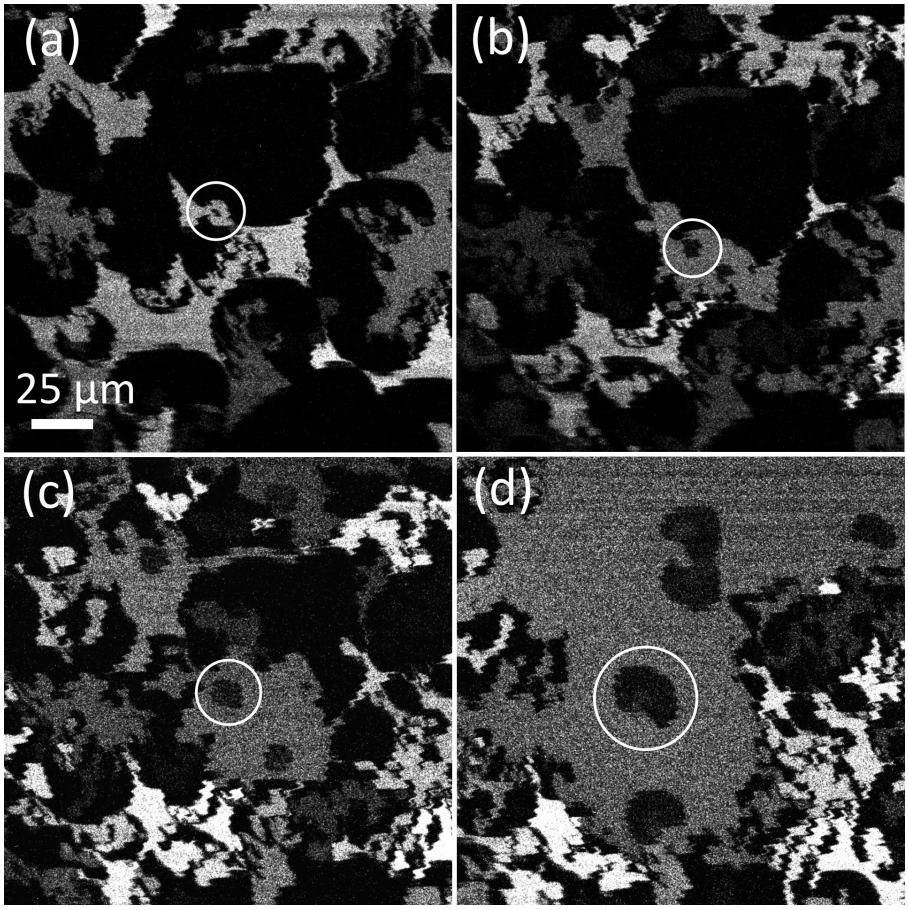

Figure 3.6: Fluorescence micrograph series of a single monolayer in the later stages of degradation, following the nucleation and growth of a condensed domain (outlined). The new domains are likely composed of DPPC and PA bound with PLA_2 in the subphase, as indicated by Maloney and Grainger [51, 52].

of aggregated domains that have solidified (Fig. 3.7c). The 9-day old PLA_2 experiment was previously shown in Figure 3.4. Each monolayer starts with packed, chiral domains of a similar size (Fig. 3.7a). The relative activity of these two PLA_2 solutions impacts the monolayer morphology transitions in qualitatively distinct ways. Notably, in Figure 3.7b, rough, solid-like domains appear only 4 minutes after injecting fresh PLA_2, before any noticeable domain coarsening or aggregation has occurred; the same domains from t=0 can be identified in Fig 3.7b. By contrast, domains degraded by old PLA_2 maintain smooth boundaries even after 90 minutes, indicating they remain liquid-like, and have

already formed an aggregated network. Moreover, domains have clearly coarsened, indicated by the smaller number of domains, the larger size of each, and the increase in LE phase. Because the time to solidification is so much shorter when using fresh PLA_2, there is insufficient time for domains to aggregate, merge, and flow into larger, compact shapes. Thus, fresher PLA_2 hastens the onset of domain solidification, thereby reducing time for domains to coarsen.

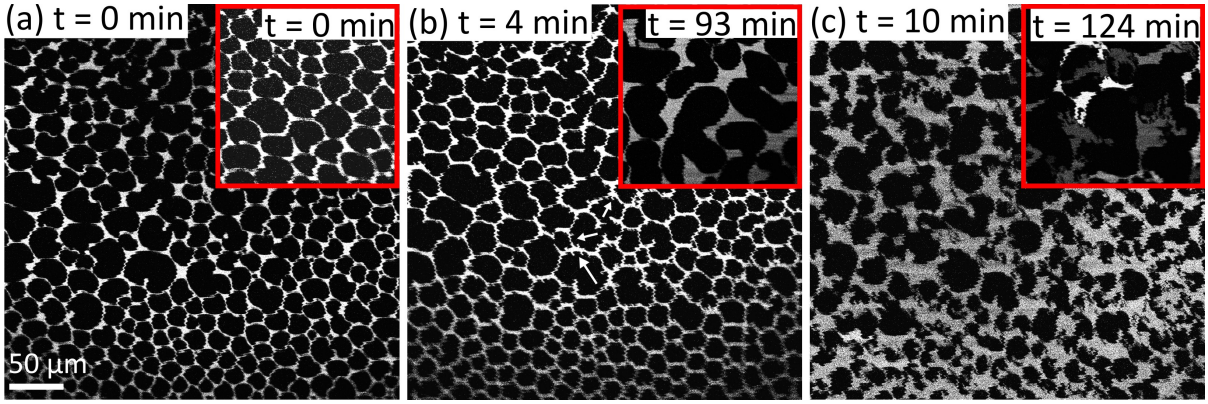

Figure 3.7: Comparison between a degrading monolayer with relatively fresh (a-c) and relatively old PLA_2 (insets). (a) Fluorescence micrographs of each LC-DPPC monolayer prior to injecting PLA_2. (b) Domain solidification already evident within 4 minutes of fresh PLA_2 injection (arrows). visible on discrete domains 4 minutes after injecting PLA_2. Inset shows network of compact, liquid-like domains that are still coarsening 1.5 hours after aged PLA_2 injection. (c) Solidified domains have aggregated into a percolated network 10 minutes after fresh PLA_2 injection. The inset shows the comparatively more heterogeneous solidified network established 2 hours after aged PLA_2 injection.

The differences stemming from restricting coarsening persist with further degradation, as shown in Figure 3.7c. In Figure 3.7c, the domains in each experiment have both solidified and aggregated into a network (larger FOV images of 3.7c and inset provided in Fig. B.4). The example using fresher PLA_2 had less time to coarsen before solidification. Therefore, the network is composed of many small domains. Alternatively, the experiment with the older PLA_2 had more time to coarsen prior to domain solidification, and thus the solid-like network is composed of fewer, larger domains. Additionally, the

pockets of LE phase trapped within each network are affected by PLA_2 age. For fresher PLA_2, solidification and aggregation occur much earlier, giving the pockets of LE phase less time to evolve before a solid-like network is achieved. As a result, the LE phase composition appears homogeneous across the network. Conversely, the use of older PLA_2 enables more time for the pockets of LE phase to evolve as the network coarsened and eventually solidified, resulting in a more heterogenous distribution of LE phase. The differences between the two networks and respective LE phases show that the relative freshness of PLA_2 not only affects the time taken to form a solid-like network, but it also sets the feature sizes of said network.

To summarize, the fresher the PLA_2, the faster the overall degradation of the condensed phase. Faster degradation results in an earlier solid-like transition and restricts the coarsening time. Less coarsening time results in a more homogenous initial solid-like network. The onset of the solid-like transition fixes the feature sizes of the network, which will determine the feature sizes going forward. After a solid-like network is formed, further structural change is dominated by the decay of the condensed phase. Once a solidified network has formed, further degradation involves the progressive degradation of this fixed structure; the condensed phase thins and linkages in the network break down.

3.3.4 Monolayer rheology tracks morphology transitions

As monolayer morphology undergoes degradation induced changes, so too does the interfacial rheology. A representative series of surface shear rheology measurements taken throughout the degradation process for a single monolayer is displayed in Figure 3.8. The magnitude of the linear viscoelastic surface shear modulus $\mid G_s^* \mid$, and LC domain area fraction ϕ for the experiment are plotted in Figure 3.8a. The phase angle, or phase lag, δ is plotted in Figure 3.8b. Corresponding micrographs depicting the evolving morphology

are included in Figure 3.8c-3.8i. Prior to adding PLA_2, the monolayer was compressed to the fully LC state in Figure 3.8c, giving rise to the initial $\mid G_s^* \mid$. The shear modulus $\mid G_s^* \mid$ does not change appreciably in the first 30 minutes after adding PLA_2, which likely reflects the time for PLA_2 to diffuse, adsorb, and appreciably degrade the monolayer.

Domain shapes transition from chiral to compact and domains aggregate to form a percolating network, all before $\mid G_s^* \mid$ starts to decay (Fig. 3.8d). The decrease in surface shear modulus $\mid G_s^* \mid$ occurs as network structures coarsen (Fig. 3.8e), and as LC domain area fraction ϕ decreases, reflecting both DPPC degradation as well as Ostwald ripening of domains. The first signs of the solidification transition appear in the bottom half of Figure 3.8f (arrows) and span the network by Figure 3.8h. Once all domains in the network have transitioned to solid-like (Fig. 3.8h), PLA_2-catalyzed degradation continues to erode the condensed phase, decreasing the thickness and connectivity of network elements. A striking correlation between $\log \mid G_s^* \mid$ and LC domain area fraction ϕ persists throughout the coarsening, solidification, and erosion processes.

The relationship between $\log \mid G_s^* \mid$ and ϕ shown in Figure 3.8a persists for PLA_2-catalyzed monolayer degradation experiments where both rheology and morphology were recorded. Figure 3.9 shows $\log \mid G_s^* \mid$ versus ϕ for all such measurements, which includes PLA_2 of different ages and variations between prepared monolayers. Each experiment differs in its range of $\mid G_s^* \mid$ and ϕ; which is initially set by the temperature and surface pressure of the DPPC monolayer. Regardless of variation in initial conditions, $\log \mid G_s^* \mid$ grows linearly with ϕ, over two decades in $\mid G_s^* \mid$.

In addition to domain area fraction, the onset of the solidification transition correlates with changes observed in monolayer rheology during PLA_2-catalyzed degradation. More specifically, the solidification onset is tied to changes in phase angle δ (Fig. 3.8b). The experiment begins with a viscous-dominant interface ($\delta \backsim \pi/2$), typical of DPPC under these conditions. The phase angle does not change appreciably during domain

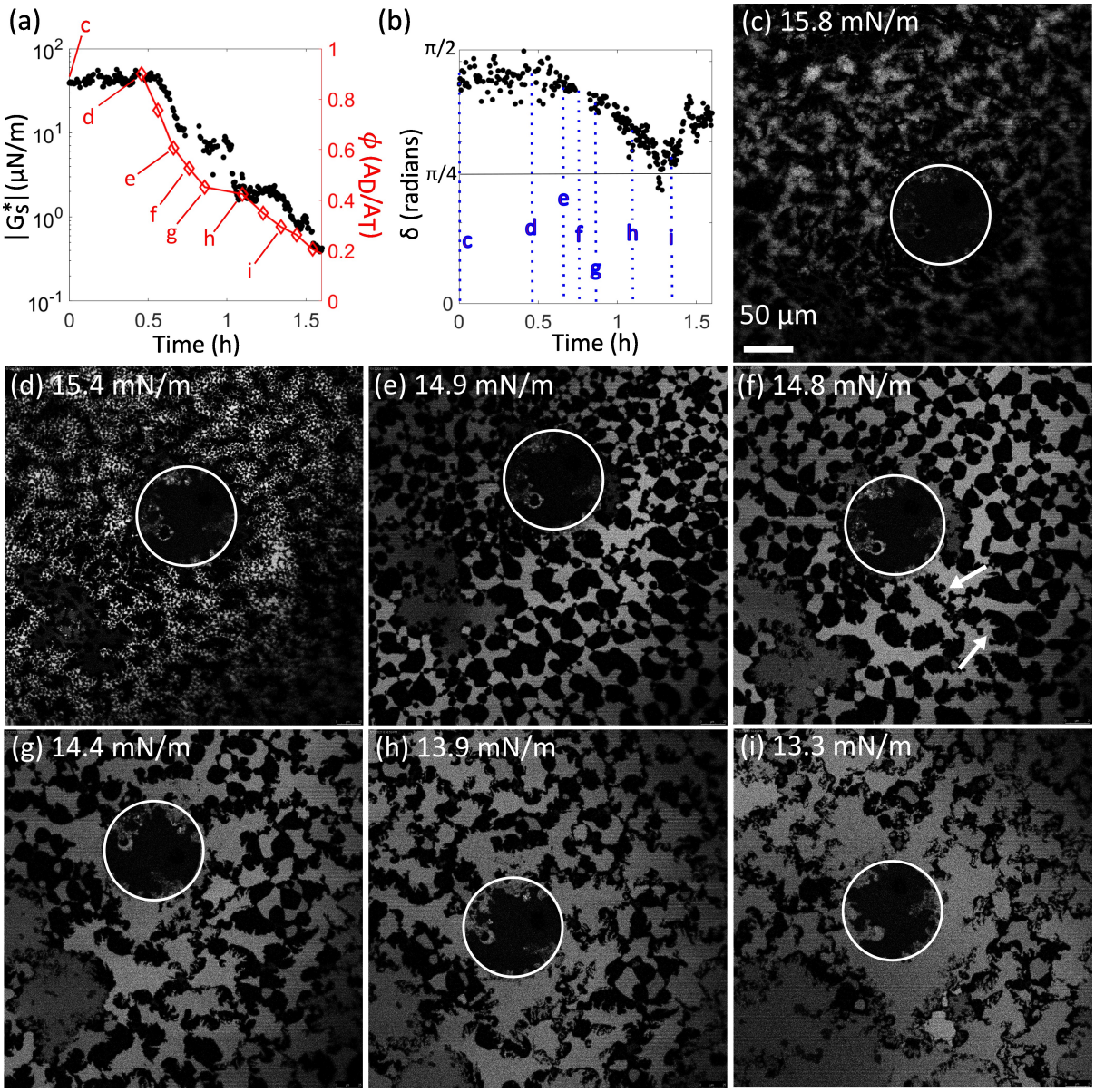

Figure 3.8: Rheology-morphology connection during PLA_2-catalyzed degradation of a single monolayer. (a) Interfacial viscoelastic shear modulus $|\ G_s^*\ |$ (filled circles) and condensed phase area fraction ϕ (unfilled diamonds) versus time since PLA_2 injection. (b) Phase angle δ versus time since PLA_2 injection. In (a) and (b) Letters indicate the time points of respective fluorescence micrographs (c-i). (c) LC-DPPC monolayer and microbutton probe (outlined) prior to PLA_2 injection. (d-i) Monolayer undergoing morphology transitions throughout PLA_2-catalyzed degradation process. Microbutton probe outlined.

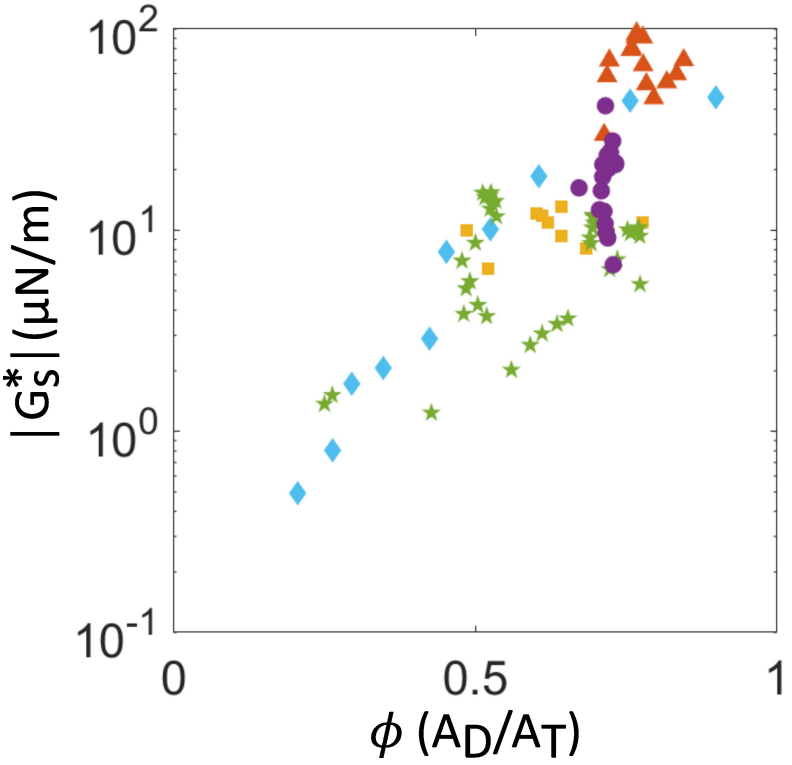

Figure 3.9: Interfacial viscoelastic shear modulus $|G_s^*|$ versus condensed phase area fraction ϕ for multiple PLA_2-catalyzed degradation experiments. Each symbol indicates a separate experiment. $|G_s^*|$ is only plotted for the duration where microbutton probe is in contact with condensed phase.

aggregation, network percolation, and coarsening (Fig. 3.8d-3.8e). Notably, δ first starts to decrease around the onset of solidification, as seen in Figure 3.8f. The phase angle continues to decrease as the solidification transition progresses, meaning that the network is becoming more elastic. The elastic character continues to increase (δ decreases) even while the network is eroding and the modulus $|G_s^*|$ is decreasing (Fig. 3.8g-3.8h). The phase angle reaches an apparent minimum just before Figure 3.8i, and are anisotropically distributed (i.e. between 45-180°). These connections further erode as δ increases, with images (micrographs provided in Fig. B.5) showing transitions to two and ultimately one point of contact with the network. Given that the assumptions used to interpret the rotational resistance of the microbutton in terms of the surface rheology of the film

(i.e. rotationally symmetric deformation) do not hold in these later stages, the increase in phase angle is likely an artifact of the technique.

The degradation experiment in Figure 3.8 occurred over several hours due to the relatively old PLA_2; as discussed in the previous section, fresher PLA_2 is more active and degrades monolayers much more quickly. Nonetheless, the solidification transition coincides with the onset of increasing elasticity (i.e. onset of decrease in δ), as demonstrated in Figure 3.10. In other experiments with differing ages of PLA_2 samples, the time at which δ begins to decrease (t_δ) is plotted against the time at which domain solidification is first observed (t_{solid}). Differences in timescales are due to the age of the PLA_2 sample used in each experiment; fresher PLA_2 corresponds to an earlier solidification transition. Despite differences in the transition timescales, the relationship between solid-like domain morphology and increasing elasticity is maintained. We thus conclude that the onset of domain solidification triggers the appearance and growth elasticity in the network.

3.4 Discussion and conclusions

Here we discuss the roles of each component (DPPC, PLA_2, PA, and LPC) in the degradation process, as inferred from the morphology and rheology results. Prior to degradation, the interface is predominantly LC-DPPC. PLA_2 begins degrading DPPC at the LE-LC phase boundary, introducing PA and LPC. Previous work has demonstrated that PA co-crystallizes with DPPC at near-zero surface pressure [28]. Thus, we expect that the new PA is co-crystallizing at the phase boundary where it is produced. DPPC-PA co-crystal domains are known to be more compact in shape than pure DPPC (Fig. 3.11)—likely reflecting the decrease in tilt angle of the aliphatic chains that is responsible for the characteristic shape of DPPC domains[28]—which may contribute to the transition towards more compact domains in the actively degrading system.

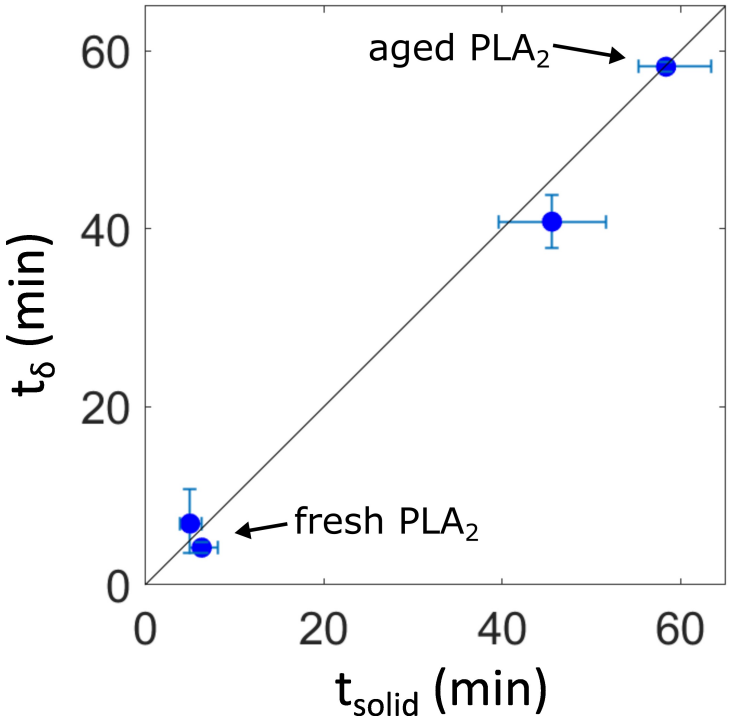

Figure 3.10: Time point t_δ at which phase angle δ begins to decrease versus the time point t_{solid} where solidification is first observed in the morphology. Solid line corresponds to $t_\delta = t_{solid}$, which matches data for both fresh and aged PLA_2.

The addition of PA alone does not explain other morphology transitions, such as domain aggregation and network percolation. Both pure DPPC domains [47, 45], and DPPC-PA co-crystal domains [28, 31] exhibit electrostatic domain-domain repulsion. Aggregation in the degrading monolayer therefore implies that the electrostatic repulsion is reduced, with some other component (buffer, PLA_2, or LPC) playing a key role. The effective electric field around each domain is a combination of the electrostatic properties of the aqueous electrolyte below, the surfactants comprising the condensed and expanded phases of the monolayer, and the air above. Focusing on the domain itself, factors including composition (e.g. headgroup properties) as well as structure (e.g. molecular packing and tilt orientation) influence the dipole density [47, 53]. In what follows, we briefly enumerate possible mechanisms by which the additional components—i.e. buffer ions, PLA_2, and LPC—might promote domain aggregation.

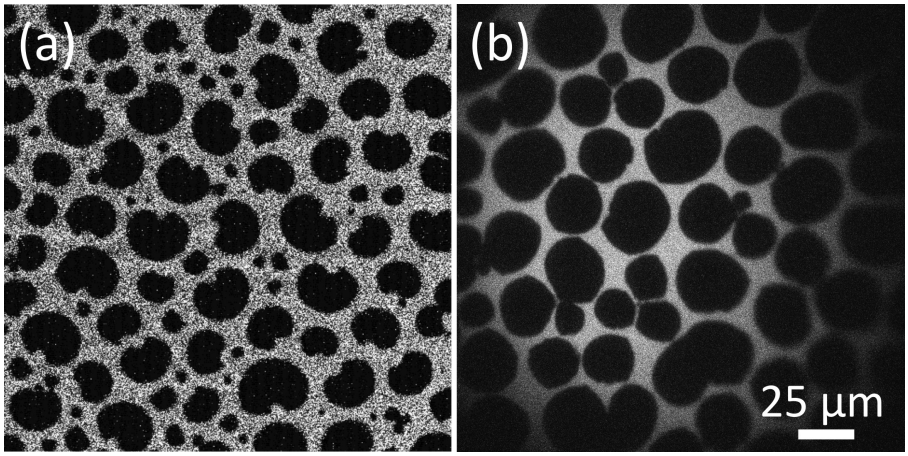

Figure 3.11: Fluorescence micrographs of DPPC (a) and 4:1 (mol) of DPPC:PA (b) at $\backsim$ 11 mN/m. DPPC:PA co-crystal domains have more compact shape than bean-like shape common for DPPC domains.

Additional monolayer components provide a variety of plausible ways in which the electrostatic repulsion between domain can be reduced, yielding the domain aggregation observed in Figure 3.4. The subphase buffer itself affects domain shape and interactions — e.g. the electric double-layer screening impacts the magnitude of the dipole density and the field distributions above the monolayer[47, 53, 54], although neither DPPC domains nor 4:1 DPPC:PA domains aggregate due to buffer alone (Fig. 3.11). The buffer contains divalent Ca^{2+} ions, as required for PLA_2 function, that are known to bind and even dimerize with fatty acids like PA [55]. Reducing the surface charge density of the condensed phase would influence both structure and dipole density within domains, and likely their interactions. Indeed, inter-domain distance for 4:1 DPPC:PA on buffer is much more heterogeneous than the relatively uniform separation between pure DPPC domains (Fig. 3.11), although fluorescently labelled LE phase remains visible between close neighbors, indicating the lack of domain aggregation. PLA_2 is likely located along domain boundaries [46] and even though PLA_2 is a relatively small protein ($\backsim$15 kDa) [23, 40], PLA_2 molecules are far larger than the lipids in the monolayer. The heterogeneous properties of the PLA_2 proteins likely perturb local electric fields relative to a

lipid monolayer free of proteins and could plausibly trigger aggregation. Lastly, LPC are known detergents at high enough concentrations, solubilizing lipids and increasing the permeability of liposomes by stabilizing transient pores [56, 57, 58]. LPC has also been shown to be line-active along the LE-LC phase boundaries of pure DPPC monolayers, enabling domains to maintain much more extended shapes [27]. These features suggest ways in which LPC could alter degrading domains so that dipolar repulsion does not dominate the interaction between condensed domains. Further investigation will be required to tease apart the individual roles that each of these components plays in the aggregation process.

Domains also undergo coarsening via Ostwald ripening and coalescence. Throughout coarsening, the composition at domain phase boundaries is constantly changing and it is not possible to tell from the fluorescence micrographs how much DPPC has been converted to PA and LPC. Surface shear rheology reveals interfaces to remain viscous-dominant while coarsening is occurring. We interpret this as indicating that the condensed phase domains remain predominantly DPPC during coarsening, given that pure DPPC is also viscous-dominant. As the coarsening period is slowed and eventually halted by domain solidification, the condensed network becomes increasingly elastic. We hypothesize that the transition from the viscous-dominant surface rheology (DPPC-like) to an increasingly elastic monolayer reflects domain solidification due to the increasing fraction of DPPC-PA co-crystals.

The timescale for the solidification transition is affected by the age, or activity, of the PLA_2. Fresher PLA_2 results in faster overall production of PA and thus DPPC-PA co-crystals. The faster the DPPC-PA fraction increases, the earlier the domains solidify and arrest coarsening, thereby fixing the feature sizes of the initial solid-like network. The activity of the PLA_2 may also affect the distribution of PA within domains. Slower overall degradation of the monolayer via older, less active PLA_2, gives more time for

PA to diffuse into LC-DPPC domains. It is unclear what effect more diffusion time would have on the network, but we hypothesize that the overall distribution of PA in each domain does affect the solidification transition. It is likely that the DPPC-PA co-crystals line the boundaries of condensed phase and perhaps the solidification transition becomes observable in the morphology and rheology when the DPPC-PA co-crystal layer grows to a certain thickness, acting like a "hard shell". Further investigation would be necessary to study how PA is distributed within each domain, and the effect of changing the relative rates of PA production via PLA_2 reactions versus PA diffusion within the domain.

Clearly, PLA_2-catalyzed degradation of model LS induces significant changes to the monolayer morphology and its corresponding mechanical properties. In the context of ARDS, these results suggest a plausible mechanical mechanism for lung surfactant inactivation via PLA_2 -catalyzed degradation, shown in Figure 3.12. PLA_2 is released after the initial acute lung injury. As PLA_2 degrades lung surfactant, condensed domains percolate into a 2D colloidal gel-like network that becomes increasingly stiff as the fraction of DPPC-PA co-crystals in the network increases. These relatively stiff heterogeneities would be resistant to deformations, such as the inflation and deflation of an alveolus during respiration [59]. If different alveoli in different regions of the lung inflate differently from each other, and if the remaining LS is not able to properly moderate the surface tension, the Laplace instability could cause some alveoli to collapse at the expense of others [60]. The result would be anisotropic inflation and deflation in the lung overall, reducing lung volume and compliance, and possibly triggering localized lung flooding (edema). In principle, PLA_2-induced heterogeneities in lung inflation and deflation could further stress the alveolar tissue, and therefore trigger an even stronger inflammatory response, releasing even more PLA_2 into the alveoli. Such positive feedback could contribute to the progressive degradation seen in ARDS.

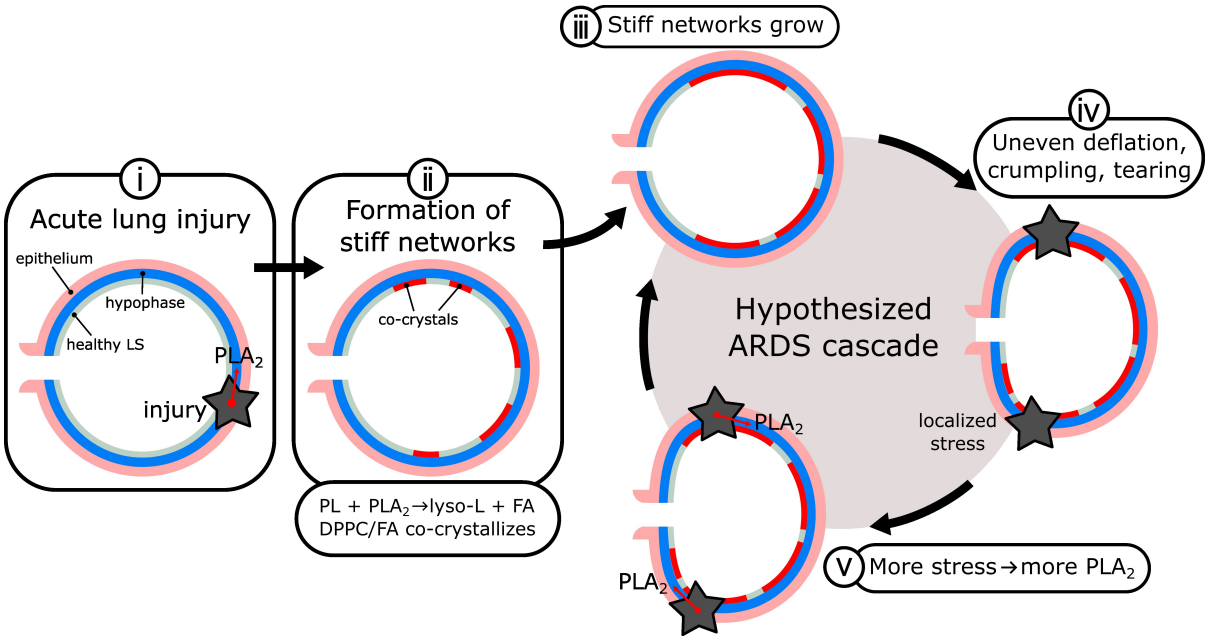

Figure 3.12: Possible mechanical mechanism for PLA_2-induced LS inactivation in ARDS. (i) PLA_2 is released after the initial acute lung injury. (ii) PLA_2 adsorbs to the interface and degrades phospholipids (PL). Resulting fatty acids (FA) co-crystallize with DPPC, forming stiff networks on the interface. (iii) Stiff networks grow as PLA_2-catalyzed degradation progresses. (iv) Stiff domains resist deformation, creating more localized stresses. Resistance to deformation could lead to uneven deflation, buckling, or monolayer fracture in the alveoli. (v) Increased alveolar stress triggers the release of more PLA_2.

3.5 Note on the content pertaining to this chapter

Chapter 3; Appendix B; and the relevant portions of the abstract, Chapter 1, and Chapter 2 are based on a manuscript under consideration for publication in the archival literature.

Chapter 4

Monolayer morphology and rheology of DPPC, HD, and DChol mixtures evolve with DPPC phase behavior

4.1 Introduction

Neonatal respiratory distress syndrome (NRDS) is a pulmonary disease that can occur in premature infants, primarily affecting infants under 32 weeks of gestation [2]. Approximately 60,000 premature infants are at risk of NRDS in the US annually [2]. The underlying cause of NRDS is an insufficient amount of functional type II pneumocytes, the cells responsible for LS production [2]. As a result, NRDS patients are unable to produce enough LS for healthy respiration. The pathophysiology of NRDS includes alveolar collapse, overdistension, decreased lung compliance, and pulmonary edema [2]. Prior to the development of effective therapies, NRDS was the major cause of infant mortality in the US and other developed nations [2]. Since the implementation of lung surfactant replacement therapy (SRT) alongside intensive care, the outcome of premature

infants has greatly improved [2, 9]. SRTs are exogeneous surfactant mixtures, composed of lipids and proteins typically extracted from bovine or porcine lungs. There are multiple SRTs in use today (e.g. Infasurf, Curosurf, and Survanta) and each is prepared using a different method. For example, Infasurf is processed from lavaged calf LS while Curosurf is processed from porcine lung tissue [2]. SRTs have also been manufactured synthetically, which has the advantage of more control over the composition than animal-derived methods. As a result of the different SRT preparation methods, the compositions and interfacial properties of each SRT are different. Clinical comparisons between SRTs have shown that each formula improves aspects of lung performance (e.g. gas exchange) to differing degrees. Additionally, clinically tested synthetic SRTs were found to be less efficacious than animal-derived SRTs [2]. However, the biophysical mechanisms behind the different SRT performances are not well-understood.

Studying the surface behavior of SRT components ex situ enables measurements that are not accessible in clinical settings, such as surface morphology and rheology. This investigation is motivated by the idea that characterizing the surface behavior of components currently used in SRTs will provide insight into the function of SRT formulas. Here, we build upon the previous work of Valtierrez-Gaytan et al., studying the morphology of DPPC, HD, and DChol mixtures [31]. Each of these components, apart from DChol, are used in one or more SRTs and are present in different amounts depending on the given SRT [2]. DChol is used here as a proxy for cholesterol, which is present in some SRT formulas. In this investigation we track the phase behavior, morphology, and rheology of 5:1 DPPC:HD monolayers with and without DChol. The surface rheology of these mixtures is dependent on the condensation of excess DPPC; monolayers become more difficult to shear and the relative elasticity is highly Π-dependent as excess DPPC condenses. When comparing the monolayers with and without DChol, monolayers with DChol are easier to shear at high Π, after the excess DPPC has condensed. These re-

sults provide some insight into the relationship between SRT composition and surface mechanics. Going forward, this approach could be expanded to more mixtures of DPPC, HD and DChol as well as other SRT components, such as LS apoproteins and synthetic additives.

4.2 Experimental methods

4.2.1 Equipment cleaning and monolayer preparation

The two samples used in this investigation were prepared by Dr. Cain Valtierrez-Gaytan, using the materials and methods described elsewhere [31]. One sample is composed of 1,2-Dipalmitoyl-sn-glycero-3-phosphocholine (r-DPPC, R-enantiomer) mixed with hexadecanol (1-HD) at a molar ratio of 5:1. The other sample contains 1,2-dipalmitoyl- rac-glycero-3-phosphocholine (rac-DPPC) mixed with 1-HD at a molar ratio of 5:1, and 1.5 mol% dihydrocholesterol (DChol). Dihydrocholesterol was used in place of cholesterol to minimize oxidation and was reported to have a negligible effect on monolayer phase behavior and morphology when compared against cholesterol [47, 31]. Both samples are in chloroform solution and contain 0.75 mol% Texas Red DHPE. Samples are refrigerated (3 °C) between experiments. Prior to use, the sample vials were acid-cleaned by Dr. Cain Valtierrez-Gaytan using the procedure in Appendix A.

Before each experiment the ribbon-barrier trough (Fig. 2.1) is first cleaned as described in Appendix A. The magnet holder in this investigation is made with polypropylene and cleaned as described in Appendix A. The subphase is ultrapure water (Milli-Q) to ensure that results in this investigation are consistent with the results reported by Valtierrez-Gaytan et al. To prepare a monolayer, a sample is deposited dropwise on the air-water interface using a cleaned gas tight syringe. The monolayer is left undisturbed

for an hour to allow the chloroform to evaporate and the monolayer to equilibrate. Monolayer tempeartures are recorded, but not controlled. Morphology and surface pressure are measured as described in Chapter 2.

4.2.2 Surface rheology and alignment of stripe domains

Rheology measurements are conducted using the microbutton microrheometry technique as described in Chapter 2. The stripe alignment demonstration also utilizes a microbutton probe and the external magnetic field. The magnetic field setup, with oppositely aligned magnetic coils connected in series, is not able to controllably spin a microbutton at a constant rate. Although, if the maximum allowable current is applied when producing the sinusoidal magnetic field and the drag from the monolayer on the probe is sufficiently low, the microbutton will spin, just not at a constant rate. For the stripe alignment demonstration, the monolayer was compressed into the stripe regime and but the surface pressure was intentionally kept low to minimize drag on the probe from the monolayer.

4.3 Phase behavior and morphology of 5:1 DPPC:HD with and without Dchol

Figure 4.1a is a representative Π-A isotherm of 5:1 r-DPPC:HD, capturing the phase behavior of the monolayer. Unlike pure DPPC, DPPC:HD co-crystals condense at immeasurably small surface pressures (Fig. C.1) and exhibit a compact shape. At low surface pressures, DPPC:HD domains grow at a fixed stoichiometry of 2:1 DPPC:HD until the HD is depleted from the disordered LE phase [31]. Like pure DPPC, DPPC:HD co-crystals exhibit electrostatic domain-domain repulsions [28, 29, 31]. Figure 4.1b shows

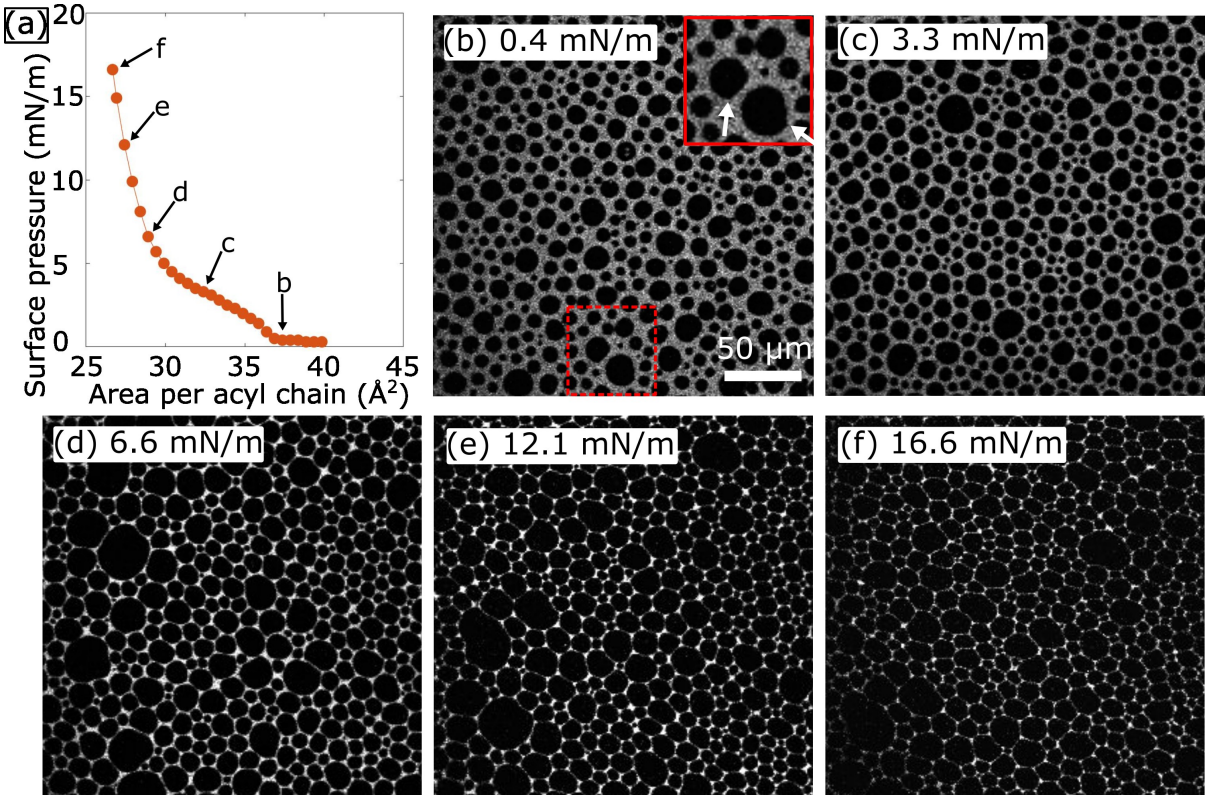

Figure 4.1: Representative isotherm (a) and morphology (b-f) of 5:1 r-DPPC:HD monolayer on an air-water interface at 21 °C. 2:1 DPPC:HD co-crystals condense at ∽ 0 mN/m [31]. (b) DPPC:HD co-crystals in continuous LE-DPPC. Inset zooms in on area outlined in red-dashes. White arrows point at examples of domain cusps. (c) Area fraction of condensed phase increases as excess DPPC begins condensing onto existing DPPC:HD co-crystals. (d) Nearly all excess DPPC has fully condensed onto the DPPC:HD co-crystals. (e-f) Fully condensed 5:1 r-DPPC:HD monolayer is compressed to higher surface pressures.

discrete, repulsive DPPC:HD co-crystals in a continuous disordered phase. The bright, disordered phase in Figure 4.1b is made up of excess DPPC and the fluorescently labeled DHPE. The Figure 4.1b inset shows a close-up of the asymmetric r-DPPC:HD domain morphology; the domains have a cusp at one end (arrows) and a rounded side on the opposite end. As described by Valtierrez-Gaytan et al., the cusp is likely due to local differences in line tension, arising from heterogeneity in the tilt orientation of the chiral DPPC molecules [31, 53]. As the monolayer is compressed to 3-4 mN/m, the interface reaches the surface pressure at which excess DPPC in the disordered phase starts

to condense; 3-4 mN/m is the approximate onset surface pressure of the LC-LE coexistence plateau for pure DPPC at these experimental conditions. Consistent with the observations of Valtierrez-Gaytan et al., no new domains nucleate as the excess DPPC condenses, meaning that the DPPC likely grows epitaxially on existing domains [31]. While compressing through the DPPC LC-LE coexistence regime, the area fraction of the condensed phase increases and the monolayer becomes fully condensed as shown in Figure 4.1c-d.

The addition of 1.5 mol% DChol to the same 5:1 ratio of rac-DPPC:HD produces entirely different phase behavior, as shown by the representative Π-A isotherm and micrographs in Figure 4.2. Like the case with no DChol, rac-DPPC:HD co-crystals condense at near-zero surface pressures until the HD is depleted from the surrounding disordered phase. Figure 4.2b shows the compact shaped rac-DPPC:HD co-crystals surrounded by excess LE-DPPC. The compact domain morphology is somewhat different for the racemic DPPC mixture. The rac-DPPC:HD domains are axisymmetric, but still have a single cusp (Fig. 4.2b inset) like the r-DPPC:HD domains in Figure 4.1b. The line-active Dchol is excluded from the co-crystals, remaining in the disordered phase, preferentially located along the phase boundaries of the condensed domains [31]. As the monolayer is compressed from Figure 4.2c to 4.2d, domains begin to elongate uniaxially. As characterized by Valtierrez-Gaytan et al., when the monolayer reaches the onset of LC-LE DPPC coexistence, the domains undergo a fingering instability on both sides and begin to change shape [31]. Following Figures 4.2d to 4.2g, the discrete domains elongate symmetrically from end to end, evolving from a compact to high-aspect ratio stripe morphology. The cusp is preserved throughout the stripe transition, although it is difficult to resolve at the magnification used in this investigation [31]. The combination of line-active DChol and enrichment of DPPC at the domain boundaries, lowers the line tension, inducing the fingering instability and eventual transition into stripes [31].

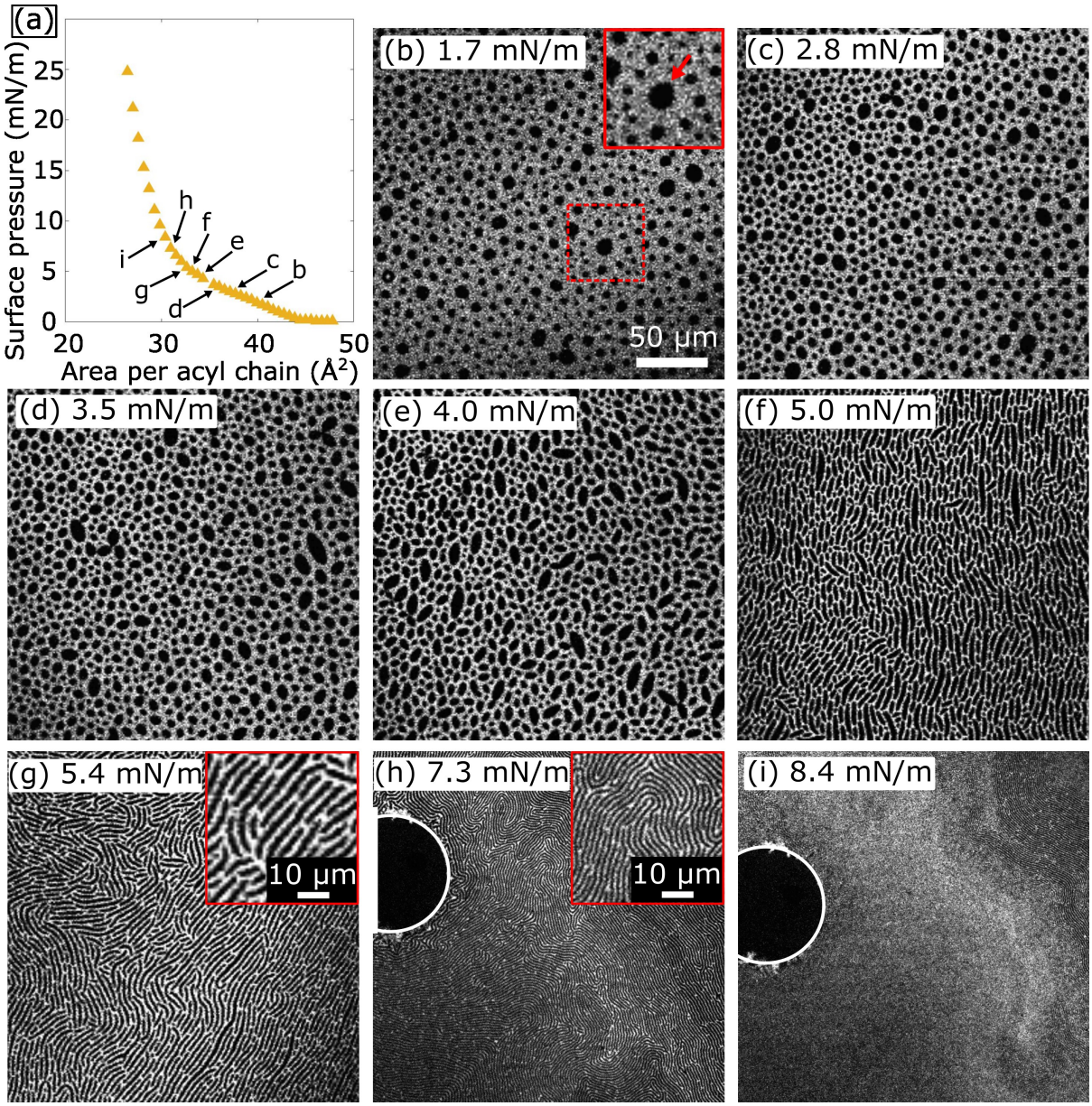

Figure 4.2: Representative isotherm (a) and morphology (b-i) of 5:1 rac-DPPC:HD + 1.5 mol% DChol monolayer on an air-water interface at 21 °C.(b) 2:1 rac-DPPC:HD co-crystals in continuous LE-DPPC. Inset zooms in on area outlined in red-dashes, showing axisymmetric domains with a cusp (red arrow) on one end. (c) Area fraction of condensed phase increases as excess DPPC begins to condense on existing DPPC:HD co-crystals. (d-g) Onset of the stripe transition; domains begin to elongate symmetrically from end to end, evolving into stripe domains of uniform width. (g) Inset shows stripe domains of uniform width ($\backsim$ 2 μm). (h) As Π increases, stripe width decreases. Microbutton probe outlined in white. Inset shows stripe domains of $\backsim$ 0.8 μm. (i) After sufficient compression, the stripe width shrinks below the limit of resolution.

Notably, the stripe domains in Figure 4.2g have a uniform width ($\backsim$ 2 μm) unlike the initial domains (Fig. 4.2b) and even pure DPPC domains, which are both polydisperse in size. Valtierrez-Gaytan et al. determined that the stripe width is dependent on temperature, surface pressure, and the DPPC:HD ratio. As the surface pressure is increased from Figure 4.2g to 4.2h, the stripe width decreased to $\backsim$ 0.8 μm. With further compression, the stripe width shrinks to below the limit of resolution, as shown in Figure 4.2i. Consistent with the observations of Valtierrez-Gaytan et al., larger stripe widths are easily recovered by decompressing the monolayer [31]. Figure C.2 walks through a decompression-compression cycle between the two stripe widths in Figure 4.2h and 4.2g, demonstrating that the changes in stripe dimensions are reversible.

Another feature of the stripe domain morphology is that stripe domains orient in the direction of surface flows. Surface convection, possibly due to air currents, is commonly observed in experiments; while in the LC-LE coexistence regime domains are seen continuously flowing in a single direction inside the cone. When such surface convection occurs, stripe domains orient lengthwise in the direction of bulk flow as shown in Figure 4.3a (solid arrows). Figure 4.3a (dashed arrows) also demonstrates that stripe domains will orient in the direction of flow around a solid inclusion on the interface (e.g. microbutton probe). The stripe domains can be realigned by imposing flow fields using a microbutton probe. For example, Figure 4.3b-4.3d follows the change in stripe domain orientation while rotationally shearing the interface with a microbutton probe. Figure 4.3b shows the monolayer prior to shearing, where the inset shows the stripe domains aligned in the direction of bulk surface flow (arrows) for the region outlined in the dashed box. In Figure 4.3c, the probe has been rotating counter-clockwise for $\backsim$2 min and the inset shows stripe domains aligned in the direction of shear. Interestingly, the fluorescence intensity is concentrated near the rotating probe and concentrates more with further rotation (Fig. 4.3d). Figure 4.3d shows the interface after $\backsim$2 more minutes of probe rotation; the flu-

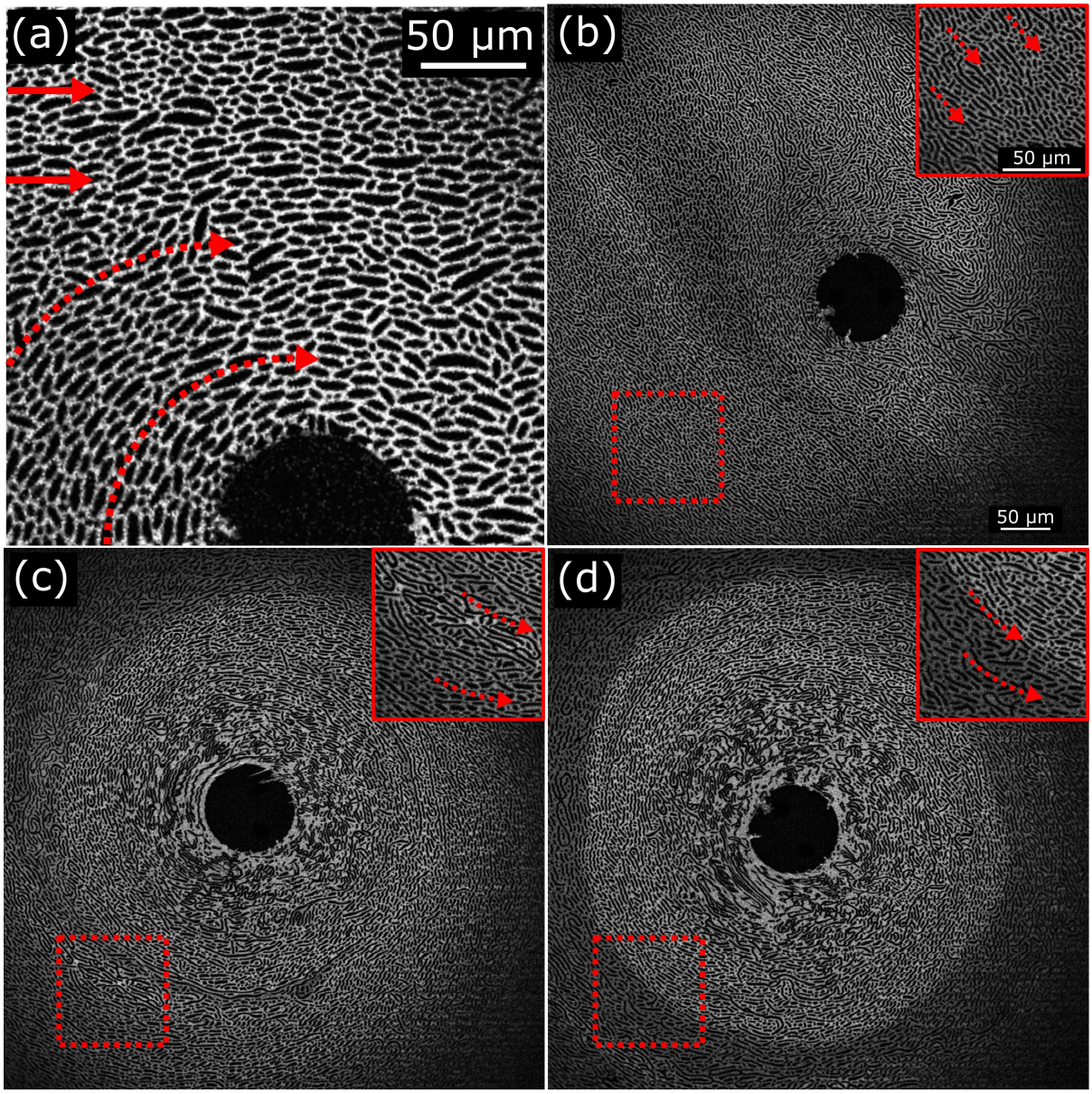

Figure 4.3: Demonstration of stripe domain alignment (a) and re-alignment (b-d). All insets correspond to the area outlined in the respective dashed boxes. (a) Stripe domains align in the direction of bulk surface flow (solid arrows) and reorient and flow around solid inclusions such as a microbutton probe (dashed arrows). (b) Stripe domains prior to rotating microbutton probe. Domains in inset are aligned in the direction of bulk surface flow (dashed arrows). (c) Monolayer after $\backsim$ 2 min of rotating the microbutton probe counter-clockwise. Fluorescence intensity is concentrated near the rotating probe. Inset shows stripe domains aligned in the direction of shear (dashed arrows). (d) Monolayer after $\backsim$ 4 min of counter-clockwise probe rotation. Fluorescence intensity is concentrated near the probe and there is a visible boundary in fluorescence in intensity. Inset shows fluorescence boundary and stripe domains aligned in the direction of shear (dashed arrows).

orescently labeled TR-DHPE has become so concentrated near the center that there is a visible boundary in fluorescence intensity outlining the concentrated region.

4.4 Surface shear rheology of 5:1 DPPC:HD with and without DChol

Similar to pure DPPC, the surface shear rheology of 5:1 r-DPPC and 5:1 rac-DPPC:HD +1.5 mol% Dchol depends on the respective phase behavior. Figure 4.4 shows the surface shear rheology and corresponding morphology for two representative monolayers at each composition. The linear, viscoelastic surface shear modulus $| G_s^* |$ is plotted against Π in Figure 4.4a. Only $| G_s^* | > 0.2$ μN/m is reported (denoted by dashed line), below which the rheology is subphase-dominated and can't be distinguished from a clean interface without surfactant. Both monolayer compositions span approximately three orders of magnitude in $| G_s^* |$ for the range of Π tested but differ when compared at a given Π. For example, $| G_s^* |$ begins to rise appreciably near $\Pi \approx$ 3-4 mN/m for the 0 mol% DChol case (Fig. 4.4c). Alternatively, $| G_s^* |$ rises at $\Pi \approx 5$ mN/m for 1.5 mol% DChol (Fig. 4.4e). Since the stripe transition occurs below $\Pi = 5$ mN/m, this measurement does not provide insight on how surface rheology changes during the stripe transition. Interestingly, even though the domain morphologies are different between the two compositions at the respective Π when $| G_s^* |$ rises, the area fractions of the condensed phase ϕ are equal ($\phi \approx 0.6$).

The initial rise in $| G_s^* |$ for each composition lies within the range of Π for which excess DPPC is expected to condense. As each monolayer is compressed further and more DPPC condenses, $| G_s^* |$ grows exponentially. $| G_s^* |$ at each composition approaches the same magnitude while compressed through DPPC LC-LE coexistence, overlapping close

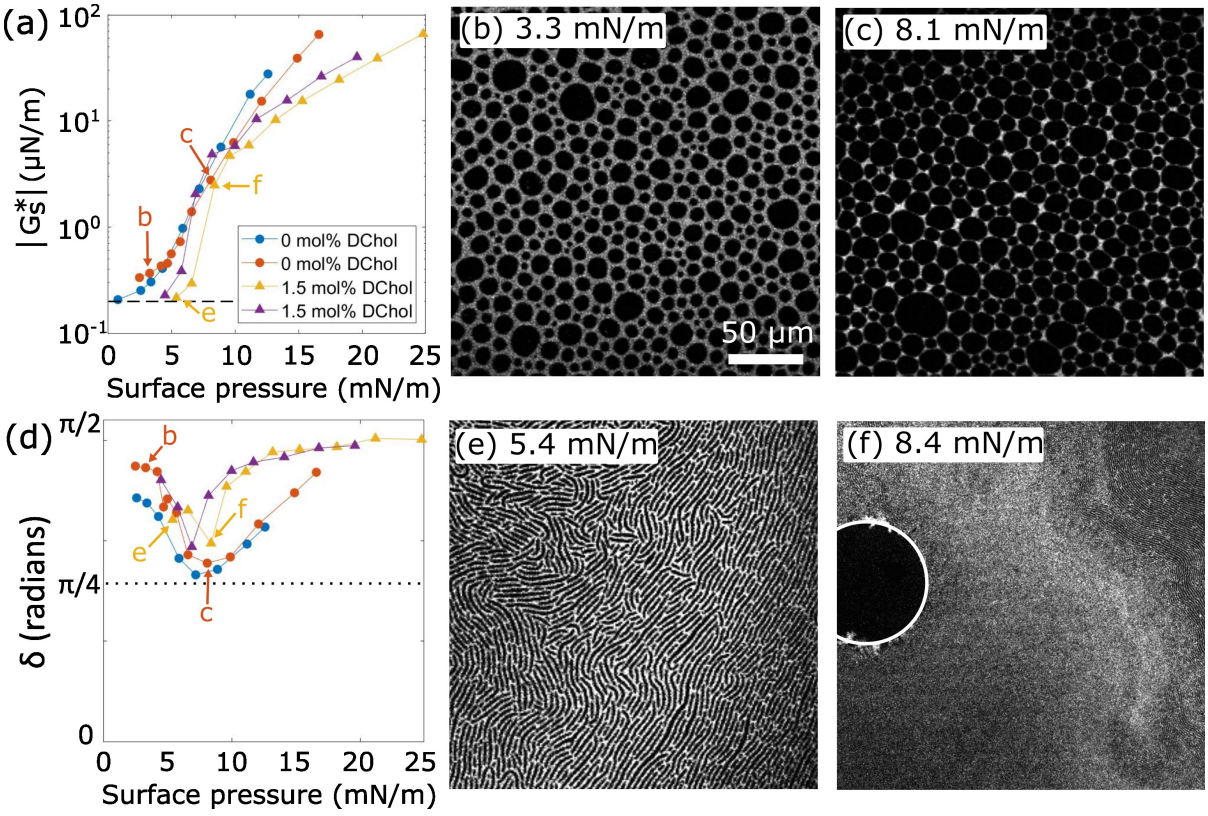

Figure 4.4: (a) Representative surface shear rheology and fluorescence micrographs of 5:1 DPPC:HD with 0 mol% DChol and 1.5 mol% DChol. (a) Linear, viscoelastic surface shear modulus $|\ G_s^*\ |$ is plotted against Π for each monolayer composition. (b-c) Monolayer morphology of 5:1 DPPC:HD + 0 mol% DChol near the initial rise in $|\ G_s^*\ |$ (b) and when the monolayer is fully condensed (c). (d) Phase lag δ for same monolayers as (a), plotted against Π. (e-f) Monolayer morphology of 5:1 DPPC:HD + 1.5 mol% DChol near the initial rise in $|\ G_s^*\ |$ (e) and and when the monolayer is fully condensed (f).

to the range where excess DPPC is expected to be fully condensed, near $\Pi \approx 8$ mN/m (Fig. 4.4c and 4.4f). Beyond $\Pi \approx 8$ mN/m, $\mid G_s^* \mid$ continues to increase for both compositions, but with a weaker exponential. In the fully condensed regime, $\mid G_s^* \mid$ is greater for the 0 mol% Dchol case at a given surface pressure. Although the 0 mol% DChol measurements do not exceed 17 mN/m due to experimental limitations, based on the trajectory of $\mid G_s^* \mid$, the trend of $\mid G_s^*(\Pi) \mid$ being greater is expected to continue. Therefore, fully condensed DPPC:HD monolayers containing Dchol are easier to shear than DPPC:HD monolayers without Dchol.

Figure 4.4d plots the corresponding phase lag δ for the same representative monolayers in Figure 4.4a. For each monolayer composition the surface shear rheology is viscous-dominant, although δ does change with surface pressure. For each composition, δ decreases (i.e. relative elasticity increases) as the monolayer is compressed through the DPPC LC-LE regime. The relative elasticity of each monolayer reaches a maximum at $\Pi \approx 8$ mN/m, near where excess DPPC is expected to be fully condensed (Fig. 4.4c and 4.4f). For the 1.5 mol% DChol case, δ is slightly higher at $\Pi \approx 8$ mN/m, meaning that the relative elasticity does not increase as much for the DChol-containing monolayers. With further compression δ rises for each composition, exhibiting an increasingly viscous-dominant response. δ is greater for the 1.5 mol% DChol case in this Π regime and reaches a plateau around 15 mN/m. The 0 mol% DChol δ does not reach a plateau for the range of Π measured.

4.5 Discussion and future directions

The surface rheology of 5:1 DPPC:HD monolayers with and without DChol exhibit a dependence on the condensation of excess DPPC. The initial rise in $\mid G_s^* \mid$ begins after DPPC starts to condense and the area fraction of the condensed phase reaches $\phi \backsim 0.6$,

which occurs at higher Π in the presence of DChol. Like a pure DPPC monolayer, $|G_s^*|$ grows most rapidly in the DPPC LC-LE regime and then grows with a weaker exponential for Π above the LC-LE regime [41, 37]. Throughout the fully condensed regime, $|G_s^*|$ is greater for monolayers without DChol, meaning they are more difficult to shear at those surface pressures. Each of these observations are consistent with previous measurements of 3:1 DPPC:HD for a range of Dchol fractions. The 3:1 DPPC:HD data, provided courtesy of Dr. Ian Williams, is plotted in terms of surface viscosity versus surface pressure in Figure 4.5a. The surface viscosities for the same monolayers from Figure 4.4 are displayed in Figure 4.5b. No morphology or temperature was recorded for the 3:1 DPPC:HD, so it is challenging to compare the two DPPC:HD mixtures quantitatively. Both ratios of DPPC:HD exhibit similar patterns in the growth of μ_s and the addition of DChol does lower μ_s in the fully condensed regime.

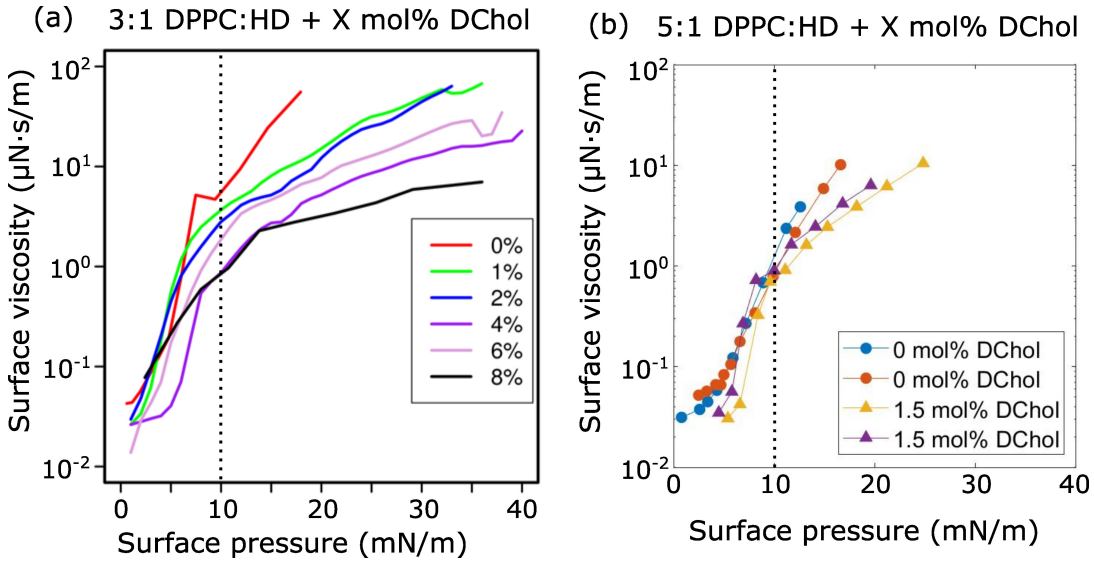

Figure 4.5: (a) Surface viscosity μ_s of 3:1 DPPC:HD + DChol ranging from 0-8 mol%, plotted against Π. (b) Surface viscosity plotted against Π for the same 5:1 DPPC:HD monolayers with 1.5 mol% DChol and without DChol as in 4.4.

Going forward, it would be worthwhile to repeat these surface rheology and morphology measurements across multiple ratios of DPPC:HD, also spanning a wide range

of DChol mol fractions. Based on the morphology data reported by Valtierrez-Gaytan et al., the area fraction of DPPC:HD co-crystals at a given Π decreases as the ratio of DPPC:HD increases. If the observation of $\mid G_s^* \mid$ growing after a condensed phase area fraction of ≈ 0.6 holds true for other DPPC:HD compositions, then increasing ratios of DPPC:HD would be expected to shift the initial rise of $\mid G_s^* \mid$ to higher surface pressures for a fixed temperature. It would be worthwhile to investigate how the relationship between surface rheology and domain area fraction is affected by adding DChol. Additionally, since domain area fraction increases as the DPPC:HD ratio decreases for a given Π, the surface rheology of domains undergoing the stripe transition might be accessible at ratios lower than 5:1 DPPC:HD. If not, the rheology of the stripe transition could be explored by adjusting probe sensitivity with smaller diameter probes. Alternatively, it might be possible to quickly compress a monolayer into a sufficiently high area fraction faster than the domains transition to stripes.

The changes in δ relative to surface pressure also follow the phase behavior of DPPC. For both compositions, the relative elasticity increases as the excess DPPC condenses. At the onset of DPPC condensation, the electrostatically repulsive domains are still dispersed in the LE phase. As the separation between domains decreases, the initial rise in relative elasticity may arise from domain-domain repulsions during shear. For both compositions, δ reaches a minimum near the end of the LC-LE DPPC coexistence plateau at $\Pi \approx 8$ mN/m. Notably, DPPC under the same ambient conditions is reported to be elastic-dominant at 8 mN/m [41]. The elasticity measured in the DPPC monolayer is hypothesized to arise from the line tension λ at the domain boundaries, analogous to a concentrated 3D-emulsion [41]. At the end of the DPPC LC-LE coexistence plateau, the contact between domains is high enough that domains do not easily slide past one another under shear. At such surface pressures, shear deformation requires deforming the domains around the points of contact, which increases the domain perimeters. Thus, some

of the energy of shearing the interface goes into creating new domain perimeters, working against the line tension, which results in an enhanced elastic response. As excess DPPC condenses onto the DPPC:HD co-crystals, the domains come increasingly into contact as the monolayer reaches the end of the DPPC LC-LE coexistence plateau. At such surface pressures, the λ-mediated elasticity hypothesis may also apply to DPPC:HD monolayers with and without DChol.

Beyond $\Pi \approx 8$ mN/m, δ increases to a more viscous-dominant response for both DPPC:HD monolayers with and without DChol. The Dchol-containing monolayer δ reaches a viscous-dominant plateau around 14 mN/m ($\delta \approx 1.4$ rad). A similar trend also occurs for pure DPPC; as the surface pressure of pure DPPC exceeds 8 mN/m, δ increases until it reaches a viscous-dominant plateau around 12-14 mN/m ($\delta \approx 1.4$ rad) [41]. The plateau is hypothesized to be connected to DPPC transitioning from LC to an untilted solid condensed phase [41]. It is possible that as the excess DPPC approaches fully condensed in the DPPC:HD-containing monolalyers, the total domain perimeter per unit area becomes fixed. As the domain perimeter approaches a constant with increasing Π, the λ-mediated elasticity would also approach a constant. The elastic modulus of the 1.5 mol% DChol monolayers does reach a plateau at $\Pi \approx 8$ mN/m and the elastic modulus of the 0 mol% DChol begins to plateau near $\Pi \approx 13$ mN/m (Fig. C.3). Additionally, as the domains are more compressed, and the tilt of the alkyl chain decreases, the surface viscosity would be expected to rise. The combination of a rise in the surface viscosity and the λ-mediated elasticity approaching a constant would result in a rise in δ, like the rise observed in Figure 4.4d.

In summary, δ of 5:1 DPPC:HD monolayers both with and without DChol changes significantly with the phase behavior of the excess DPPC. Going forward, it would be worthwhile to conduct measurements across a range of DPPC:HD ratios, including 2:1 DPPC:HD, to see how the amount of excess DPPC influences δ. Since 2:1

DPPC:HD is the composition of the co-crystals, there is no excess DPPC. Thus, examining 2:1 DPPC:HD monolayers would provide insight into how δ changes with Π for just DPPC:HD co-crystals on the interface. To investigate the effect of adding DChol, a wider range of DChol mol% needs to be examined. Changing the amount of DChol will shift the onset of the stripe transition and the line-active DChol is expected to change domain line tension, which may impact the relative elasticity.

Chapter 5

Interfacial properties of discrete lipid-PEG copolymer library as a function of PEG headgroup size

5.1 Introduction

Lipid nanoparticles (LNP) are expanding as a potential delivery platform for a variety of therapeutics and are also utilized in other applications including cosmetics, food, and agriculture [5]. The first clinically approved therapy using LNP technology emerged in 1995, with several more LNP therapies approved in the decades that followed [5, 6]. More recently, LNPs have become well-known as the delivery platform used for the COVID-19 mRNA vaccines [5, 6]. LNPs come in a variety of designs, therefore compositions can vary depending on the desired morphology, but one key component of many LNPs is lipid-PEG conjugates [5]. For example, DMG-PEG2000 is one of the most widely used lipid-PEG conjugates in LNPs and consists of DMG (1,2-dimyristoyl-glycerol) coupled with a linear PEG chain of the average molecular weight 2000 g/mol [5].

Lipid-PEG conjugates exhibit several functions, such as dictating particle size as well as preventing particle aggregation [6]. The PEG moiety has low nonspecific binding and sterically blocks access to the LNP surface, extending the blood circulation lifetime of LNPs [5, 6, 32]. However, one drawback of commercial lipid-PEGs, such as DMG-PEG2000, is the polydispersity of the PEG chains [32]. Polydispersity leads to batch differences and thus variation in the physical properties critical to the efficacy of LNPs in the human body. Moreover, varying compositions makes it difficult to study lipid-PEG properties, such as assembly, for biomedical use or any other application. Addressing the issue of polydispersity, Chen et al. recently developed a synthesis strategy to produce discrete libraries of lipid-PEG conjugates [32]. Using this strategy, lipid-PEG conjugates with monodisperse PEG headgroups are isolated and physical properties can be characterized as a function of headgroup structure.

The library of lipid-PEG conjugates, or graft copolymers, studied in this investigation were provided by Dr. Junfeng Chen, prepared using the aforementioned synthesis method [32]. The chemical structure of the lipid-PEG copolymers is shown in Figure 5.1. The dotted blue line outlines the DMG lipid component while the dashed red line marks the PEG 4-mer monomer unit (PEG4). The naming convention for the lipid-PEG library used in this investigation is DMG-PEG4-n. The number of PEG 4-mers, n, ranges from 4 to 9 in this study, chosen to emulate the range of ethylene glycol (EG) units commonly used in biological applications [32]. Notably, the lipid-PEG conjugates in this investigation have a branched, nonlinear PEG headgroup, unlike DMG-PEG2000. A second drawback of commercial lipid-PEGS, like DMG-PEG2000, is the rising concern over anti-PEG antibodies in recent years. The prevalence of PEG in commercial products has led to an increase in pre-existing anti-PEG antibodies in the population [61, 62, 63, 64, 65]. One advantage of the branched PEG moiety used in the DMG-PEG4-n series is that it has lower anti-PEG antibody binding when compared to commercial, polydisperse

linear PEG derivatives [32].

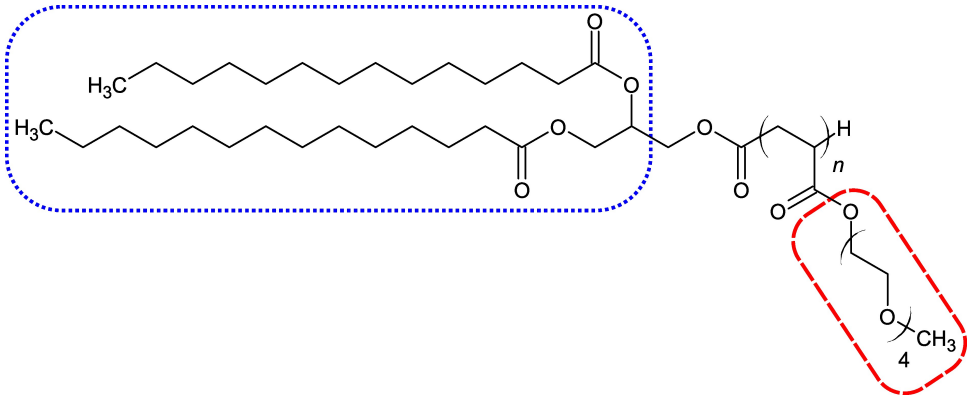

Figure 5.1: Chemical structure of DMG-PEG4-n copolymers. DMG lipid component outlined in blue dots. PEG 4-mer monomer unit outlined in red dashed. n corresponds to the number of PEG 4-mers, ranging from 4 to 9 in this investigation.

In this investigation each DMG-PEG4-n copolymer is examined as a monolayer on an air-water interface. Here, we probe interfacial properties as a function of n, or PEG headgroup size, using Π-A isotherms. When reduced to PEG surface concentration, the library of isotherms collapse onto a single curve, with some departure at higher Π. This result indicates that interactions between the PEG headgroups, as opposed to the aliphatic chains, contribute to much of the observed surface behavior.At dilute concentrations, copolymers with larger headgroups occupy more area on the interface. As the DMG-PEG4-n copolymers contact and interpenetrate at semi-dilute concentrations, each species exhibits traits of a 2D polymer in a good solvent. Lastly, at sufficiently high concentrations the energy of each monolayer reaches the respective desorption energy, which grows with the size of the PEG headgroup, and copolymers start to desorb from the interface. Clearly, the structure of PEG headgroups in lipid-PEG conjugates play a critical role in the resulting interfacial properties, which would influence the structure and function of LNPs. As LNP applications continue to grow and more lipid-PEG conjugates are developed, Π-A isotherms could be a useful tool for characterizing new lipid-PEG conjugate designs.

5.2 Experimental methods

Each DMG-PEG4 copolymer provided by Chen arrived dried. Samples were reconstituted in HPLC grade chloroform (Sigma Aldrich) and transferred to base-cleaned vials. Capped vials were wrapped in Teflon thread sealant tape and refrigerated (3 °C) when not in use. Monolayers are prepared by spreading the polymer solution dropwise from a pre-cleaned gas-tight syringe onto on an air-water interface in the custom Langmuir trough from Figure 2.1. Prior to monolayer deposition, the trough is cleaned as previously described in Appendix A and filled with an ultrapure water subphase (Milli-Q). The base-cleaning and syringe cleaning procedures are also described in Appendix A.

The trough does not have sufficient area to capture the full isotherms for the DMG-PEG4 copolymers in a single experiment. Instead, isotherms were collected in increments, meaning that different amounts of copolymer solution would be deposited to access different molecular area ranges. After deposition, the monolayer is undisturbed for 30 minutes, allowing chloroform to evaporate and the monolayer to equilibrate. The monolayer is compressed at a rate of 0.016 cm^2/s and surface pressure is measured using a filter paper Wilhelmy plate tensiometer (Riegler and Kirstein, Germany).

The optical desorption measurement utilizes a free-floating microfabricated deflection tensiometer (Fig. 5.2) [66]. The microtensiometer used in this investigation is made of SU-8 following the methods described elsewhere [66]. Prior to monolayer deposition, the microtensiometer was placed on the air-water interface. The microtensiometer position was secured by threading a stainless steel wire through one of the holes in the ladder structure attached to the side of the microtensiometer. The wire was fastened to the objective, preventing the microtensiometer from floating out of the field of view. Once secure, the monolayer is deposited outside the microtensiometer. The monolayer is compressed at a rate of 0.016 cm^2/s.

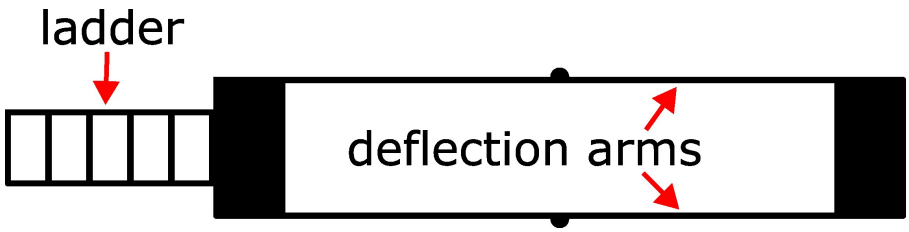

Figure 5.2: Schematic drawing of SU-8 deflection microtensiometer (not drawn to scale) [66]. Deflection arms are tracked optically to visualize the difference in surface pressure inside and outside the microtensiometer. Ladder is used to secure the position of the microtensiometer by feeding a wire through one if its holes.

5.3 Results and discussion

5.3.1 DMG-PEG4-n isotherms exhibit dependence on PEG 4-mer surface concentration

Representative Π-A isotherms for the DMG-PEG4-n series are displayed in Figure 5.3. Each isotherm follows a similar lineshape, with Π rising as A decreases until Π reaches a plateau corresponding to desorption. The series of isotherms exhibit a dependence on the size of the branched PEG headgroup, or the number of PEG 4-mer units (n). Isotherms shift to larger molecular areas as n increases, especially at lower Π, likely connected to the increasing size of PEG headgroups on the interface. Notably, the range of molecular areas observed across the DMG-PEG4-n isotherms lie above the range of pure DMG. The smallest copolymer (DMG-PEG4-4) reaches $A \approx 115$ Å^2/molecule just before the plateau while the initial onset of Π for DMG doesn't begin until $A \approx 60$ Å^2/molecule [67]. The larger molecular areas observed for the copolymers suggests that the interfacial behavior is largely dominated by the PEG headgroup, rather than the alkyl tails. Another feature of the isotherms that clearly depends on n is the plateau in Π—as n increases, the plateau Π decreases. A plateau in Π has also been observed in isotherms of PEG homopolymers, where the plateau was found to indicate desorption [36]. Clearly, the size of the branched

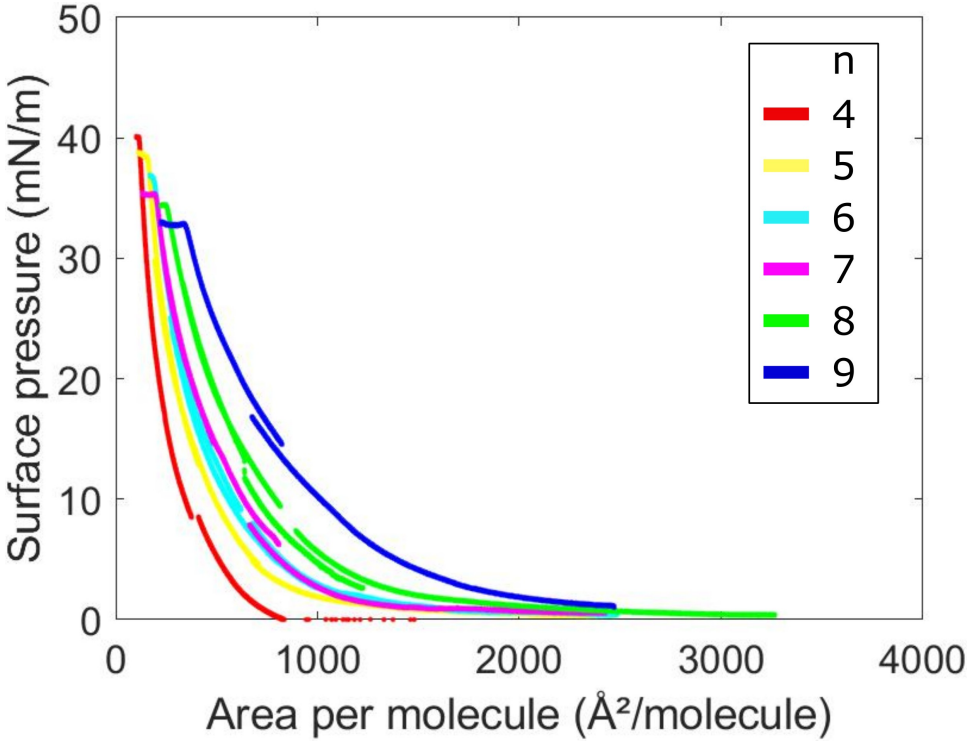

Figure 5.3: Representative Π-A isotherms of DMG-PEG4-n series at 21 °C. Each isotherm is the combination of two or more separate monolayers because the Langmuir trough in 2.1 does not have enough area to capture the full isotherm in a single experiment. Isotherms shift to larger A as n increases. Each isotherm exhibits a plateau in Π corresponding to desorption. Plateau Π decreases as n is increased.

PEG headgroup plays an important role in the interfacial behavior of the DMG-PEG4-n series. The remainder of this chapter dives deeper into the relationship between the isotherms and n, first examining the whole isotherms then followed by a closer look at different regimes: dilute, semi-dilute, and the plateau.

Going forward, the isotherms will be predominantly discussed in terms of surface concentrations (e.g. Γ, Γ_{4mer}, Γ_{peg}) and for completeness the Π-Γ isotherms are plotted in Figure D.1. To further examine isotherm dependence on n, Γ is converted to total PEG 4-mer surface concentration ($\Gamma_{4mer} = \Gamma n$) in Figure 5.4. The representative isotherms in Figure 5.4 collapse onto a single curve with some departure near the plateau. This strong dependence on n suggests that for the range of PEG 4-mer units tested the molecular

area scales linearly with the number of PEG 4-mer units ($A \backsim nA_{4mer}$). Since each monomer unit has the same amount of PEG, the isotherms would similarly fall onto a single curve when converting Γ to overall PEG surface concentration ($\Gamma_{peg} = 4\Gamma n$). One interpretation of the dependence of the isotherms on the overall surface concentration of PEG could be that the isotherms are somewhat independent of the connectivity of the PEG (i.e. branched v. linear). Although, this result may be biased by comparing only samples with the same monomer unit (PEG 4-mer). To further probe the relationship between isotherms and overall PEG surface concentration, it would be useful to test other DMG-PEGm-n series, where $m \neq 4$ but the overall number of PEG monomers is consistent with the DMG-PEG4-n series (e.g. DMG-PEG4-8 and DMG-PEG8-4 have the same total amount of PEG).

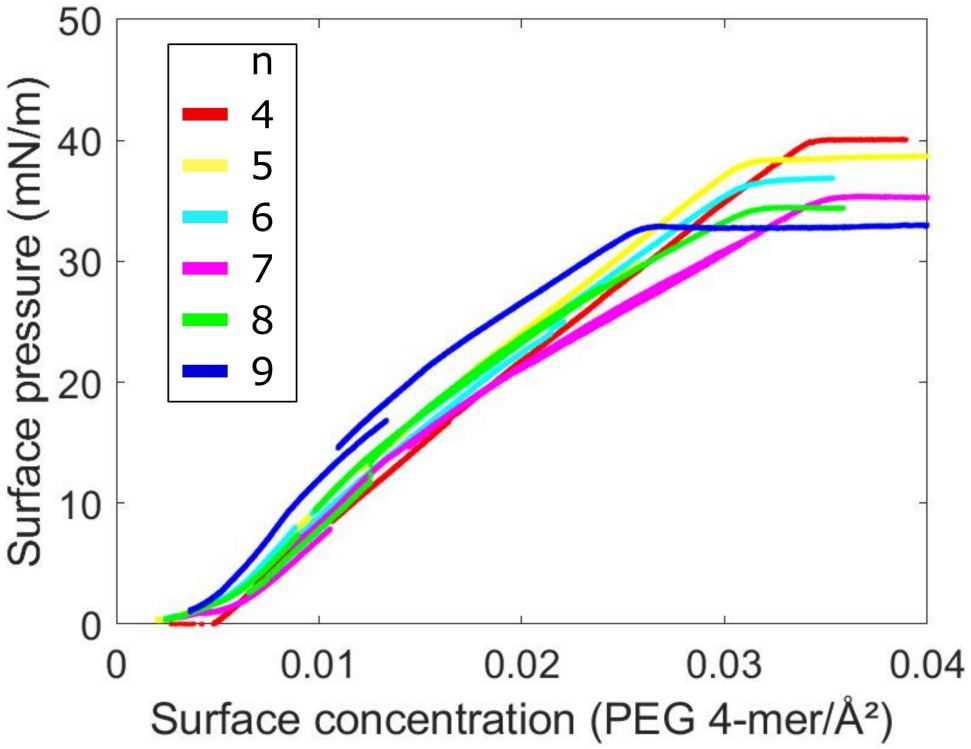

Figure 5.4: Representative isotherms from Figure 5.3 collapse onto single curve with some departure near the plateau when A is converted to Γn. Γn corresponds to PEG 4-mer surface concentration Γ_{peg}.

5.3.2 Overlap surface concentration of DMG-PEG4-n library changes with n

This next section will focus on the dependence on n in the low Π or dilute regime of each isotherm. In the dilute regime, the molecules on the interface rarely see each other. As the monolayer is compressed, the surface concentration approaches the overlap concentration, denoting the crossover from dilute to semi-dilute behavior. At the overlap concentration, polymer coils contact each other and the concentration of monomers in a coil matches the overall surface concentration of monomers. Here we estimate the overlap concentration Γ^* for each value of n, which corresponds to the approximate area A^* ($A^* = 1/\Gamma^*$) each PEG headgroup occupies on the interface before significant interpenetration with neighboring molecules.

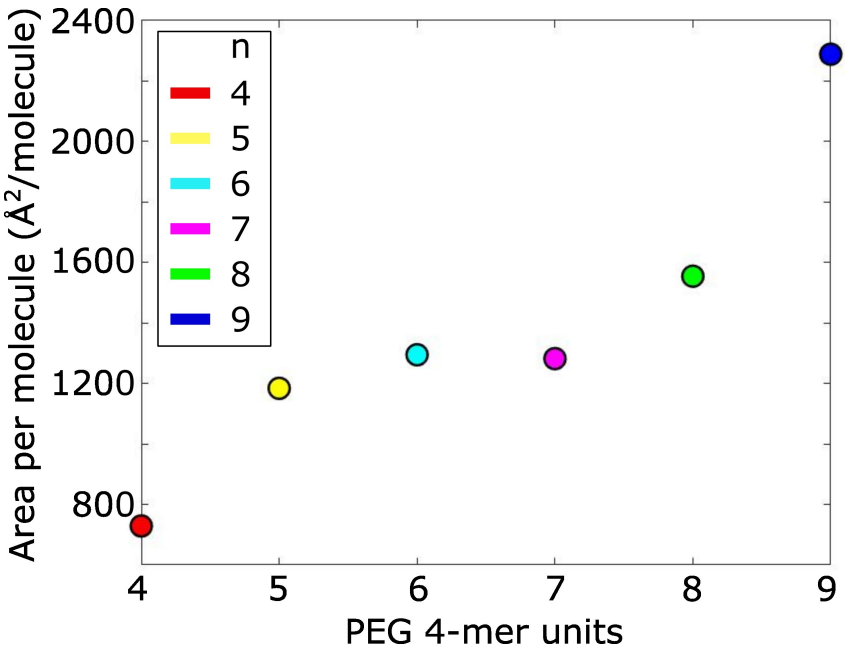

Figure 5.5: Molecular areas A^*, corresponding to the estimated overlap concentrations Γ^*, plotted for for each value of n. A^* represents the area a PEG headgroup occupies on the interface before significant interpenteration with neighboring molecules.

The approach to estimating Γ^* was simplified by approximating the dilute regime

with the 2D ideal gas isotherm ($\Pi = \Gamma k_B T$) and the semi-dilute regime with a fitted line. The surface concentration at the intersect of the two lines is taken to be Γ^*. Figure D.2 shows an example of this approach, displaying the two isotherms and the semi-dilute fitted line. The resulting A^* for each isotherm are plotted versus n in Figure 5.5. As n increases in Figure 5.5 so does A^*, which is consistent with each copolymer taking up more space on the interface with each PEG 4-mer added to the branched PEG headgroup. If this trend is assumed to be linear, the area of a PEG 4-mer group on the interface is roughly $\backsim 250$ $\mathring{A}$ before significant interpenetration with neighboring molecules occurs.

As shown in Figure D.2, the approach of approximating the isotherm with a combination of the 2D ideal gas isotherm and the semi-dilute fitted line doesn't fully capture the recorded isotherm. For example, the ideal gas isotherm underestimates the surface pressures observed in the dilute regime and this is consistent across the representative isotherms. Going forward, an alternative, more rigorous method to estimating the crossover from dilute to semi-dilute could be to fit each data regime to their respective scaling and finding the intersection. The reduced surface pressure ($\Pi/\Gamma k_B T$) in the dilute regime is expected to follow Equation 5.1 while the semi-dilute would follow Equation 5.2, where α_1 and α_2 are constants and ν is related to the molecular weight of the polymer M and the radius of gyration in 2D ($R_{g,2D} \backsim M^{\nu}$) [68, 69]. One of the challenges to this approach is that data in the dilute regime is near the sensitivity limit of the Wilhelmy plate and the measurement sometimes drifts between monolayer deposition and compression, making it difficult to reliably interpret Π in the dilute regime and thus fit it to a model. If using this approach, it would be beneficial to collect more data in the dilute regime to get an idea of the average isotherms and error contributed by the Wilhelmy plate.

$$\frac{\Pi}{\Gamma k_B T} = 1 + \alpha_1 \frac{\Gamma}{\Gamma^*} \tag{5.1}$$

$$\frac{\Pi}{\Gamma k_B T} = \alpha_2 (\frac{\Gamma}{\Gamma^*})^{1/(2\nu-1)} \tag{5.2}$$

5.3.3 DMG-PEG4-*n* copolymers at semi-dilute surface concentrations behave like 2D polymers in a good solvent

As each monolayer is compressed beyond the dilute concentrations, the copolymers reach the semi-dilute regime. At semi-dilute concentrations, polymers touch and interpenetrate, forming a mesh-like structure. Assuming good solvent quality, meaning the polymer swells in the presence of solvent, surface pressure follows the 2D equivalent of des Cloizeaux's scaling argument for osmotic pressure in polymer solutions (Equation 5.3) [70, 69]. The exponent ν is taken to be 0.77 for a polymer tethered to the interface in a good solvent, yielding $\Pi/T \backsim \Gamma^{2.85}$ [69, 34, 71]. Figure 5.6 shows $\log \Pi$ versus $\log \Gamma$ for the representative isotherms, where the regime that approximately follows the semi-dilute scaling is outlined by the dashed box. The slopes from linear fits of each dataset in the highlighted regime are reported in Table D.1. The slopes agree moderately well with the expected 2.85, demonstrating that in this regime the DMG-PEG4-n series behaves like polymers tethered to an interface in a good solvent.

$$\Pi/T \backsim \Gamma^{2\nu/(2\nu-1)} \tag{5.3}$$

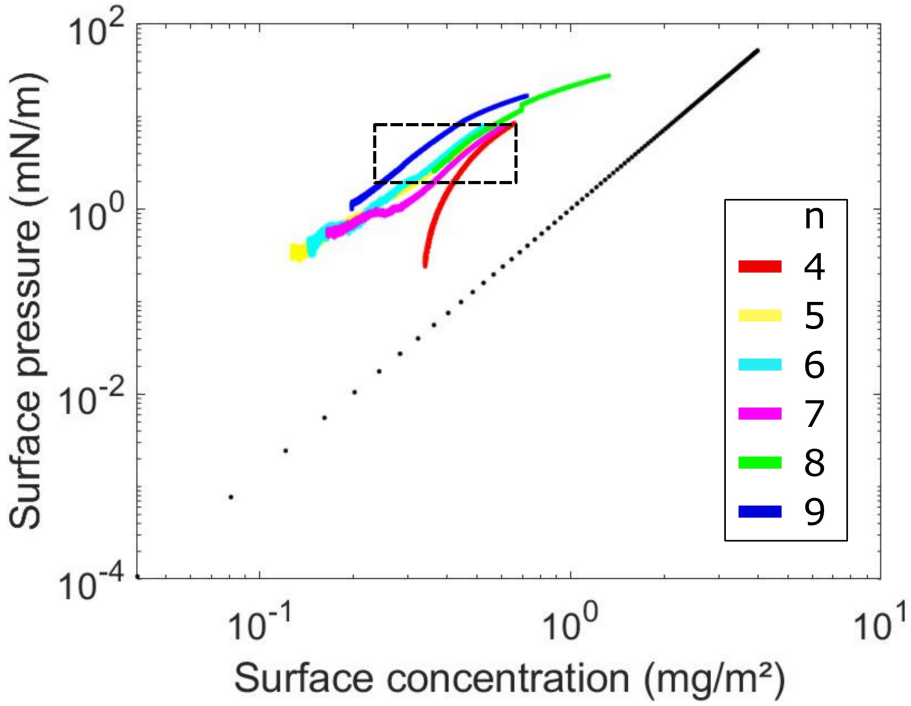

Figure 5.6: Surface pressure versus surface mass concentration plotted for representative isotherms. Dotted black line represents a slope of 2.85, which corresponds to a polymer tetherd to the interface in a good solvent [69, 34, 71] The black dashed box outlines the portions of the isotherms that approximately follow the semi-dilute scaling.

5.3.4 Desorption energies of DMG-PEG4-*n* copolymers grow with *n*

One feature that remains distinct even when the isotherms collapse in Figure 5.4 is the point at which Π plateaus. As mentioned above, PEG homopolymers also exhibit this plateau, which was determined to be due to desorption using a custom deflection tensiometer [36, 66]. A similar approach was employed to study the Π plateau for the DMG-PEG4-*n* series. As shown in Figure 5.7a, a custom SU-8 deflection microtensiometer was first deposited on a clean air-water interface so that Π inside and outside the tensiometer was zero. A sample of DMG-PEG4-9 was deposited to achieve Π = 25 mN/m, which is near the plateau Π and high enough to push the tensiometer arms

into contact (Figure 5.7b). The monolayer was then continually compressed up to and through the plateau region. While compressing in the plateau region, the tensiometer arms began to separate, meaning that the surface pressure inside the tensiometer had increased, indicating that DMG-PEG4-9 had desorbed and then re-adsorbed inside the tensiometer (Figure 5.7c). To further confirm that DMG-PEG4-9 had adsorbed inside, the interface was first expanded to the maximum area, dropping the external $\Pi \approx 25$ mN/m. Figure 5.1d shows the tensiometer arms slightly bowing outward after trough barrier expansion, indicating that there is surface active material (DMG-PEG4-9) trapped inside. Finally, to exaggerate the bowing of the tensiometer arms and confirm that the internal $\Pi > 0$ mN/m, the interface outside of the tensiometer was aspirated to remove

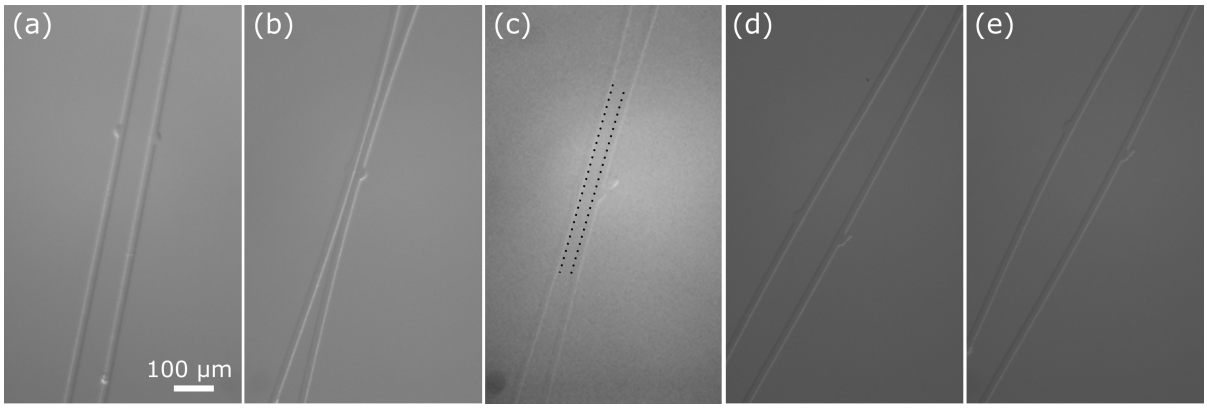

Figure 5.7: Brightfield micrograph series demonstrating desorption in the DMG-PEG4-9 Π plateau by tracking the arms of a custom deflection microtensiometer [66]. (a) Tensiometer on a clean air-water interface. Tensiometer arms are parallel because the Π inside and outside are equal ($\Pi_{in} = \Pi_{out} = 0$ mN/m). (b) Tensiometer arms are pressed into contact after the desposition of DMG-PEG4-9 outside the tensiometer ($\Pi_{out} = 25$ mN/m, $\Pi_{in} = 0$ mN/m). 25 mN/m is near, but below the DMG-PEG4-9 plateau. (c) After compressing into the plateau region, tensiometer arms begin to separate, indicating that $\Pi_{in} > 0$ mN/m. The rise of Π_{in} is the result of desorbed DMG-PEG4-9 re-adsorbing inside the tensiometer. (d) Tensiometer arms bow outward as trough is expanded to maximum area. At the maximum area, $\Pi_{out} \approx 25$ mN/m. Since the tensiometer arms bow outward, $\Pi_{in} > \Pi_{out}$. (e) Tensiometer arms bow even more after aspirating the interface outside the tensiometer, removing the remaining monolayer ($\Pi_{out} = 0$ mN/m). The tensiometer arms bowing outward again verify that DMG-PEG4-9 adsorbed inside the tensiometer ($\Pi_{in} > 0$ mN/m).

the surrounding DMG-PEG4-9 (Figure 5.7e). To summarize, the deflection microtensiometer method demonstrates that the plateaus observed in the DMG-PEG4-n series are a result of DMG-PEG4-n copolymers desorbing from the interface, similar to PEG homopolymers.

n	Π_{des} (mN/m)
4	40.0
5	38.2
6	36.5
7	35.2
8	34.3
9	32.9

Table 5.1: Surface pressure at onset of desorption Π_{des} for representative isotherms of DMG-PEG4-n series. Π_{des} decreases as the the number of PEG 4-mers increases.

The surface pressure at the onset of each plateau Π_{peg} decreases as n increases, as listed in Table 5.1. When each compression isotherm reaches the plateau, the energy at the interface meets the respective desorption energy ΔE_{des} for each DMG-PEG4 oligomer. Following the thermodynamic argument also described by Zell, the onset of each plateau relates directly to ΔE_{des} [36]. The desorption of a single molecule frees an area ΔA, or $1/\Gamma$. The corresponding change free energy is $\Delta E = -\int \Pi dA$, or approximately $-\Pi\Delta A \backsim -\Pi/\Gamma$ for small chain lengths. At the onset of the desorption plateau, the work to desorb a molecule ΔE_{des} is equivalent to the free energy gained by freeing up area for remaining molecules to relax. Thus, $\Delta E_{des} = \Pi_{des}/\Gamma_{des}$, where Π_{des} and Γ_{des} are the Π and Γ at the onset of a plateau. Figure 5.8 shows the ΔE_{des} for each DMG-PEG4 oligomer plotted against n. Similar to PEG homopolymers, ΔE_{des} scales linearly with n, or the amount of PEG. Assuming that $\Delta E_{des} = n\Delta E_{4mer}$, the desorption energy is approximately 2.9 kT per PEG 4-mer or 0.7 kT per PEG monomer, which is comparable in magnitude to the 0.15 kT per PEG monomer reported for linear PEG homopolymers [36]. Notably, the linear relationship between ΔE_{des} and n is not expected to extend to

all $n < 4$, as the size of the aliphatic DMG group becomes comparable to the headgroup. When extending the trend to $n = 0$, $\Delta E_{des} \backsim 0 k_B T$, which does not reflect the expected behavior of an insoluble monolayer of DMG.

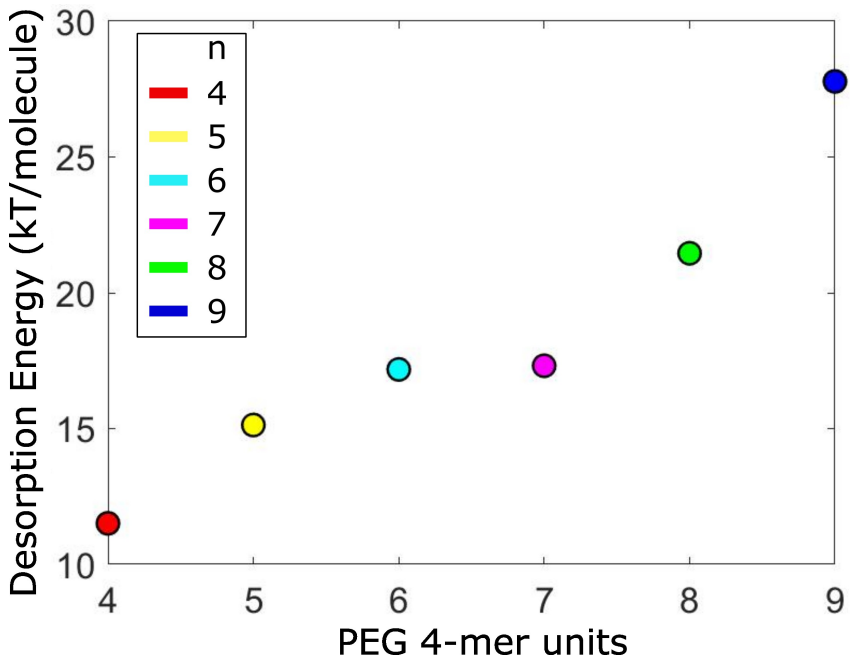

Figure 5.8: Desorption energy ΔE_{des} versus number of PEG 4-mers n. ΔE_{des} is calculated from the respective surface pressure and surface concentration at the onset of the plateau ($\Delta E_{des} = \Pi_{des}/\Gamma_{des}$).

5.4 Conclusions

In summary, we have investigated the interfacial properties across the DMG-PEG4-n library as a function of PEG headgroup size (n). Using a custom Langmuir trough and a Wilhelmy plate tensiometer, we have measured Π-A isotherms of DMG-PEG4-n monolayers on an air-water interface for n ranging from 4 to 9. For the range of n measured, the interfacial behavior is largely dependent on the size of the PEG headgroup. When the isotherms are represented in terms of PEG surface concentration, the library of isotherms collapse onto a single curve, with some departure at higher Π. At dilute

concentrations, DMG-PEG conjugates with larger headgroups occupy more interfacial area. At semi-dilute surface concentrations, where the PEG headgroups contact and interpenetrate, each DMG-PEG conjugate exhibits traits of a 2D polymer in a good solvent. At sufficiently high surface concentrations the energy of each monolayer reaches the respective desorption energy, which grows with the size of the PEG headgroup, and copolymer molecules desorb from the interface. The structure of the PEG headgroups on the DMG-PEG4-n copolymers play a significant role in the resulting interfacial properties. This observation on the importance of PEG headgroup structure would likely extend to the interfacial behavior of other lipid-PEG conjugates. As LNP applications continue to grow and more lipid-PEG conjugates are developed, Π-A isotherms could be a useful tool for characterizing new lipid-PEG conjugate designs.

Chapter 6

Conclusions and future directions

6.1 Outlook on investigation of PLA_2-catalyzed degradation of model LS monolayers

Chapter 3 investigates how monolayer morphology and rheology evolves as DPPC undergoes PLA_2-catalyzed degradation. While degrading, the morphology passes through qualitatively distinct transitions: compactification, aggregation and percolation, coarsening, solidification, network erosion, and PLA_2-rich domain nucleation. Initially, condensed domains shift to more compact shapes, followed by domain aggregation and formation of a percolated network. At the same time, domains coarsen via Ostwald ripening and coalescence up until the solidification transition, when domains no longer visibly flow and relax. After the network is formed and domains have solidified, further degradation leads to erosion of the network and condensation of PLA_2-rich domains. The relative activity of PLA_2, set by the age of the sample, impacts the order and duration of morphology transitions. The fresher the PLA_2, the faster the overall degradation of the condensed phase and the earlier the solidification transition, restricting the coarsening

time. In all cases of PLA_2-activity, $\log|G_s^*|$ grows linearly with the area fraction of the condensed phase ϕ throughout monolayer degradation. Additionally, the relative elasticity of the monolayer increases with the onset of domain solidification, which is hypothesized to be a result of the increasing DPPC-PA co-crystal fraction.

One future direction of this project could be to study this system under more physiologically relevant conditions, such as under expansion-compression cycles and on curved interfaces. The custom Langmuir trough system has planar expansion-compression capabilities, lending itself naturally to studying the morphology and shear rheology of degrading DPPC monolayers under expansion-compression cycles. Using this approach, direct comparisons in morphology and surface shear rheology can be drawn between the constant interface area results in Chapter 3 with dynamic area experiments. A capillary pressure microtensiometer would also be a useful method for studying degrading monolayers, adding the complexity of a curved interface with dilatational rheology capabilities [72, 73, 74]. Employing the microtensiometer technique would enable comparisons between the morphology on a planar versus curved interface as well as probing the monolayer mechanics under dilation, simulating the dilation of alveoli during respiration.

Another direction for this project would be to study mixtures of DPPC with PA and LPC to better understand the roles of each component in the actively degrading system. We hypothesize that the increase in monolayer elasticity and domain solidification in the actively degrading monolayer is due to the increasing fraction of DPPC-PA co-crystals. However, further investigation is needed to determine the PA quantity and distribution within domains required to drive domain solidification and increasing monolayer elasticity. One challenge with testing this hypothesis in situ is the transient concentrations and distributions of DPPC and PA during monolayer degradation, for which there are no direct measurements. A future direction of this investigation could be to measure the monolayer phase behavior, morphology, and rheology of DPPC-PA mixtures, where

the surface concentrations of DPPC and PA are known and controlled. The properties of DPPC-PA mixtures could be compared to the actively degrading monolayers, testing whether or not DPPC-PA mixtures are a model system for the increasing PA fraction in an actively degrading monolayer.

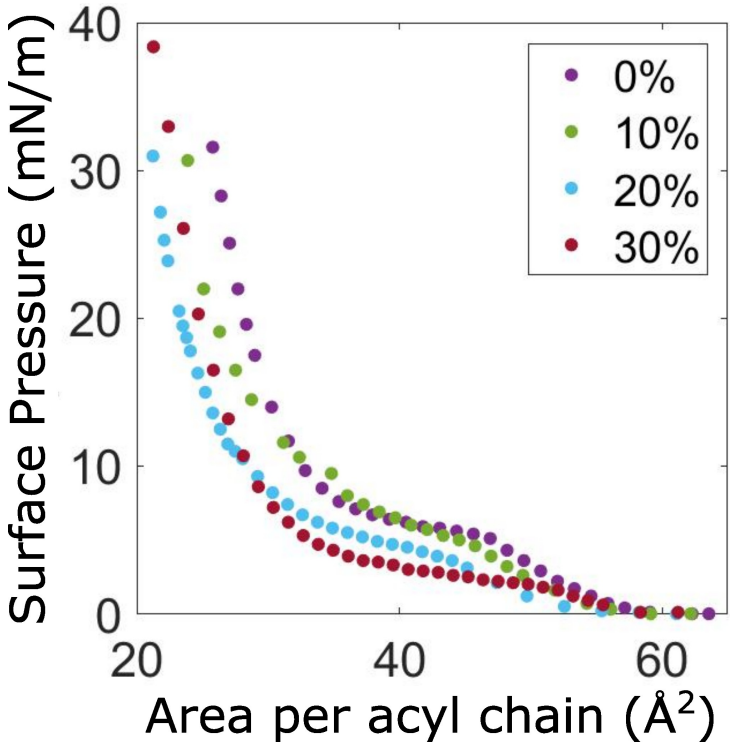

Figure 6.1: Surface pressure–area (Π–A) isotherms of DPPC-PA monolayers on buffered subphase. DPPC-PA mixtures include 0, 10, 20, and 30 mol% PA. Monolayers spread on Ca^{2+}-containing, Tris-buffer (T = 22 °C).

Here, we discuss a few preliminary results of the phase behavior and morphology of DPPC-PA mixtures. The tested PA fractions include 0, 10, 20, and 30 mol% PA, all spread on Ca^{2+}-containing, Tris-buffer at ∽ 22 °C. Figure 6.1, shows a representative Π-A isotherm for each PA fraction. As PA fraction increases, the plateau feature is maintained, but shifts to lower Π. The trend of the coexistence plateau lowering with increasing PA is consistent with reported isotherms collected on air-water interfaces [28, 75]. Samples of the domain morphology near 10 mN/m for each PA fraction is compared in Figure

6.2. As the PA fraction increases, the condensed domains lose the chiral, bean-like shape of pure DPPC (Fig. 6.2a), exhibiting more compact shapes (Fig. 6.2b-d). As previously discussed in Chapter 3, the formation of DPPC-PA co-crystals may be connected to domain compactification observed in the actively degrading system. The compact DPPC-PA domain shapes in Figure 6.2 are also consistent with studies of DPPC-PA monolayers and the analogous fatty alcohol mixture (DPPC-HD) on air-water interfaces in Chapter 4 [31].

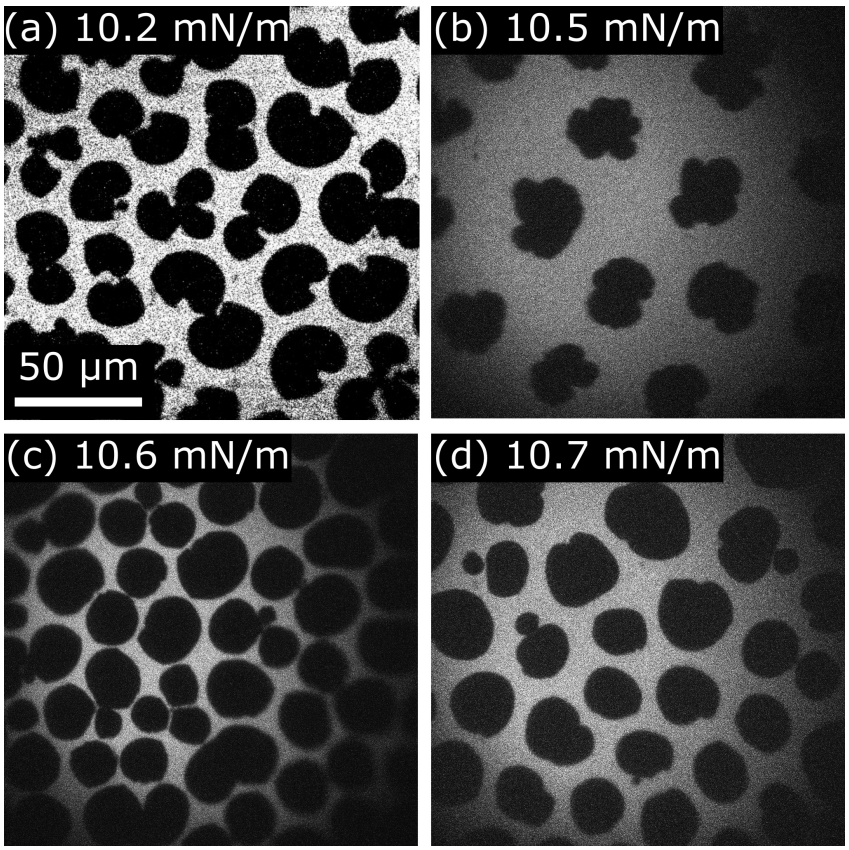

Figure 6.2: Fluorescence micrographs of DPPC (a) and DPPC-PA (b-d) monolayers near $\Pi = 10$ mN/m. (a) Pure DPPC, (b) 10 mol% PA, (c) 20 mol% PA, (d) 30 mol% PA. (a-c) Separate monolayers from those in Fig. 6.1.

More work is needed to determine the relationships between phase behavior, morphology, and rheology of DPPC-PA mixtures. In addition to collecting more isotherms, morphology data, and rheology data over a wider range of DPPC-PA compositions, it

would be worthwhile to compare DPPC-PA mixtures with and without Ca^{2+} ions in the subphase. Ca^{2+} ions are known to bind and even dimerize with fatty acids like PA [55]. Reducing the surface charge density of the condensed phase would influence both structure and dipole density within domains, and likely their interactions. Notably, Vailtierrez-Gaytan et al. reported that PA and HD were interchangeable with respect to the phase behavior and morphology when mixed with DPPC on air-water interfaces [31]. As such, the work of studying DPPC-HD mixtures in Chapter 4 may be reflective of DPPC-PA mixtures on an air-water interface, free of Ca^{2+} ions.

6.2 Outlook on investigation of DPPC:HD + DChol monolayers

Chapter 4 interrogates the relationships between the phase behavior, morphology, and surface rheology of 5:1 DPPC:HD mixtures with 0 and 1.5 mol% DChol. As excess DPPC condenses and the domain area fraction increases, $| G_s^* |$ and relative elasticity grows for each monolayer composition. The addition of DChol shifts the initial growth in $| G_s^* |$ to a higher surface pressure, but $| G_s^* |$ approaches the same magnitude as the 0 mol% DChol monolayer as excess DPPC condenses. Once excess DPPC is condensed $| G_s^* |$ continues to grow for all monolayer compositions with further compression, but not as strongly. $| G_s^* |$ of the DChol-containing monolayer is lower than the DChol-free monolayer once the excess DPPC is condensed, meaning that the DChol-containing monolayer is easier to shear at those surface pressures. As the monolayers approach fully condensed, the relative elasticity of each monolayer decreases with further compression. In this regime, the elastic modulus approaches a constant while the viscous modulus grows. We hypothesize that the elasticity of the condensed monolayers is λ-mediated,

analogous to concentrated 3D emulsions, and becomes constant once the monolayer is fully condensed. The combination of a rise in the surface viscosity from compressing the domains and a λ-mediated elasticity approaching a constant would result in a rise in δ, like the rise measured experimentally.

The future direction of this project would be to measure the phase behavior, morphology, and surface rheology across a wider range of DPPC, HD, and DChol fractions. The ternary mixtures span a wide range of Π-dependent domain area fractions, composition, and shapes; measuring the surface rheology across the composition space will provide insight into how these factors influence the monolayer mechanics. For example, Valtierrez-Gaytan et al. demonstrated that the area fraction of DPPC:HD co-crystals at a given Π decreases as the ratio of DPPC:HD increases [31]. Changes in the condensed phase area fraction would likely affect how $\mid G_s^* \mid$ grows with respect to Π. The addition of DChol lowers domain line tension, which may impact the relative elasticity of monolayers. Lastly, the stripe widths depend on the amount of each component. Conducting measurements across a range of stripe widths will provide insight into the role of domain shape in the surface rheology. In the context of SRT formulas, the composition space could be expanded to include other relevant surfactants, such as PA and LS apoproteins.

6.3 Outlook on investigation of DMG-PEG4-n monolayer library

Chapter 5 investigates the interfacial properties of discrete DMG-PEG4-n copolymers as a function of PEG headgroup size (n ranges 4-9). From the measured Π-A isotherm of each copolymer, we examined the dilute, semi-dilute, and desorption properties, each of which exhibit a dependence on the size of the PEG headgroup. When the isotherms

are represented in terms of PEG surface concentration, the library of isotherms collapse onto a single curve, with some departure at higher Π. To further probe the relationship between isotherms, headgroup structure, and PEG surface concentration, it would be worthwhile to measure the isotherms of other PEG headgroups, especially with a comparable molecular weight of PEG. For example, DMG-PEG8-4 would have the same total amount of PEG as DMG-PEG4-8, but the size and number of PEG branches differ; comparing isotherms of copolymers like DMG-PEG8-4 and DMG-PEG4-8 would provide insight into the significance of headgroup structure versus PEG surface concentration.

Appendix A

Additional experimental protocols

A.1 Cleaning protocols

Maintaining cleanliness is an integral part of this research. This section describes the cleaning protocols applied to all the experiments in this body of work. There are three main categories of cleaning protocols: base/acid cleaning, syringe cleaning and handling, and trough cleaning.

A.1.1 Base and acid cleaning protocols

Glassware is typically cleaned using either a base bath or acid bath protocol. The amber glass vials with teflon-lined caps (Thermo Fisher) for sample storage in Chapters 3 and 5 are cleaned using the base bath protocol. The first step is to immerse vials and caps in a base bath (50 g KOH, 200 mL ultrapure water, 800 mL IPA) for 24 hours. Make sure there are no air bubbles trapped in the vials or caps. Next, vials and caps are rinsed under ultrapure water (Milli-Q), and then immersed in an ultrapure water bath for 24 hours. Throughout cleaning, vials and caps are handled with teflon-coated forceps that have been wiped down with acetone (ACS grade) and isopropyl alcohol (HPLC grade) prior

to handling. The base bath and water bath are conducted in a Pyrex crystallization dish dedicated to vial cleaning. After 24 hours in the water bath, vials and caps are removed, excess water is shaken out, and then they are stored in a repurposed pipette tip box and left to air dry. The storage box is wiped down with acetone and isopropyl alcohol prior to use. Once vials and caps are dry, place caps on vials to prevent accumulation of dust in the vials. After drying, vials and caps are ready for use.

Samples in Chapter 4 are also stored in amber glass vials with Teflon-lined caps. Vials and all other glassware used in the sample preparation process were cleaned by Dr. Valtierrez-Gaytan using the following the acid bath protocol. First glassware is placed in a secondary container (Pyrex dish) and the acid cleaning solution is poured over top (1 packet of NoChromix (Sigma-Aldrich) and 2.5 L pure sulfuric acid (Fisher)). Make sure there are no air bubbles trapped in the vials or caps. Leave glassware to soak at least 8 h. Next, rinse the glassware under ultrapure water 10 times. Allow the glassware to air dry while covered to prevent accumulation of dust.

Caps are cleaned separately by soaking in a detergent solution (3-5 mL Micro-90 per liter ultrapure water). Caps are then transferred to an ultrapure water bath, covered, and shaken. Water bath is poured out and then refilled with more ultrapure water. The shaking, emptying, and refilling process is repeated until there are no visible bubbles after shaking and then the process is repeated three additional times (usually 10 times in total). Caps are then rinsed individually under ultrapure water 10 times each and dried using pressurized nitrogen. Next, sample vials are filled halfway with ultrapure water, capped, and shaken, repeating this sequence 10 times for each vial. Finally, vials and caps are dried under pressurized nitrogen. After drying, vials and caps are ready for use.

A.1.2 Syringe cleaning and handling

Gas-tight syringes (Hamilton) are used for sample preparation and deposition. Prior to use, every syringe is deep-cleaned with chloroform to remove any residues. The cleaning steps include first wiping the syringe tip with a lens wipe soaked in chloroform. Then the syringe is rinsed by filling it with chloroform out of an acid-cleaned vial two hundred times. After the initial cleaning, a syringe is dedicated to a single function, either transferring a single component (e.g. DPPC solution or TR-DHPE solution) or sample deposition. Prior to each use, syringes are cleaned by the following procedure. First an unused scintillation vial is opened and filled with chloroform. The syringe is rinsed with chloroform thirty times from the vial, depositing the used chloroform in a separate waste vial with each rinse. Following every use, the syringe is cleaned again using the same procedure. While handling syringes, it is advised to minimize all contact with the syringe tip to reduce chances of contamination.

To maintain consistent experimental protocols with collaborators, Chapter 4 follows a slightly different syringe cleaning procedure. The initial deep cleaning is the same, but prior to each experiment, the sample deposition syringe is cleaned again using another procedure. The first step in this procedure is to fill two acid-cleaned vials, used only for these experiments, with chloroform. Lastly, the syringe is rinsed with chloroform twenty times from each vial and then it is ready for sample deposition.

A.1.3 Trough cleaning

The interior of the ribbon-barrier Langmuir trough and any items used inside the trough are cleaned before and after conducting experiments. Figure A.1 shows all the components which require cleaning. Before each experiment the ribbon-barrier trough is first cleaned by removing the magnets and magnet holder and then wiping the Teflon

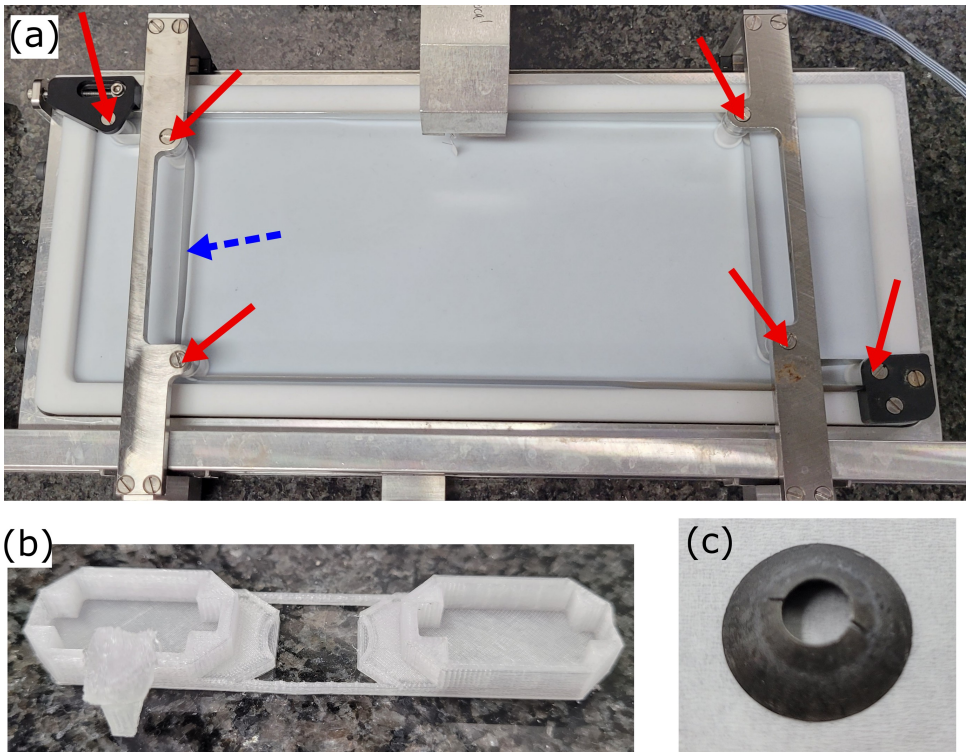

Figure A.1: Images of Langmuir trough and components that require cleaning. (a) Top view of Langmuir trough. Blue dashed arrow points to ribbon barrier. Solid red arrows denote locations of all posts that secure the ribbon barrier. (b) 3D-printed Nylon magnet holder. (c) Top view of cone

interior with a wipe (Kimtech) soaked in HPLC-grade chloroform (Sigma-Aldrich). The ribbon-barrier (Fig. A.1a, dashed arrow), posts that secure the ribbon (Fig. A.1a, red arrows), and cone (Fig. A.1c) are similarly cleaned by wiping with a cotton swab soaked in chloroform. Any remaining droplets of chloroform in the trough are wicked away with a dry wipe.

The next step is a three-stage solvent rinse. The trough and cone are cleaned by alternating rinses of acetone (ACS grade) and ultrapure water (Milli-Q), three times each. This is followed by alternating rinses of isopropyl alcohol (HPLC grade) and ultrapure water, three times each. The trough is then rinsed three more times with ultrapure water. Make sure the cone is completely submerged and no air bubbles trapped inside during

each rinse. The Wilhelmy plates should also come in contact with the liquid for each rinse.

How the holder (Fig. A.1b) is cleaned depends on the holder material. For example, polypropylene holds up to the solvent rinses and is kept in the trough for all rinses. Alternatively, solvents tend to seep into nylon holders, which can cause subphase to leak into the holder later on. Thus, nylon holders are cleaned by wiping with acetone and isopropyl alcohol and then placed in the trough for the final rounds of water rinses. Magnets are deposited in the holder prior to the final water rinse so that any debris that falls into the trough is rinsed out.

In Chapter 4, two additional steps are added during the final water rinse. First, the barrier is compressed to the smallest area without touching the magnet holder, and then the interface inside the ribbon is aspirated for a few seconds. Second, the barrier is then expanded to the maximum area and the interface outside the ribbon is aspirated for a few seconds. After the third water rinse, the remaining water is aspirated from the trough and the aqueous subphase is deposited.

Regardless of cleaning procedure, after an experiment is concluded, the monolayer and subphase are removed by aspirating at the air-subphase interface. All the cleaning steps are repeated and finally, the trough is left filled with enough ultrapure water to submerge the cone. Keep the trough covered and maintain the water level between experiments.

A.2 Stock solutions and handling procedures for DPPC sample preparation

All DPPC monolayers from Chapter 3 are prepared from stock solutions of DPPC in chloroform (Avanti Polar Lipids Ltd) and TR-DHPE chloroform. The stock solution of

DPPC arrives in glass ampoules. Before use, the DPPC stock is poured directly into a base-cleaned sample vial and capped. The Texas Red labelled DHPE (Life Technologies) arrives dried in a plastic vial that is incompatible with chloroform. A stock of TR-DHPE solution is prepared by first filling a base-cleaned sample vial with chloroform. Then a stainless steel spatula is wiped down with acetone (ACS grade) and air-dried. Use the clean spatula to scrape the TR-DHPE from the plastic vial and transfer to the chloroform-filled sample vial.

When transferring solutions into the storage vials, it is best to keep the vials closed as much as possible and to minimize contact with the vial and cap interiors, thereby minimizing evaporation and contamination. After capping any vial, the outside gap between the cap and vial is wrapped in Teflon thread sealant tape as an additional protective seal. The tape must be wrapped clockwise around the vial so that the cap is not loosened. All stock solutions and samples are stored in a freezer (-20 °C) when not in use. When removing from the freezer, allow to come up to room temperature and wipe off condensation before removing Teflon tape and cap.

A.3 Preparing Wilhelmy plates

Filter paper (grade 541, Whatman) is cut into 3 mm by $\backsim$ 1 cm strips. Next, two glass petri dishes are cleaned using a three-stage solvent rinse. The first stage is alternating rinses of acetone (ACS grade) and ultrapure water (Milli-Q), three times each. The second stage is alternating rinses of isopropyl alcohol (HPLC grade) and ultrapure water, three times each. The final stage is three rinses with ultrapure water. Finally, one dish is filled with HPLC-grade chloroform and the other is left empty. The Teflon-lined forceps used to handle the cut filter paper is first cleaned by wiping down with acetone and isopropyl alcohol. Using the cleaned forceps, each filter paper strip is submerged in the chloroform

and then laid in the empty dish to air dry. Once dry, the petri dish is covered and stored to prevent the accumulation of dust. When mounting a filter paper strip, handle with cleaned forceps. Using the tip of the forceps, puncture a hole into one end of the paper. Bend a $\backsim$ 1 inch piece of stainless steel wire into an approximate 's' shape. Using the forceps, thread the wire through the hole in the paper. The Wilhelmy plate is now ready to be mounted onto the tensiometer.

A.4 Magnet holder design and handling

The electromagnetic coils are secured by a custom 3D printed holder. One purpose the magnet holders serve is to hold the coils in a fixed position, so that the magnetic field is kept consistent across experiments. The other function is to separate the coils from the monolayer and subphase. Previous iterations of magnet holders have been built directly into troughs [41] or out of aluminum [38]. The advantage of 3D printing the holder is the ease of customization. A schematic of the design made for the experiments in this body of work is shown in Figure A.2. Overall, the design is optimized to minimize the interfacial area it takes up. For example, the slots for the coils (Fig. A.2, solid arrows) and the syringe tip holder (Fig. A.2, dashed arrows) are the only parts that protrude out of the subphase during experiments. Keeping those features small leaves more accessible interfacial area for the monolayers. The bottom platform (Fig. A.2, solid lines) lifts the cone off the bottom of the trough, allowing molecules in the subphase (e.g. PLA_2) to enter the cone from below in addition to the slits along the top of the cone. The second tier (Fig. A.2, dashed lines) holds the cone in place to keep the magnetic field consistent across experiments. The purpose of the syringe tip holder (Fig. A.2, dashed arrows) is to keep the injection site in the subphase (e.g. PLA_2 solution) at a constant location and prevent errors that can arise if injecting by hand. The distance between the slots for the

coils was chosen to hold the coils as close together as possible, while leaving room for the objective.

Because 3D printed magnet holders are easy to customize, the magnet configuration is not limited to one experimental setup. For example, holders can be designed to fit different trough geometries. However, if the distance between the coils or the relative height of the cone changes, additional measurements are needed to determine the new ratio of the magnetic field to the current (B/I). First, set up the coils and cone in the magnet holder. Secure the gauss meter wand (5180 Gauss meter, F.W. Bell) to a ring stand using a clamp. Check the gauss meter manual to make sure the gauss meter wand is oriented in the proper direction to measure the magnetic field between the coils. Lower the clamp so that the gauss meter wand is just inside the cone, where a microbutton would sit during an experiment. Turn on a constant magnetic field for a range of applied voltages (0-1 V in increments of 0.1 V). Record the reading on the gauss meter for each voltage. Repeat four more times, raising and lowering the gauss meter wand between each series of measurements. Average the B values for each voltage. Measure the resistance across the coils, then convert voltage to current. Apply a linear fit to B versus I and take the slope as the new B/I. Finally, enter B/I into the rheology GUI.

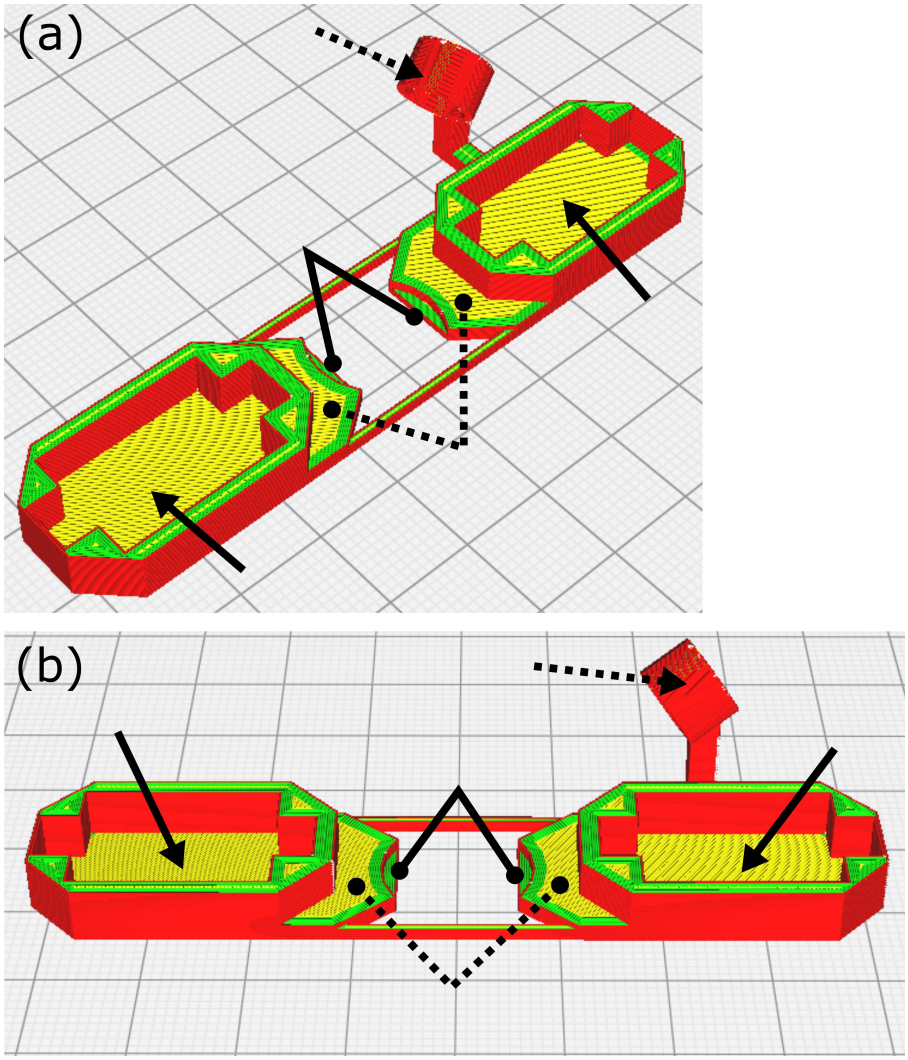

Figure A.2: Schematic of 3D-printed magnet holder design from different angles. Walls of slots for electromagnetic coils (solid arrows) and syringe tip holder (dashed arrows) protrude out of subphase in experiments. Slots keep coils dry and placement consistent across experiments. The syringe tip holder enables hands-free injection of PLA_2-solution at the same site across all experiments. Cone sits on bottom platform (solid lines), lifted off the trough to enable PLA_2 in the subphase to enter the cone from below. Cone is held in place by the walls of the second tier (dashed lines), so that cone placement is consistent across experiments.

A.5 Microbutton handling and setup

When not in use, microbutton probes are stored in ultrapure water (Milli-Q) in a glass vial. The vial rests on top of a rare earth magnet to keep the probes magnetized. Prior to depositing a microbutton, the subphase has to be sufficiently low so that the probe doesn't flow out of the cone. The appropriate subphase level is determined through trial and error by depositing a probe and watching to see if it remains in the cone. The appropriate subphase level depends on the specific cone used and its height from the bottom of the trough. If the cone and height are consistent, a notch could be made on the magnet holder to visually indicate when the subphase level is correct. To deposit a microbutton, it is first picked up by touching the needle tip of a syringe (tuberculin syringe, 27 gauge needle, BD) to a floating probe in the storage vial. This process is difficult to do by eye and is made easier by looking at the storage vial under magnification and additional light. The probe is deposited on the interface by tapping the loaded needle tip to the air-subphase interface inside the cone. Successful deposition can be initially verified by eye; setting the brightfield light source to the maximum intensity makes it easier to see the microbutton. Successful deposition is officially confirmed by finding the probe using the microscope eyepieces. Confirm that the object is a single microbutton. If attempts to deposit a microbutton are unsuccessful, aspirate the interface in-between attempts; any debris or microbuttons out of the field of view can ruin experiments.

After a probe is deposited, the next step is to check the angle of the magnetic moment relative to the applied magnetic field. The angle will limit the maximum torque that can be applied, so it is ideal to get it as close to 90° as possible. The angle can be checked by applying a constant magnetic field and watching the probe rotation. To adjust the microbutton angle, use Teflon-coated forceps to nudge the outside of the cone, pushing it to rotate. When finished making adjustments, record an image of the probe when the

constant field is on and when it is turned off. The rheology GUI assumes the magnetic moment of the probe is 90° from the direction of the magnetic field. The images are used to correct the final rheology data, accounting for the actual angle of the magnetic moment.

Appendix B

Supplementary materials for Chapter 3

B.1 Supplementary figures

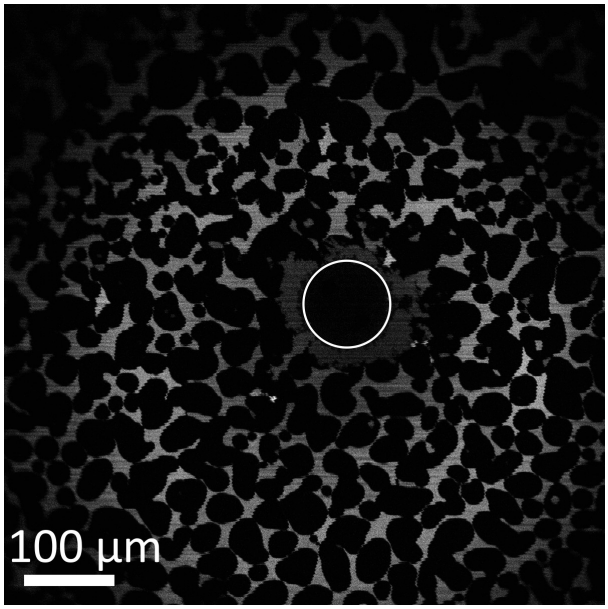

Figure B.1: Larger field of view fluorescence micrograph of Fig. 3.4d, showing the 2D colloidal gel-like network spanning the interface. Note that in this experiment, degradation detached disk from network. In such cases, rheology after detachment is not reported; only morphology is tracked.

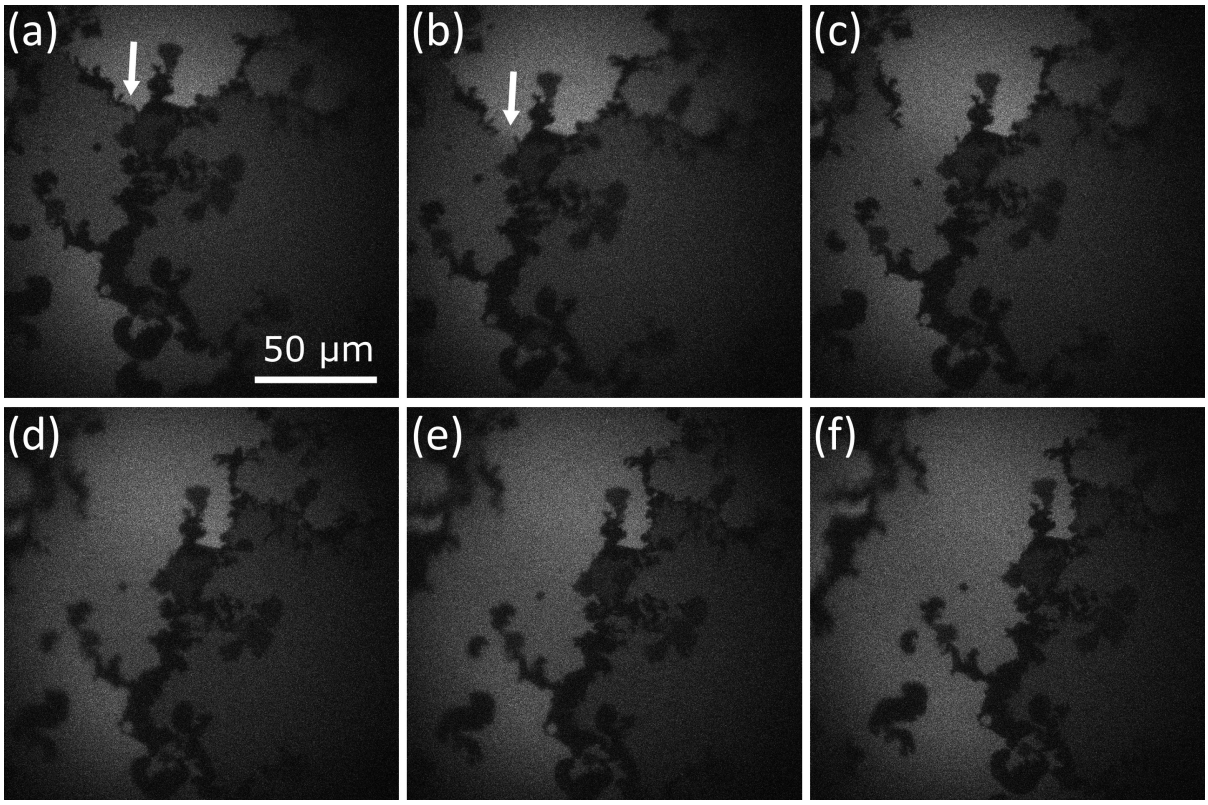

Figure B.2: Fluorescence micrographs tracking network breakage event and corresponding mixing of formerly distinct pockets of disordered phase. (a) White arrow indicates network bridge prior to breakage. Disordered phase above and below have differing fluorescence intensities, indicating distinct pockets separated by the network. (b) White arrow points at breakage location. Front of higher fluorescence intensity is visibly passing through the breakage area, showing the initial diffusive mixing of the two disordered regions. (c-e) Fluorescence intensities continue to equilibrate, reaching a fully mixed, uniform intensity in (f).

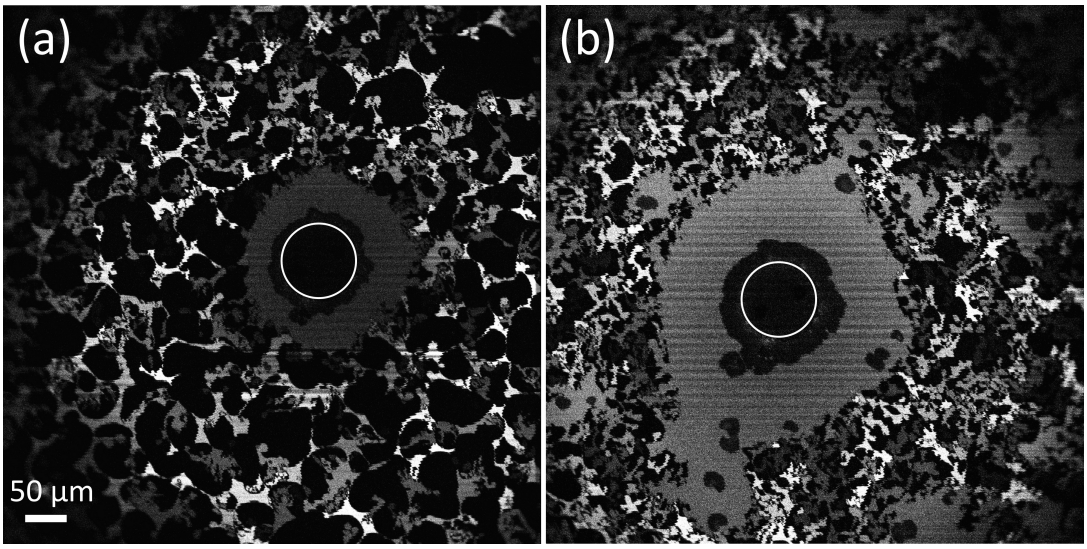

Figure B.3: Larger field of view fluorescence micrographs of (a) Fig. 3.4e and (b) Fig. 3.4f from the main text. Micrographs show on a larger scale the impact of network erosion. Like in Figure S1, rheology data is not taken for detached probes. Condensed domains lining each probe are understood to be of the same makeup as the new domains that nucleate at late stages of degradation, like the domain discussed in Fig. 3.6 in the main text.

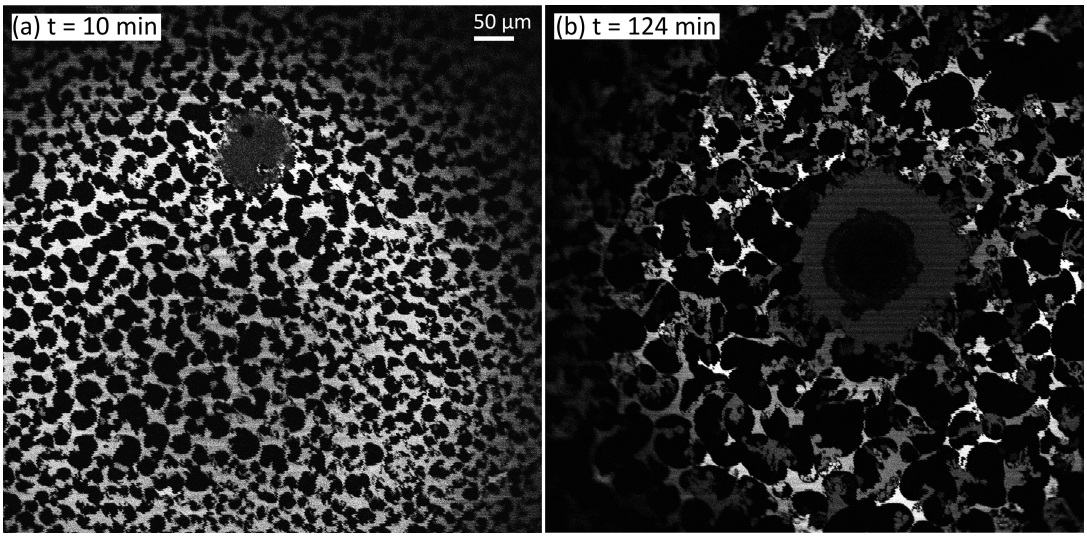

Figure B.4: Larger field of view fluorescence micrographs of (a) Fig. 3.7c and (b) Fig. 3.7c inset. Micrographs show on a larger scale the initial solid-like network when using relatively fresh (a) or old (b) PLA_2. For the monolayer in (b), the probe was connected until t $\backsim$ 100 minutes; rheology data prior to probe detaching is reported in Fig. 3.9.

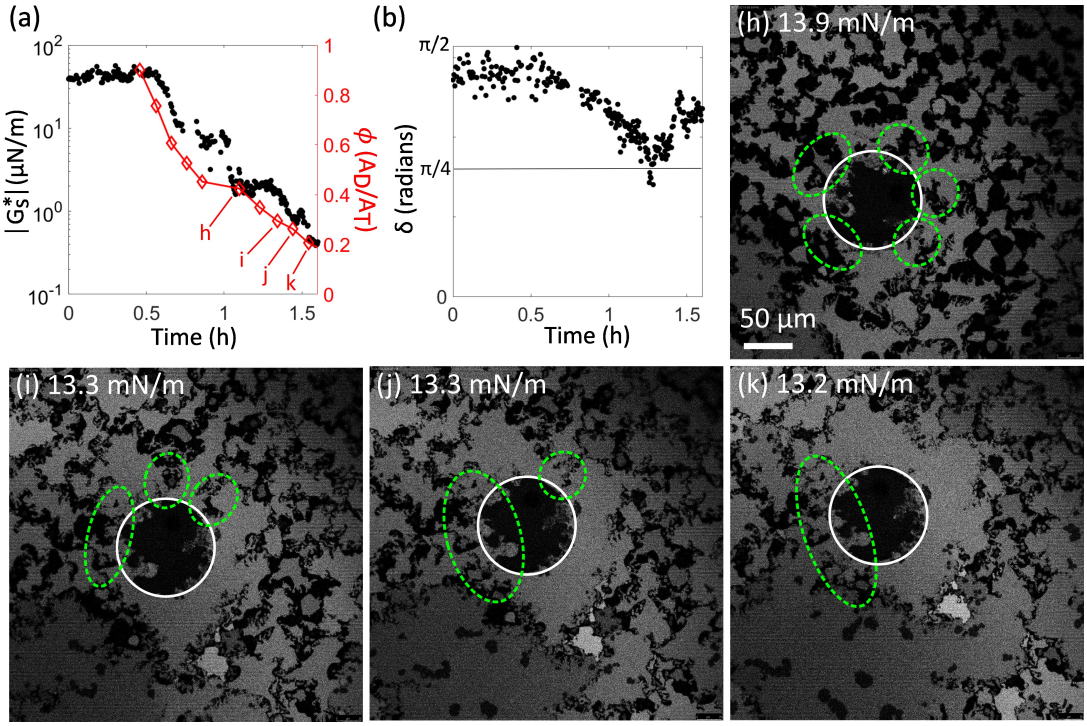

Figure B.5: (a) and (b) reproduce Fig. 3.8 in the main text. The fluorescence micrographs (h-k) correspond to the (h-k) labels in the interfacial rheology data. Micrographs show the points of contact between the condensed phase and the microbutton probe, outlined in green dashes, transitioning from five points initially distributed around the probe (h), to three points (i), then two points (j), finally one point (k).

B.2 Surface behavior of PA and LPC

Palmitic acid, like DPPC, has well established phase behavior on air-water interfaces [28, 75, 76]. PA is insoluble in the subphase, like DPPC, so its phase behavior can be described with Π-A isotherms. At very low surface concentrations, $\Pi \simeq 0$ mN/m, PA is in the gas phase. At $\Pi \leq 24$ mN/m, PA is in a tilted condensed phase and for $\Pi > 24$ mN/m, PA is in an untilted solid phase (T $\backsim$ 21 °C) [76].

Surface rheology measurements have reported for PA on air-water interfaces [77, 76]. A previous study using the microbutton microrheometry technique [76], reported that the surface shear modulus at 1 Hz is primarily viscous in the tilted condensed phase ($0 < \Pi < 24$ mN/m). $\mid G_s'' \mid$ grows exponentially with Π, rising from approximately 10^{-5} mPa·m to 10^{-3} mPa·m in the tilted condensed phase. At the onset of the untilted solid phase, $\mid G_s' \mid$ appears discontinuously. Above the untilted solid phase transition ($\Pi > 24$ mN/m), the shear moduli grow and the response is elastic-dominated until monolayer collapse.

LPC is soluble in the aqueous subphase and does not pack to form 2D ordered phases at the surface like DPPC and PA. For a given concentration of LPC in the subphase there is a corresponding equilibrium surface pressure, Π_e; if the interface is compressed or expanded, LPC desorbs or adsorbs, respectively, to maintain Π_e. The adsorption isotherms of LPC in DI water and phosphate buffered saline plotted in Figure B.6 shows the Π_e as function of the subphase concentration. At the CMC (C $\approx 10^{-5}$ M) and higher concentrations, the surface pressure remains constant as LPC micellizes in the subphase. Like other soluble surfactants, LPC is expected to have no measurable surface shear viscosity [78]. Although an isotherm on Ca^{2+}-containing, Tris-buffer has not been recorded, it is reasonable to expect that the isotherm will be similar to the isotherms on DI water and PBS.

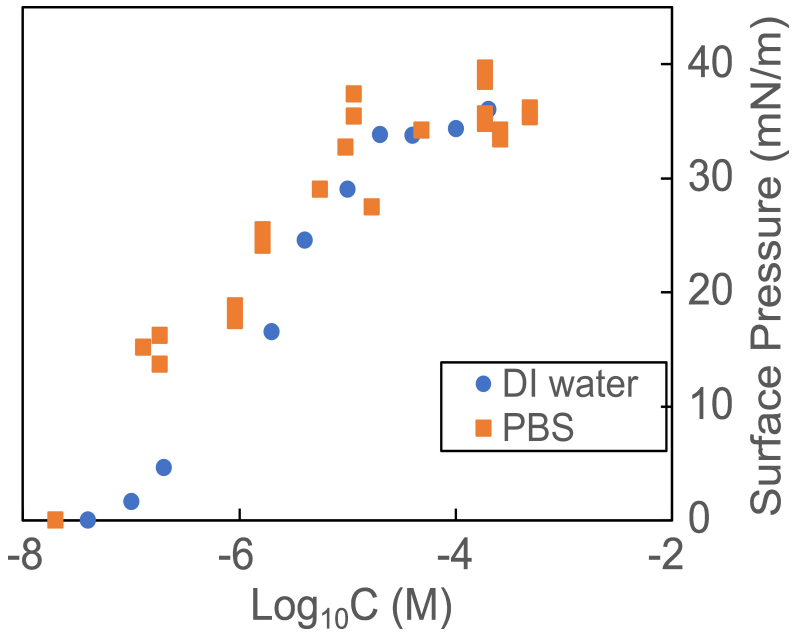

Figure B.6: Adsorption isotherms of LPC in DI water (blue circle) and PBS (orange square) at T ∽ 21°C.

Appendix C

Supplementary materials for Chapter 4

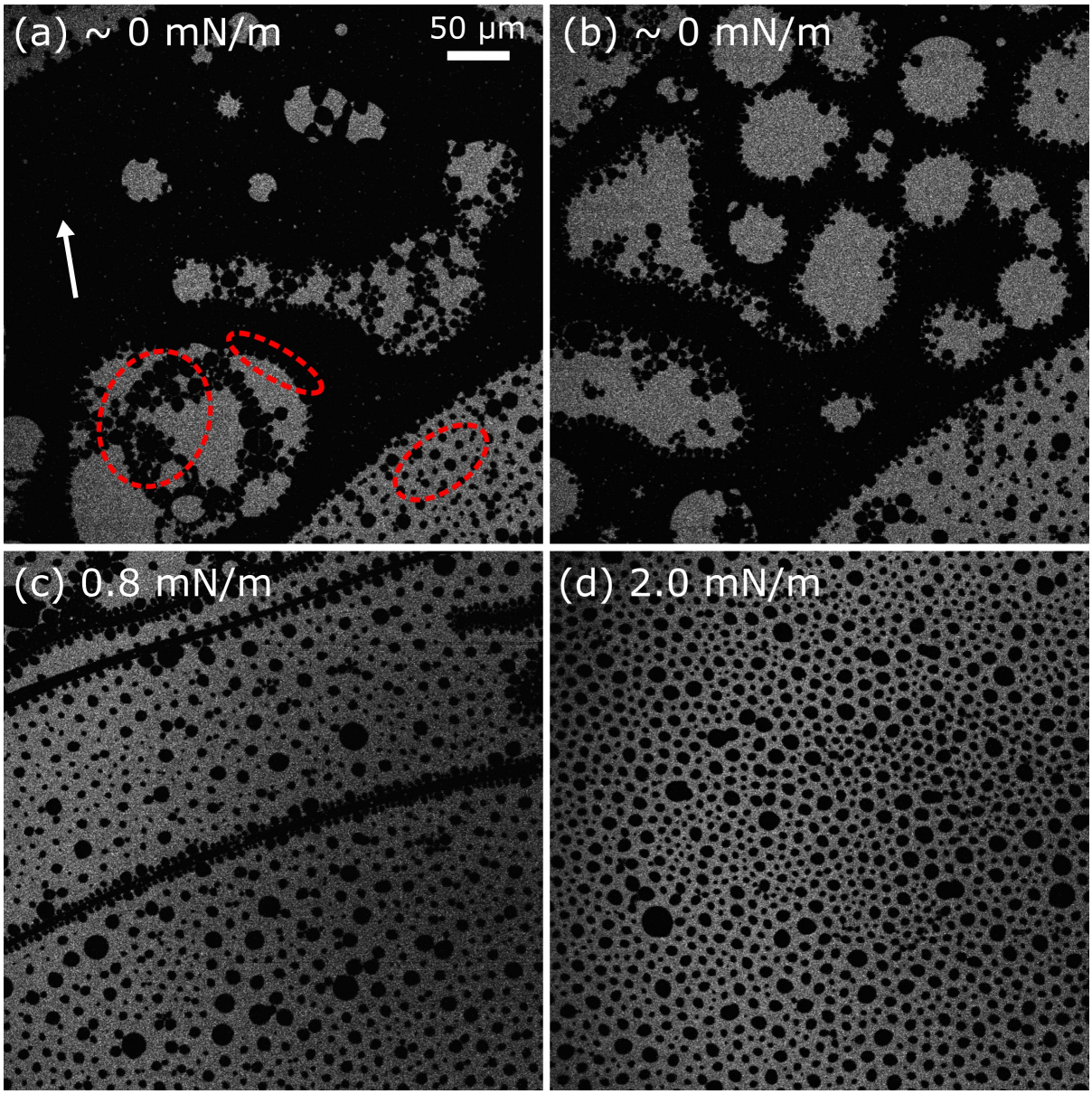

Figure C.1: Fluorescence micrographs of 5:1 DPPC:HD at low Π. (a) Excess DPPC coexists as LE (bright phase) and gaseous (black phase, white arrow). 2:1 DPPC:HD co-crystals form at Π ≈ 0 mN/m (outlined in red dashes). Co-crystals are both dispersed in the LE phase and lining the gaseous DPPC phase boundaries. (b-d) As monolayer is compressed, gaseous DPPC shifts to LE DPPC until excess DPPC is fully LE.

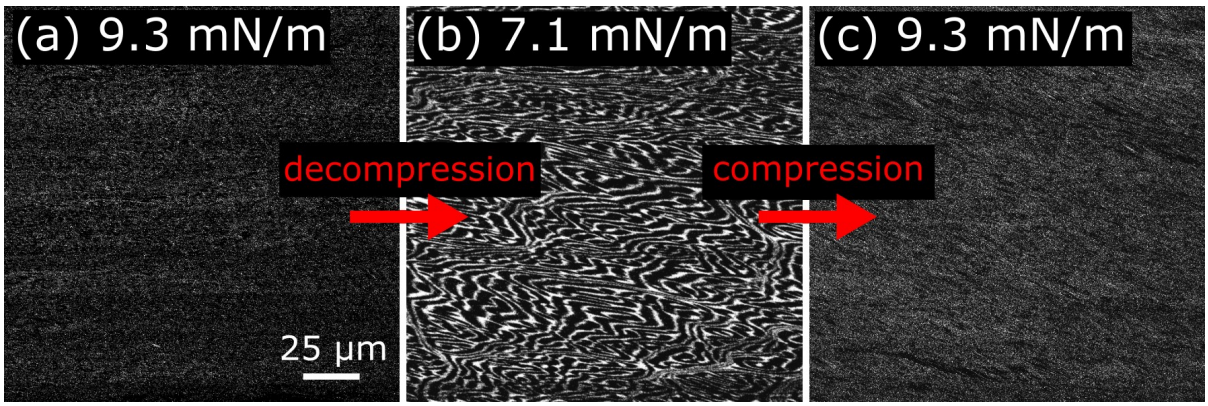

Figure C.2: Decompression/compression cycle demonstrating recovery of stripe widths in 5:1 DPPC:HD + 1.5 mol% monolayers. (a) Stripe widths begin below the limit of resolution. (b) Monolayer decompressed to Π where stripe widths are visible. Stripe domains are distorted in image because barriers are in motion during image acquisition. Decompression step was ≈7 minutes. (c) Monolayer is compressed back to the initial Π where stripe widths are again below the limit of resolution. Compression step was ≈7 minutes.

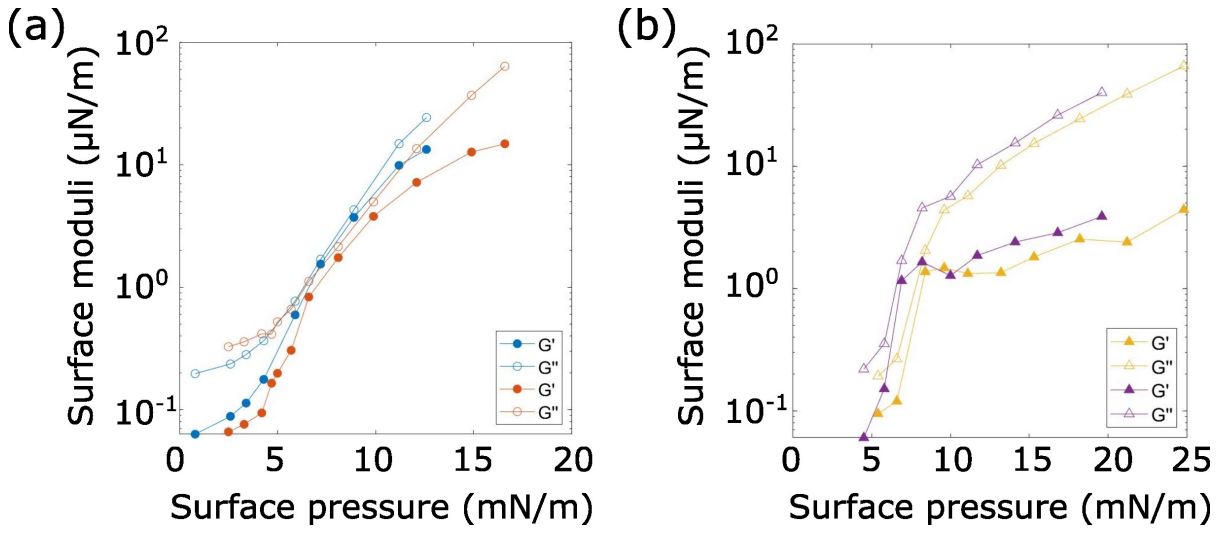

Figure C.3: Surface shear moduli | G' | and | G'' | for 5:1 r-DPPC:HD monolayers (a) and 5:1 rac-DPPC:HD + 1.5 mol% DChol monolayers (b). Monolayers correspond to same monolayers as in Figure 4.4.

Appendix D

Supplementary materials for Chapter 5

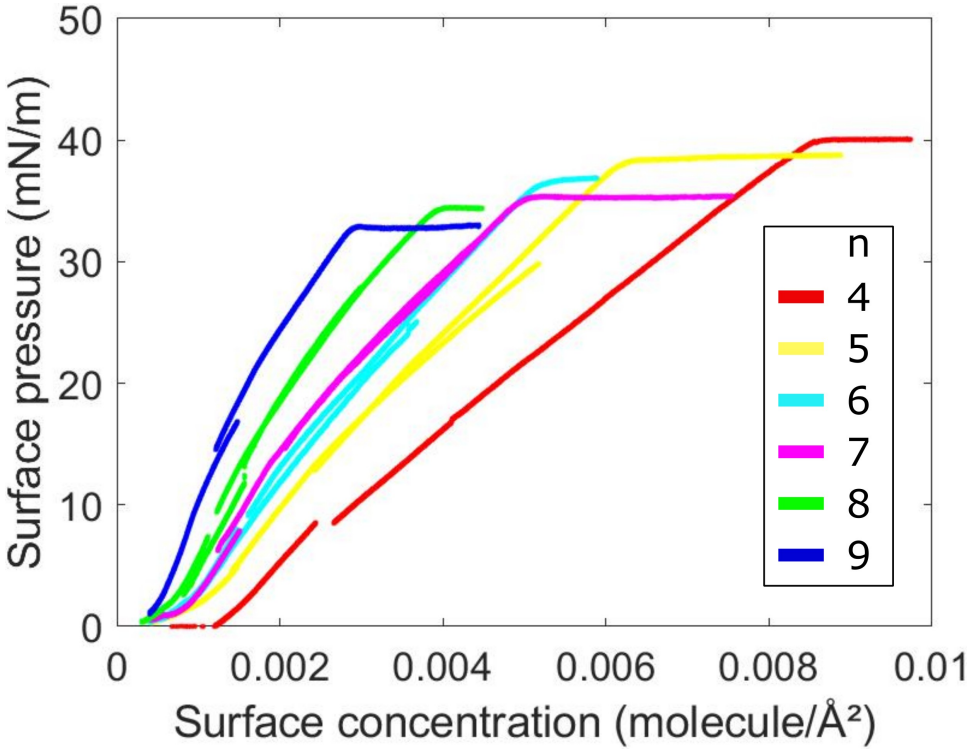

Figure D.1: Representative Π-Γ isotherms of DMG-PEG4-n library on an air-water interface (T ≈ 21 °C).

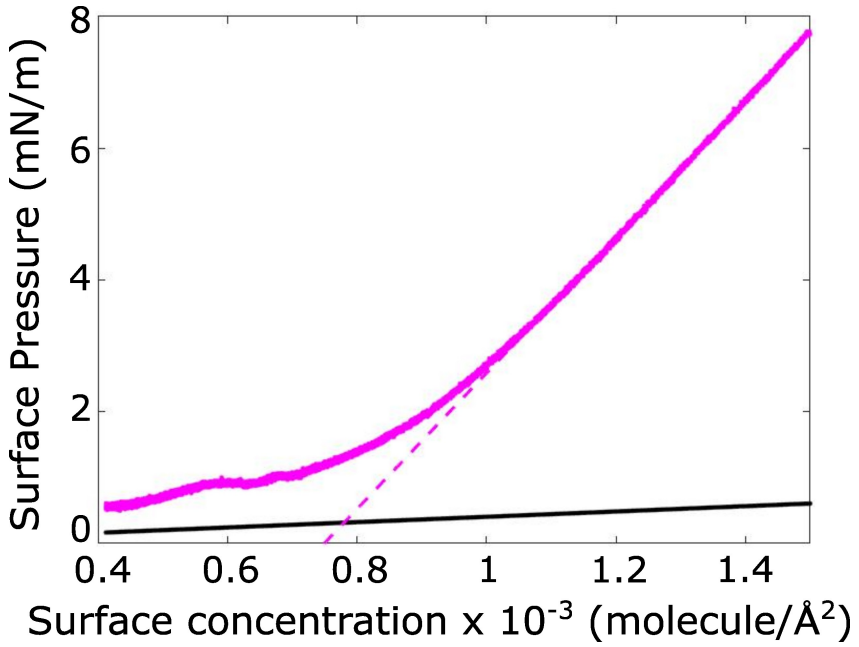

Figure D.2: Demonstration of overlap concentration approximation on Π-Γ plot. Black solid line represents the 2D ideal gas isotherm. Magenta curve denotes the recorded isotherm ($n = 7$) and the dashed line corresponds to the semi-dilute fitted line.

n	slope
4	2.92
5	2.47
6	2.63
7	2.76
8	2.63
9	2.62

Table D.1: Slopes from linear fits of DMG-PEG4-n isotherms in Figure 5.6. Slopes are determined for data within the range of $\Pi = 2 - 8$ mN/m. Π range was limited by the ranges over which individual isotherms were collected.

Bibliography

[1] C. C. Chang, A. Nowbahar, V. Mansard, I. Williams, J. Mecca, A. K. Schmitt, T. H. Kalantar, T. C. Kuo, and T. M. Squires, *Interfacial rheology and heterogeneity of aging asphaltene layers at the water-oil interface*, *Langmuir* **34** (2018) 5409–5415.

[2] R. H. Notter, *Lung surfactants: basic science and clinical applications*. CRC Press, 2000.

[3] M. A. Matthay, R. L. Zemans, G. A. Zimmerman, Y. M. Arabi, J. R. Beitler, A. Mercat, M. Herridge, A. G. Randolph, and C. S. Calfee, *Acute respiratory distress syndrome*, *Nature Reviews Disease Primers* **5** (2019) 1–22.

[4] B. T. Thompson, R. C. Chambers, and K. D. Liu, *Acute respiratory distress syndrome*, *New England Journal of Medicine* **377** (2017) 562–572.

[5] R. Tenchov, R. Bird, A. E. Curtze, and Q. Zhou, *Lipid nanoparticles from liposomes to mrna vaccine delivery, a landscape of research diversity and advancement*, *ACS Nano* **15** (2021) 16982–17015.

[6] X. Hou, T. Zaks, R. Langer, and Y. Dong, *Lipid nanoparticles for mrna delivery*, *Nature Reviews Materials* **6** (2021) 1078–1094.

[7] C. B. Daniels and S. Orgeig, *Pulmonary surfactant: the key to the evolution of air breathing*, *Physiology* **18** (2003), no. 4 151–157.

[8] E. Parra and J. Pérez-Gil, *Composition, structure and mechanical properties define performance of pulmonary surfactant membranes and films*, *Chemistry and Physics of Lipids* **185** (2015) 153–175.

[9] J. A. Clements and M. E. Avery, *Lung surfactant and neonatal respiratory distress syndrome*, *Am J Respir Crit Care Med* **157** (1998) 59–66.

[10] S. J. Tzotzos, B. Fischer, H. Fischer, and M. Zeitlinger, *Incidence of ards and outcomes in hospitalized patients with covid-19: A global literature survey*, *Critical Care* **24** (2020) 1–4.

[11] Y. Y. Zuo, R. A. Veldhuizen, A. W. Neumann, N. O. Petersen, and F. Possmayer, *Current perspectives in pulmonary surfactant - inhibition, enhancement and evaluation*, *Biochimica et Biophysica Acta - Biomembranes* **1778** (2008) 1947–1977.

[12] K. W. Lu, H. W. Taeusch, B. Robertson, J. Goerke, and J. A. Clements, *Polyethylene glycol/surfactant mixtures improve lung function after hcl and endotoxin lung injuries*, *American Journal of Respiratory and Critical Care Medicine* **164** (2001) 1531–1536.

[13] K. W. Lu, H. W. Taeusch, B. Robertson, J. Goerke, and J. A. Clements, *Polymer-surfactant treatment of meconium-induced acute lung injury*, *American Journal of Respiratory and Critical Care Medicine* **162** (2013) 623–628.

[14] J. A. Zasadzinski, T. F. Alig, C. Alonso, J. B. D. L. Serna, J. Perez-Gil, and H. W. Taeusch, *Inhibition of pulmonary surfactant adsorption by serum and the mechanisms of reversal by hydrophilic polymers: Theory*, *Biophysical Journal* **89** (2005) 1621–1629.

[15] D. F. Wilson, N. J. Thomas, B. P. Markovitz, L. A. Bauman, J. V. DiCarlo, S. Pon, B. R. Jacobs, L. S. Jefferson, M. R. Conaway, and E. A. Egan, *Effect of exogenous surfactant (calfactant) in pediatric acute lung injury*, *Journal of the American Medical Association* **293** (2005) 470–476.

[16] D. F. Willson, P. R. Chess, and R. H. Notter, *Surfactant for pediatric acute lung injury*, *Pediatric Clinics of North America* **55** (2008) 545–575.

[17] P. Bruins, J.-J. Rouby, B. Lachmann, L. Holzapfel, T. E. Stewart, J. Kesecioglu, G. P. Findlay, R. Beale, E. J. Steenken, and O. K. Jeppesen, *Exogenous natural surfactant for treatment of acute lung injury and the acute respiratory distress syndrome*, *American Journal of Respiratory and Critical Care Medicine* **180** (2009) 989–994.

[18] R. C. McIntyre, E. J. Pulido, D. D. Bensard, B. D. Shames, and E. Abraham, *Thirty years of clinical trials in acute respiratory distress syndrome*, *Critical Care Medicine* **28** (2000) 3314–3331.

[19] A. Anzueto, A. Jubran, J. A. Ohar, C. A. Piquette, S. I. Rennard, G. Colice, E. N. Pattishall, J. Barrett, M. Engle, K. A. Perret, and B. K. Rubin, *Effects of aerosolized surfactant in patients with stable chronic bronchitis: A prospective randomized controlled trial*, *JAMA* **278** (11, 1997) 1426–1431.

[20] D. Machado-Aranda, Z. Wang, B. Yu, M. V. Suresh, R. H. Notter, and K. Raghavendran, *Increased phospholipase a2 and lyso-phosphatidylcholine levels are associated with surfactant dysfunction in lung contusion injury in mice*, *Surgery* **153** (2013) 25–35.

[21] G. Nakos, E. I. Kitsiouli, I. Tsangaris, and M. E. Lekka, *Bronchoalveolar lavage fluid characteristics of early intermediate and late phases of ards. alterations in leukocytes, proteins, paf and surfactant components*, *Intensive Care Medicine* **24** (1998) 296–303.

[22] A. Gunther, C. Siebert, R. Schmidt, S. Ziegler, F. Grimminger, M. Yabut, B. Temmesfeld, D. Walmrath, H. Morr, and W. Seeger, *Surfactant alterations in severe pneumonia, acute respiratory distress syndrome, and cardiogenic lung edema*, *American Journal of Respiratory and Critical Care Medicine* **153** (1996) 176–184.

[23] B. P. Hurley and B. A. McCormick, *Multiple roles of phospholipase a2 during lung infection and inflammation*, *Infection and Immunity* **76** (2008) 2259–2272.

[24] B. A. Holm, L. Keicher, M. Liu, J. Sokolowski, and G. Enhorning, *Inhibition of pulmonary surfactant function by phospholipases*, *Journal of Applied Physiology* **71** (1991) 317–321.

[25] R. D. Hite, M. C. Seeds, R. B. Jacinto, B. L. Grier, B. M. Waite, and D. A. Bass, *Lysophospholipid and fatty acid inhibition of pulmonary surfactant: Non-enzymatic models of phospholipase a2surfactant hydrolysis*, *Biochimica et Biophysica Acta - Biomembranes* **1720** (2005) 14–21.

[26] B. A. Holm, Z. Wang, and R. H. Notter, *Multiple mechanisms of lung surfactant inhibition*, *Pediatric Research* (1999).

[27] C. W. McConlogue and T. K. Vanderlick, *Monolayers with one component of variable solubility: Studies of lysophosphocholine/dppc mixtures*, *Langmuir* **14** (1998) 6556–6562.

[28] K. Y. C. Lee, A. Gopal, A. von Nahmen, J. A. Zasadzinski, J. Majewski, G. S. Smith, P. B. Howes, and K. Kjaer, *Influence of palmitic acid and hexadecanol on the phase transition temperature and molecular packing of dipalmitoylphosphatidyl-choline monolayers at the air–water interface*, *The Journal of Chemical Physics* **116** (2002) 774–783.

[29] J. Ding, H. E. Warriner, and J. A. Zasadzinski, *Viscosity of two-dimensional suspensions*, *Physical Review Letters* **88** (2002) 168102.

[30] J. M. Barakat and T. M. Squires, *Curvature-mediated forces on elastic inclusions in fluid interfaces*, *Langmuir* **38** (2022), no. 3 1099–1105.

[31] C. Valtierrez-gaytan, J. M. Barakat, M. Kohler, K. Kieu, B. L. Stottrup, and J. A. Zasadzinski, *Spontaneous evolution of equilibrium morphology in phospholipid-cholesterol monolayers*, *Science Advances* **8** (2022) 1–12.

[32] J. Chen, A. Rizvi, J. P. Patterson, and C. J. Hawker, *Discrete libraries of amphiphilic poly(ethylene glycol) graft copolymers: Synthesis, assembly, and bioactivity*, *Journal of the American Chemical Society* **144** (2022) 19466–19474.

[33] J. Majewski, T. L. Kuhl, M. C. Gerstenberg, J. N. Israelachvili, and G. S. Smith, *Structure of phospholipid monolayers containing poly(ethylene glycol) lipids at the air-water interface*, *Journal of Physical Chemistry B* **101** (1997) 3122–3129.

[34] Z. Xu, N. B. Holland, and R. E. Marchant, *Conformations of short-chain poly(ethylene oxide) lipopolymers at the air-water interface: a combined film balance and surface tension study*, *Langmuir* **17** (2001) 377–383.

[35] K. Tanwir and V. Tsoukanova, *Lateral distribution of a poly(ethylene glycol)-grafted phospholipid in phosphocholine monolayers studied by epifluorescence microscopy*, *Langmuir* **24** (2008) 14078–14087.

[36] Z. A. Zell, L. Isa, P. Ilg, L. G. Leal, and T. M. Squires, *Adsorption energies of poly(ethylene oxide)-based surfactants and nanoparticles on an air water surface*, *Langmuir* **30** (2014) 110–119.

[37] I. Williams and T. M. Squires, *Evolution and mechanics of mixed phospholipid fibrinogen monolayers*, *J. R. Soc. Interface* **15** (2018) 20170895.

[38] Z. A. Zell, V. Mansard, J. Wright, K. Kim, S. Q. Choi, and T. M. Squires, *Linear and nonlinear microrheometry of small samples and interfaces using microfabricated probes*, *Journal of Rheology* **60** (2016) 141–159.

[39] S. Q. Choi, S. Steltenkamp, J. A. Zasadzinski, and T. M. Squires, *Active microrheology and simultaneous visualization of sheared phospholipid monolayers*, *Nature Communications* **2** (2011) 312–316.

[40] E. Kitsiouli, G. Nakos, and M. E. Lekka, *Phospholipase a2 subclasses in acute respiratory distress syndrome*, *Biochimica et Biophysica Acta - Molecular Basis of Disease* **1792** (2009) 941–953.

[41] K. Kim, S. Q. Choi, J. a. Zasadzinski, and T. M. Squires, *Interfacial microrheology of dppc monolayers at the air–water interface*, *Soft Matter* **7** (2011) 7782–7789.

[42] E. Hermans and J. Vermant, *Interfacial shear rheology of dppc under physiologically relevant conditions*, *Soft Matter* **10** (2014) 175–186.

[43] R. M. Weis, *Fluorescence microscopy of phospholipid monolayer phase transitions*, *Chemistry and Physics of Lipids* **57** (1991) 227–239.

[44] V. T. Moy, D. J. Keller, H. E. Gaub, and H. M. McConnell, *Long-range molecular orientational order in monolayer solid domains of phospholipid*, *Journal of Physical Chemistry* **90** (1986) 3198–3202.

[45] C. W. McConlogue and T. K. Vanderlick, *A close look at domain formation in dppc monolayers*, *Langmuir* **13** (1997) 7158–7164.

[46] D. W. Grainger, A. Reichert, H. Ringsdorf, and C. Salesse, *An enzyme caught in action: Direct imaging of hydrolytic function and domain formation of phospholipase a2 in phosphatidylcholine monolayers*, *FEBS Letters* **252** (1989) 73–82.

[47] H. M. Mcconnell, *Structures and transitions in lipid monolayers at the air-water interface*, *Annual Review of Physical Chemistry* **42** (1991) 171–195.

[48] S. Q. Choi, S. G. Jang, A. J. Pascall, M. D. Dimitriou, T. Kang, C. J. Hawker, and T. M. Squires, *Synthesis of multifunctional micrometer-sized particles with magnetic, amphiphilic, and anisotropic properties*, *Advanced Materials* **23** (2011) 2348–2352.

[49] S. Trabelsi, S. Zhang, T. R. Lee, and D. K. Schwartz, *Linactants: Surfactant analogues in two dimensions*, *Physical Review Letters* **100** (2008) 2–5.

[50] H. A. Stone, B. Bentley, and L. Leal, *An experimental study of transient effects in the breakup of viscous drops*, *Journal of Fluid Mechanics* **173** (1986) 131–158.

[51] K. Maloney, M. Grandbois, D. Grainger, C. Salesse, K. Lewis, and M. Roberts, *Phospholipase a2 domain formation in hydrolyzed asymmetric phospholipid monolayers at the air/water interface*, *Biochimica et Biophysica Acta (BBA) - Biomembranes* **1235** (1995) 395–405.

[52] D. W. Grainger, a Reichert, H. Ringsdorf, and C. Salesse, *Hydrolytic action of phospholipase a2 in monolayers in the phase transition region: direct observation of enzyme domain formation using fluorescence microscopy.*, *Biochimica et biophysica acta* **1023** (1990) 365–79.

[53] H. M. McConnell and V. T. Moy, *Shapes of finite two-dimensional lipid domains*, *Journal of Physical Chemistry* **92** (1988) 4520–4525.

[54] J. M. Barakat and T. Squires, *Shape morphology of dipolar domains in planar and spherical monolayers*, *The Journal of Chemical Physics* **152** (2020), no. 23 234701.

[55] M. Grandbois, B. Desbat, and C. Salesse, *Monitoring of phospholipid monolayer hydrolysis by phospholipase a2 by use of polarization-modulated fourier transform infrared spectroscopy*, *Biophysical Chemistry* **88** (2000) 127–135.

[56] D. Lichtenberg, H. Ahyayauch, and F. M. Goñi, *The mechanism of detergent solubilization of lipid bilayers*, *Biophysical Journal* **105** (2013) 289–299.

[57] D. Lichtenberg, H. Ahyayauch, A. Alonso, and F. M. Goñi, *Detergent solubilization of lipid bilayers: A balance of driving forces*, *Trends in Biochemical Sciences* **38** (2013) 85–93.

[58] D. Needham and D. V. Zhelev, *Lysolipid exchange with lipid vesicle membranes*, *Annals of Biomedical Engineering* **23** (1995) 287–298.

[59] J. M. Barakat and T. M. Squires, *Curvature and shape relaxation in surface-viscous domains*, *Physical Review Fluids* **8** (2023), no. 5 054001.

[60] S. Barman, M. L. Davidson, L. M. Walker, S. L. Anna, and J. A. Zasadzinski, *Inflammation product effects on dilatational mechanics can trigger the laplace instability and acute respiratory distress syndrome*, *Soft matter* **16** (2020), no. 29 6890–6901.

[61] B.-M. Chen, T.-L. Cheng, and S. R. Roffler, *Polyethylene glycol immunogenicity: theoretical, clinical, and practical aspects of anti-polyethylene glycol antibodies*, *ACS nano* **15** (2021), no. 9 14022–14048.

[62] B. Cabanillas and N. Novak, *Allergy to covid-19 vaccines: a current update*, *Allergology International* **70** (2021), no. 3 313–318.

[63] P. Sellaturay, S. Nasser, S. Islam, P. Gurugama, and P. W. Ewan, *Polyethylene glycol (peg) is a cause of anaphylaxis to the pfizer/biontech mrna covid-19 vaccine*, *Clinical and Experimental Allergy* **51** (2021), no. 6 861.

[64] Q. Yang, T. M. Jacobs, J. D. McCallen, D. T. Moore, J. T. Huckaby, J. N. Edelstein, and S. K. Lai, *Analysis of pre-existing igg and igm antibodies against polyethylene glycol (peg) in the general population*, *Analytical chemistry* **88** (2016), no. 23 11804–11812.

[65] M. R. Sherman, L. D. Williams, M. A. Sobczyk, S. J. Michaels, and M. G. Saifer, *Role of the methoxy group in immune responses to mpeg-protein conjugates*, *Bioconjugate chemistry* **23** (2012), no. 3 485–499.

[66] Z. A. Zell, S. Q. Choi, L. G. Leal, and T. M. Squires, *Microfabricated deflection tensiometers for insoluble surfactants*, *Applied Physics Letters* **97** (2010) 1–3.

[67] P. Perczyk and M. Broniatowski, *Simultaneous action of microbial phospholipase c and lipase on model bacterial membranes – modeling the processes crucial for bioaugmentation*, *Biochimica et Biophysica Acta - Biomembranes* **1863** (2021) 183620.

[68] I. Noda, N. Kato, T. Kitano, and M. Nagasawa, *Thermodynamic properties of moderately concentrated solutions of linear polymers*, *Macromolecules* **14** (1981) 668–676.

[69] M. Kawaguchi, S. Komatsu, M. Matsuzumi, and A. Takahashi, *Concentration dependence of surface pressure of polyether monolayers at the air-water interface*, *Journal of Colloid And Interface Science* **102** (1984) 356–360.

[70] J. Des Cloizeaux, *The lagrangian theory of polymer solutions at intermediate concentrations*, *Journal de Physique* **36** (1975), no. 4 281–291.

[71] J. C. L. Guillou and J. Zinn-Justin, *Critical exponents from field theory*, *Physical Review B* **21** (1980) 3976–3998.

[72] N. J. Alvarez, L. M. Walker, and S. L. Anna, *A microtensiometer to probe the effect of radius of curvature on surfactant transport to a spherical interface*, *Langmuir* **26** (2010) 13310–13319.

[73] A. P. Kotula and S. L. Anna, *Regular perturbation analysis of small amplitude oscillatory dilatation of an interface in a capillary pressure tensiometer*, *Journal of Rheology* **59** (2015), no. 1 85–117.

[74] A. K. Sachan and J. A. Zasadzinski, *Interfacial curvature effects on the monolayer morphology and dynamics of a clinical lung surfactant*, *Proceedings of the National Academy of Sciences* **115** (2018), no. 2 E134–E143.

[75] G. Ma and H. C. Allen, *Condensing effect of palmitic acid on dppc in mixed langmuir monolayers*, *Langmuir* **23** (2007) 589–597.

[76] S. Q. Choi, *Investigation of rheological properties of fluid / fluid interfaces*, 2011.

[77] C. Alonso and J. A. Zasadzinski, *A brief review of the relationships between monolayer viscosity, phase behavior, surface pressure, and temperature using a simple monolayer viscometer*, *Journal of Physical Chemistry B* **110** (2006) 22185–22191.

[78] Z. A. Zell, A. Nowbahar, V. Mansard, L. G. Leal, S. S. Deshmukh, J. M. Mecca, C. J. Tucker, and T. M. Squires, *Surface shear inviscidity of soluble surfactants*, *Proceedings of the National Academy of Sciences* **111** (2014) 3677–3682.